Chapter 1
Fundamentals of Infrared Thermal Imaging

1.1
Introduction

Infrared (IR) thermal imaging, also often called *thermography* for short, is a very rapidly evolving field in science as well as industry owing to the enormous progress made in the last three decades in microsystem technologies of IR detector design, electronics, and computer science. Thermography nowadays is applied in research and development as well as in a variety of different fields in industry, such as nondestructive testing, condition monitoring, and predictive maintenance, reducing energy costs of processes and buildings, detection of gaseous species, and many more areas. In addition, competition in the profitable industry segment of camera manufacturers has recently led to the introduction of low-cost models at a price level of just several thousand dollars or euros, and smartphone accessories even below five hundred dollars, which has opened up new application fields for the cameras. Besides education (obviously schools' problems with financing expensive equipment for science classes are well known), IR cameras will probably soon be advertised in hardware stores as "must-have" do-it-yourself products for analyzing building insulation, heating pipes, or electrical components in homes. This development has both advantages and drawbacks.

The advantages may be illustrated by an anecdote based on personal experiences concerning physics teaching in school. Physics was, and still is, considered to be a very difficult subject in school. One of the reasons may be that simple phenomena of physics, for example, friction or the principle of energy conservation in mechanics, are often taught in such an abstract way that rather than being attracted to the subject, students are scared away. One of us clearly remembers a frustrating physics lesson at school dealing first with free-falling objects and then with the action of walking on a floor. First, the teacher argued that a falling stone would transfer energy to the floor such that the total energy was conserved. He only used mathematical equations but stopped his argument at the conversion of initial potential energy of the stone to kinetic energy just prior to impact with the floor. The rest was a hand-waving argument that, of course, the energy would be transformed into heat. The last argument was not logically developed; it was just one of the typical teacher arguments to be believed (or not). Of course, at

Infrared Thermal Imaging, Second Edition. M. Vollmer and K.-P. Möllmann.

those times, it was very difficult in schools to actually measure the conversion of kinetic energy into heat. Maybe the students would have been more satisfied if the teacher had at least attempted to visualize the process in more detail. The second example – explaining the simple action of walking – was similarly frustrating. The teacher argued that movement was possible owing to the frictional forces between shoe and floor. He then wrote down some equations describing the underlying physics, and that was all. Again, there were missing arguments: if someone walking has to do work against frictional forces, there must be some conversion of kinetic energy into heat, and shoes as well as the floor must heat up. Again, of course, at those times, it was very difficult in school to actually measure the resulting tiny temperature rises of shoes and floors. Nevertheless not discussing them at all was a good example of bad teaching. And again, maybe some kind of visualization would have helped. But visualizations were not a strength of this old teacher, who rather preferred to have Newton's laws recited in Latin.

Visualization refers to any technique for creating images, diagrams, or animations to communicate an abstract or a concrete argument. It can help bring structure to a complex context, it can make verbal statements clear, or it can give clear and appropriate visual representations of situations or processes. The underlying idea is to provide visual concepts that help to better understand and better recollect a context. Today, in the computer age, visualization is finding ever-expanding applications in science, engineering, medicine, and other fields. In the natural sciences, visualization techniques are often used to represent data from simulations or experiments in plots or images in order to make analysis of the data as easy as possible. Powerful software techniques often enable the user to modify the visualization in real time, thereby allowing easy perception of patterns and relations in the abstract data in question.

Thermography is an excellent example of a visualization technique that can be used in many different fields of physics and science. Moreover, it has opened up a totally new realm of physics in terms of visualization. Nowadays, it is possible to visualize easily the (to the human eye) invisible effects of temperature rise of the floor upon impact of a falling object or upon interaction with the shoe of a walking person. This will allow totally new ways of teaching physics and the natural sciences starting in school and ending in the training of professionals in all kinds of industries. Visualization of "invisible" processes of physics or chemistry with thermography can be a major factor creating fascination for and interest in these subjects, not only in students at school and university but also for the layperson. Nearly every example described later in this book can be studied in this context.

The drawbacks of promoting IR cameras as mass products for a wide range of consumers are less obvious. Anyone owning an IR camera will be able to produce nice and colorful images, but most will never be able to fully exploit the potentials of such a camera – and most will never be able to correctly use it.

Typically, the first images recorded with any camera will be the faces of people nearby. Figure 1.1 gives an example of IR images of the two authors. Anyone confronted with such images for the first time would normally find them fascinating since they provide a totally new way of looking at people. The faces can still be

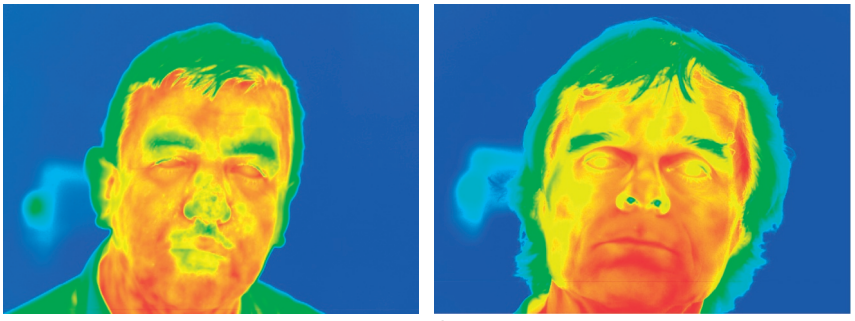

Figure 1.1 IR thermal images of (a) K-P. Möllmann and (b) M. Vollmer.

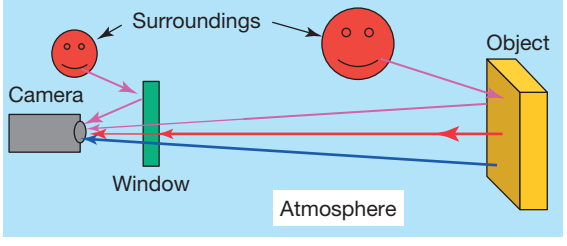

Figure 1.2 Various signal contributions entering an IR camera due to external influences.

recognized, but some parts look strange, for example, the eyes. Also, the nostrils (Figure 1.1b) seem to be distinctive and the hair to be surrounded by an "aura."

For artists who want to create new effects, such images are fine, but thermography – if it is to be used for the analysis of real problems like building insulation, for example – is much more than this. Modern IR cameras may give qualitative images, colorful images that look nice but mean nothing, or they can be used as quantitative measuring instruments. The latter use is the original reason for developing these systems. Thermography is a measurement technique that, in most cases, is able to quantitatively measure surface temperatures of objects. To use this technique correctly, professionals must know exactly what the camera does and what the user must do to extract useful information from images. This knowledge can only be obtained through professional training. Therefore, the drawback in IR cameras is that they require professional training before they can be used properly. A multitude of factors can influence IR images and, hence, any interpretation of such images (Figure 1.2 and Chapters 2 and 7).

First, radiation from an object (red) is attenuated via absorption or scattering while traveling through the atmosphere (Section 1.5.2), IR windows, or the camera optics (Section 1.5.4). Second, the atmosphere itself can emit radiation owing to its temperature (blue) (this also holds for windows or the camera optics and housing itself), and third, warm or hot objects in the surroundings (even the thermographer is a source) may lead to reflections of additional IR radiation from the

Table 1.1 Several parameters and factors affecting images recorded with modern IR cameras systems.

Parameters affecting IR images generated from raw detector data within camera that can usually be adjusted using camera software; quantitative results can strongly depend on some of these parameters! They can often be changed while analyzing images (after recording) if proper software is used (this may not be possible for the cheapest models!)	• Emissivity of object • Distance of camera to object (usually in meters, feet in the USA) • Size of object • Relative humidity • Ambient temperature (usually in degrees Celsius or Kelvin, degrees Fahrenheit in the USA) • Atmospheric temperature • External optics temperature • External optics transmission
Parameters affecting how data are plotted as an image; if chosen unfavorably, important details may be disguised	• Temperature span ΔT • Temperature range and level • Color palette
Some parameters that can significantly affect quantitative analysis and interpretation of IR images	• Wavelength dependence of emissivity (wavelength range of camera) • Angular dependence of emissivity (angle of observation) • Temperature dependence of emissivity • Optical properties of matter between camera and object • Use of filters (e.g., high temperature, narrowband) • Thermal reflections • Wind speed • Solar load • Shadow effects of nearby objects • Moisture • Thermal properties of objects (e.g., time constants)

object or windows, and so on (pink arrows). The contributions from the object or windows may, furthermore, depend on the material, the surface structure, and so on, which are described by the parameter emissivity. These and other parameters are listed in Table 1.1; they are all discussed in subsequent sections.

Even if all of these parameters are dealt with, some remaining open questions will need to be answered. Consider, for example, someone who uses IR imaging in predictive maintenance doing electrical component inspections. Suppose the recording of an IR image shows a component with an elevated temperature. The fundamental problem is the assessment criterion for the analysis of IR images. How hot can a component become and still be okay? What is the criterion for an immediate replacement, or how long can one wait before replacement? These questions involve a lot of money if the component is involved in the power supply

of an industrial complex, the failure of which can lead to a shutdown of a facility for a certain period of time.

Obviously, buying a camera and recording IR images may shift the problem from not knowing anything at all to the problem of understanding the IR technology being used and all aspects of IR image interpretation. This book deals with the second problem. In this respect, it is addressed to at least three different groups of people. First, it will benefit interested newcomers to the field by giving an introduction to the general topic of IR thermal imaging, by discussing the underlying fundamental physics, and by presenting numerous examples of the technique in research as well as in industry. Second, it will benefit educators at all levels who want to include IR imaging in their curriculum in order to facilitate the understanding of physics and science topics as well as IR imaging in general. Third, it is addressed to all practitioners who own an IR camera and want to use it as a quantitative or qualitative tool for business. The text complements any kind of modern IR camera training/certification course as is offered by nearly every manufacturer of such camera systems.

The authors sincerely hope that this text will help reduce the number of colorful, but often quite wrongly interpreted, IR images of buildings and other objects in daily newspapers. In one typical example, a (probably south) wall of a house that had been illuminated by the sun for several hours before the IR image was taken was – of course – showing up as being warmer than the windows and other walls of the house. The interpretation that the wall was obviously very badly insulated was, however, pure nonsense (Chapter 7). In addition, we hope that in the future trained specialists will no longer call up their manufacturer and ask, for example, why they are not able to see any fish in their aquarium or in a pond with a long-wave (LW) camera. When that happens, there will be no more complaints about system malfunctions because the IR camera measures skin temperatures well above 45 °C. Or, to give a last example, people will no longer ask whether they are also able to measure the temperature of hot noble gases or oxygen using IR imaging.

We next come to the reason for bringing out the second edition of our book on IR thermal imaging. Of course, various handbooks have been published [1–6] that contain articles on several related topics, a number of books are available on certain aspects like the principles of radiation thermometry [7–9], detectors and detector systems, and their testing [10–16], IR material properties [17, 18], the fundamentals of heat transfer [19, 20], and an overview of the electromagnetic (EM) spectrum in the IR and adjacent regions [21], and, finally, some concise books on practical applications have also been released [22–24]. However, not only the detector technologies but also the range of applications have increased enormously over the past decade and since the first edition of this textbook. Therefore, an up-to-date review of the 2017 state of the art in technology and applications seems overdue.

This text uses the international system of units. The only deviation from this rule concerns temperature, probably the most important quantity for thermography. Temperatures in science should be given in Kelvin; IR camera manufac-

Table 1.2 Relation between three commonly used temperature scales in thermography.

T (K)	T (°C)	T (°F)
0 (absolute zero)	−273.15	−459.67
273.15	0	32
373.15	100	212
1273.15	1000	1832

ΔT (K) = ΔT(°C); ΔT (°C) = (5/9) · ΔT (°F);
T (K) = T (°C) + 273.15; T (°C) = (5/9) · (T (°F) − 32);
T (°F) = (9/5) · T (°C) + 32.

turers, however, mostly use the more common Celsius scale for their images. For North American customers, there is the option of presenting temperatures on the Fahrenheit scale. Table 1.2 gives a short survey of how these temperature readings can be converted from one unit to another.

1.2 Infrared Radiation

1.2.1 Electromagnetic Waves and the Electromagnetic Spectrum

In physics, visible light (VIS), ultraviolet (UV) radiation, IR radiation, and so on can be described as waves – to be more specific, as EM waves (for some properties of IR radiation, e.g., in detectors, a different point of view with radiation acting like a particle is adopted, but for most applications, the wave description is more useful).

Waves are periodic disturbances (think, e.g., of vertical displacements of a water surface after a stone has been thrown into a puddle or lake) that keep their shape while progressing in space as a function of time. The spatial periodicity is called *wavelength*, λ (given, for example, in meters, micrometers, nanometers), the transient periodicity is called the *period of oscillation*, T (in seconds), and its reciprocal is the *frequency*, $\nu = 1/T$ (in s^{-1} or Hertz). Both are connected via the speed of propagation c of the wave by Eq. (1.1):

$$c = \nu \cdot \lambda \tag{1.1}$$

The speed of propagation of waves depends on the specific type of wave. Sound waves, which exist only if matter is present, have typical speeds of about 340 m s^{-1} in air (think of the familiar thunder and lightning rule: if you hear the thunder 3 s after seeing the lightning, it has struck at a distance of about 1 km). In liquids, this speed is typically at least three times higher, and in solids, the speed of sound can reach about 5 km s^{-1}. In contrast, EM waves propagate at the much higher speed

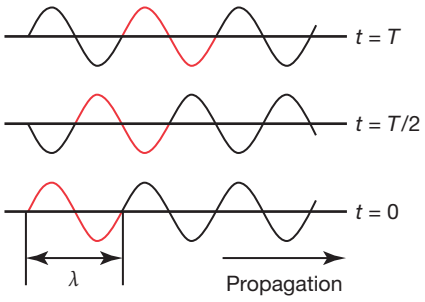

Figure 1.3 Three snapshots of a sinusoidal wave traveling from left to right. Part of the wave (one wavelength) is marked (red line) to demonstrate how the wave propagates as a function of time. The snapshots start at $t = 0$ then show the wave after half a period and a full period. In one period T, the wave has traveled one wavelength λ.

of light, which is $c = 299\,792\,458\ \mathrm{m\,s^{-1}} \approx 300\,000\ \mathrm{km\,s^{-1}}$ in a vacuum and $v = c/n$ in matter, with n being the index of refraction, which is a number of the order of unity.

In nature, the geometric form of a disturbance is very often sinusoidal, that is, it can be described by the mathematical sine function. Figure 1.3 schematically depicts snapshots of a sinusoidal wave traveling from left to right in space. The bottom snapshot refers to a starting time of $t = 0$. One wavelength λ is marked by a red bold line. After half a period of oscillation (when $t = T/2$), the wave has moved by $\lambda/2$, and when $t = T$, it has moved by one wavelength in the propagation direction.

Disturbances, which resemble waves, can be of a great variety. For example, sound waves in gases are due to pressure variations and water waves are vertical displacements of the surface. According to the type of disturbance, two wave types are usually defined: in longitudinal waves (e.g., sound waves in gases), the disturbance is parallel to the propagation direction, whereas in transverse waves (e.g., surface-water waves), it is perpendicular to it. With springs (Figure 1.4), both types of waves are possible (e.g., sound waves in solids). In transverse waves, the disturbances can oscillate in many different directions. This is described by the property called *polarization*. The *plane of polarization* is the plane defined by the disturbance and the propagation direction.

Light and IR radiation are EM waves. In EM waves, the disturbances are electric and magnetic fields. They are perpendicular to each other and also perpendicular to the propagation direction, that is, EM waves are transverse waves (Figure 1.5). The maximum disturbance (or elongation) is called the *amplitude*.

The polarization is defined by the electric field and the propagation direction, that is, the wave is polarized in the x–z plane in Figure 1.5. Sunlight and light from many other sources like fire, candles, or light bulbs is unpolarized, that is, the plane of polarization of these light waves can have all possible orientations. Such unpolarized radiation may, however, become polarized by reflections from surfaces or on passing a so-called polarizer.

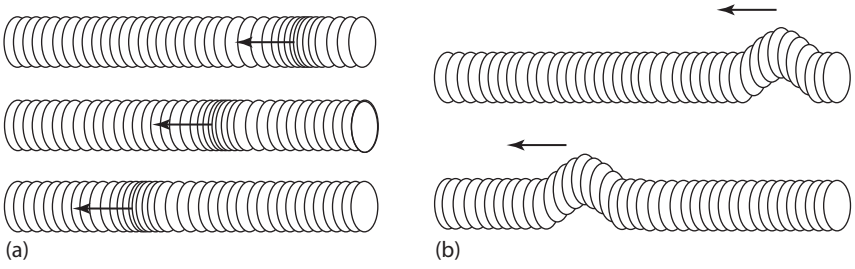

Figure 1.4 Illustration of longitudinal (a) and transverse waves (b). The latter have the additional property of polarization.

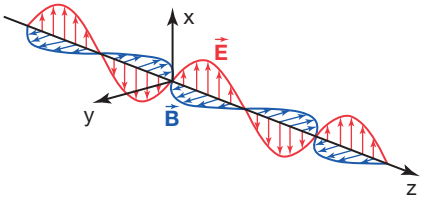

Figure 1.5 IR radiation involves a special kind of EM waves. In EM waves, the electric field and the magnetic induction field are perpendicular to each other and to the direction of propagation (here the *z*-direction).

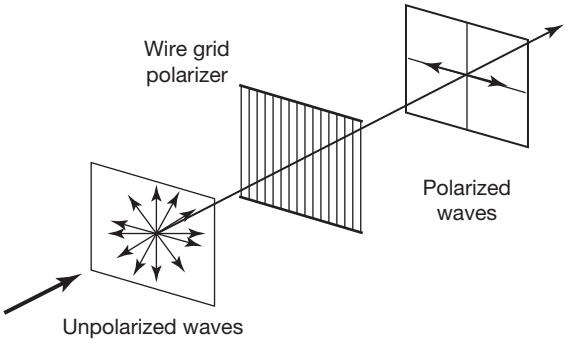

Figure 1.6 Microscopic wire grids can act as polarizers for IR radiation. The transmitted electric field oscillates perpendicular to the direction of the wires.

For VIS and IR radiation the simplest polarizer consists of a microscopically small conducting grid (similarly, a metal wire grid can polarize microwave radiation). If unpolarized radiation is incident on such a grid, only those waves whose electric field is oscillating perpendicular to the grid wires are transmitted (Figure 1.6). Such polarizing filters can help suppress reflections when taking photos with a camera (for more details, see [25, 26] and Section 3.4).

Figure 1.7 gives an overview of EM waves, ordered according to their wavelength or frequency. This spectrum consists of a great variety of different waves. All of them can be observed in nature, and many have technical applications.

Starting from the top of the figure, for example, γ-rays have the highest frequencies, that is, the shortest wavelengths. X-rays are well known from their medical applications, and UV radiation is important in the context of the ozone hole

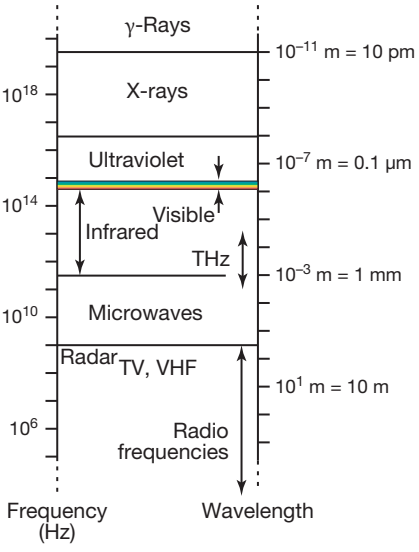

Figure 1.7 Overview of most common types of EM waves. The visible spectral range (VIS) covers only a tiny part with wavelengths from 0.38 to 0.78 µm, followed at longer wavelengths by the infrared (IR) from 0.78 µm to 1 mm.

since less ozone in the upper atmosphere means more UV radiation from the sun reaches the surface of the earth, which can cause skin cancer. The visible light, defined by the sensitive range of the light receptors in our eyes, only covers a very small range within this spectrum, with wavelengths from 380 to 780 nm. The adjacent spectral region with wavelengths from 780 up to 1 mm is usually called *infrared*, which is the topic of this book. This range is followed by microwaves, RADAR, and all EM waves that are used for radio, TV, and so on. Recently, new sensing developments in the frequency range from 0.1 to 10 THz have led to the newly defined range of terahertz radiation, which overlaps part of the IR and microwave ranges.

For IR imaging, only a small range of the IR spectrum is used. It is shown in an expanded view in Figure 1.8. Typically, three spectral ranges are defined for thermography: the long-wave (LW) region from around 8 to 14 µm, the mid-wave (MW) region from around 3 to 5 µm, and the short-wave (SW) region from 0.9 to 1.7 µm. Commercial cameras are available for these three ranges (note that the limiting wavelengths for these ranges, also called *bands*, can vary depending on the actual detector sensitivities (Figure 2.71) and additional optical filter elements; for most simple estimates we use the aforementioned values). The restriction to these wavelengths follows firstly from considerations of the amount of thermal radiation to be expected (Section 1.3.2), secondly from the physics of detectors (Chapter 2), and thirdly from the transmission properties of the atmosphere (Section 1.5.2).

The origin of naturally occurring EM radiation is manifold. The most important process for thermography is the so-called thermal radiation, which will be discussed in detail in the next section. In brief, the term *thermal radiation* implies that every body or object at a temperature $T > 0\,\mathrm{K}$ (−273.15 °C) emits EM radiation. The amount of radiation and its distribution as a function of wavelength

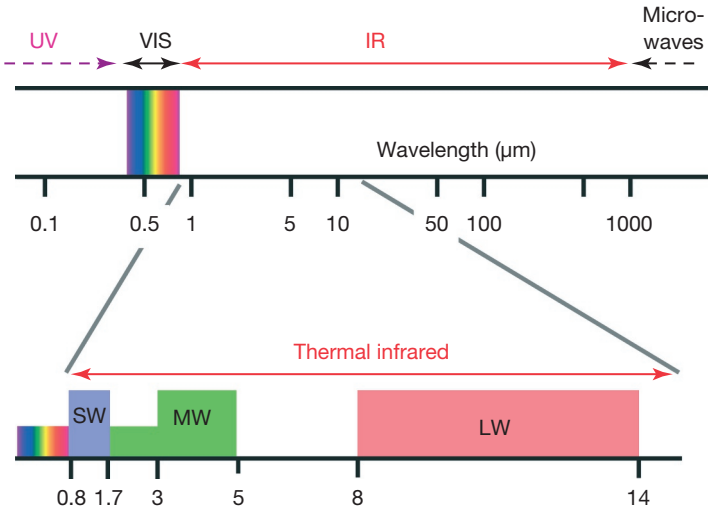

Figure 1.8 Infrared (IR) and adjacent spectral regions and expanded view of so-called thermal IR. This is the region where IR imaging systems for short-wave (SW), mid-wave (MW), and long-wave (LW) cameras exist. Special systems have extended ranges.

depend on temperature and material properties. For temperatures in the range of natural and technological processes, this radiation is in the thermal IR spectral region.

1.2.2 Basics of Geometrical Optics for Infrared Radiation

1.2.2.1 Geometric Properties of Reflection and Refraction

From the observation of shadows or the use of laser pointers, it is an everyday experience that visible light propagates more or less in straight lines. This behavior is most easily described in terms of geometrical optics. This description is valid if the wavelength of the light is much smaller than the size of the objects/structures on which the light is incident. IR radiation has a behavior very similar to that of visible light; hence, it can also often be described using geometrical optics:

- In homogeneous materials, IR radiation propagates in straight lines. It can be described as rays whose propagation follows from geometrical laws. Usually the rays are indicated by arrows.
- At the boundary between two materials, part of the incident radiation is reflected, and part of it is transmitted as refracted IR radiation (Figure 1.9).
- The optical properties of homogeneous materials, for example, those of a lens of an IR camera, are described by the index of refraction n. This index n is a real number larger than unity for nonabsorbing materials and a complex mathematical quantity for absorbing materials. The properties of materials for the thermal IR spectral range are described in detail in Section 1.5.

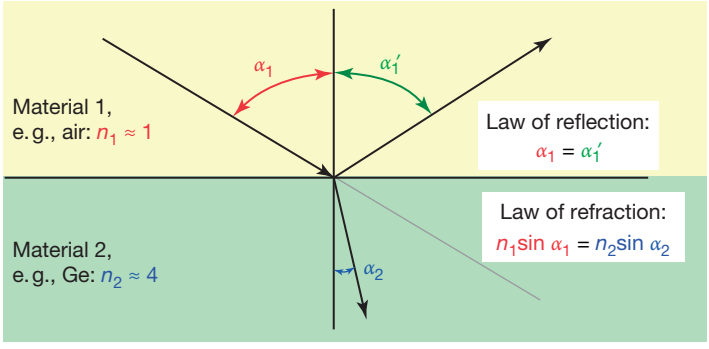

Figure 1.9 Laws of reflection and refraction in geometrical optics. The examples given in the figure refer to IR radiation, which is incident from the air on a germanium surface.

- The orientation between the incident radiation and surface normal of the boundary between two materials is called the *angle of incidence*, α_1. The corresponding angle between the reflected ray and the surface normal is the angle of reflection, α_1'. The law of reflection – which is the basis for mirror optics – states that

$$\alpha_1' = \alpha_1 \tag{1.2}$$

- The orientation between the transmitted refracted radiation and surface normal of the boundary between two materials is called the *angle of refraction*, α_2. If the index of refraction of the two materials are given by n_1 and n_2, the law of refraction (also called *Snell's law*) – which is the basis for lens optics – states that

$$n_1 \sin \alpha_1 = n_2 \sin \alpha_2 \tag{1.3}$$

The propagation of radiation in matter can be described using these two laws. Nowadays, this is mostly done using ray-tracing programs, which make it possible to follow the path of radiation through many different materials and a large number of boundaries, as are usual, for example, in complex lens systems used in optical instruments such as IR cameras.

Refraction is also the basis for studying spectra and defining the IR spectral region. In the seventeenth century, Isaac Newton demonstrated that the index of refraction of materials depends on the wavelength of visible light. The same holds for IR radiation. Typical optical materials show a normal dispersion, that is, the index of refraction decreases with increasing wavelength. If radiation is incident on a prism, the angles of refracted light within the prism are determined from the law of refraction. If the index of refraction decreases with increasing wavelength, the radiation with longer wavelength is refracted less than the short wavelength radiation. The same holds for the second boundary of the prism. As a result, the incident EM radiation is spread out into a spectrum behind the prism. If thermal IR radiation is incident and the prism is made of an IR transparent

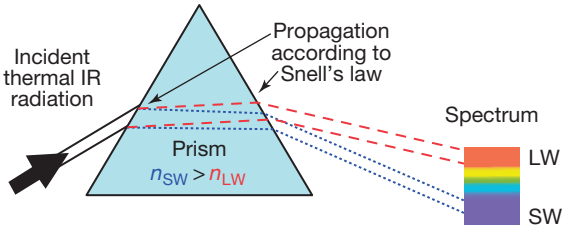

Figure 1.10 Generating a spectrum from a collimated narrow beam of EM radiation using a nonabsorbing prism.

material, the LW radiation will end up on top and the SW radiation on the bottom of the spectrum in Figure 1.10.

1.2.2.2 Specular and Diffuse Reflection

Finally, IR imaging is often used to study objects with rough surfaces. In such cases, reflection need not be directed but can also have a diffuse component. Figure 1.11 illustrates the transition from directed reflection, also called *specular reflection*, to diffuse reflection.

1.2.2.3 Portion of Reflected and Transmitted Radiation: Fresnel Equations

Equations 1.2 and 1.3 give the directions of reflected and transmitted radiation. The portions of reflected and transmitted light, which depend on angle of incidence, can also be computed from the so-called Fresnel equations of wave optics [25, 27]. For the purpose of this book, graphical results will be sufficient. Fig-

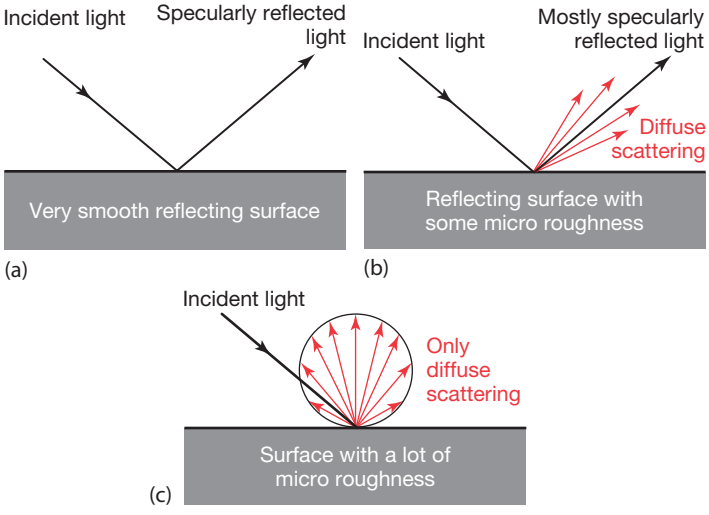

Figure 1.11 During the transition from smooth to rough surfaces, optical reflections change from specular mirrorlike (a) to diffuse reflection (c). The most common case is a combination of both types of reflection (b).

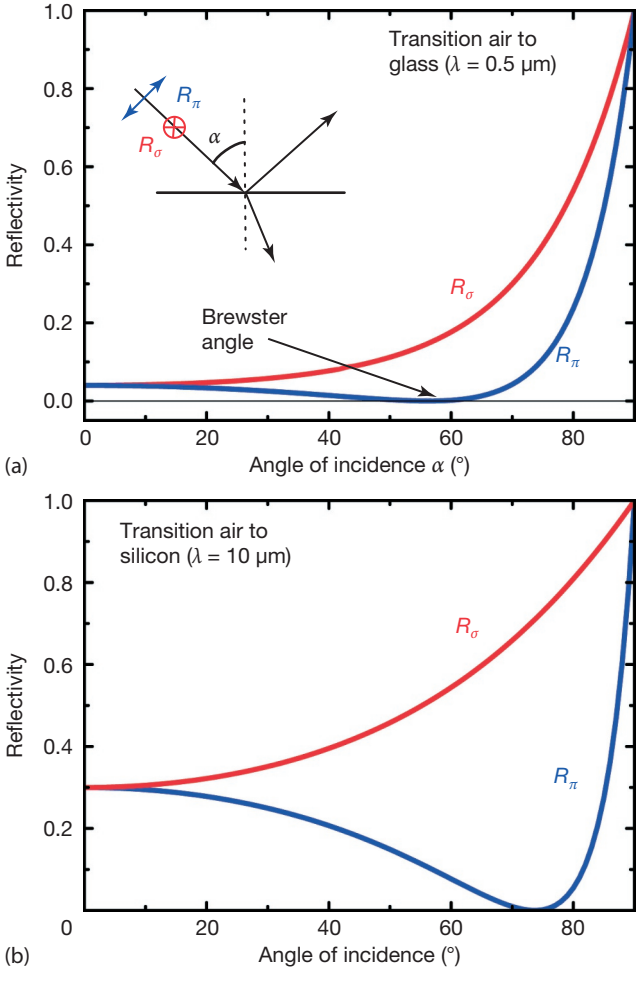

Figure 1.12 The portion of reflected visible light from an air–glass boundary (a) or of IR radiation from an air–silicon boundary (b) depends on the polarization of the radiation.

ure 1.12 shows representative results for the reflection of visible light ($\lambda = 0.5$ µm) for a boundary between air and glass and for IR radiation ($\lambda = 10$ µm) for a boundary between air and silicon.

Reflected light consists of two contributions: the first is light that is polarized parallel (R_π) and the second is light that is polarized perpendicular (R_σ) to the plane of incidence. The latter is defined as the plane made up by the surface normal of the boundary and the propagation direction of the EM radiation. In Figure 1.9 and the inset in Figure 1.12, the drawing plane is the plane of incidence. For the perpendicular component, the portion of reflected radiation, called *reflectivity*, slowly increases from 0.04 for the VIS case (and about 0.3 for IR) at normal incidence ($\alpha = 0°$) up to the maximum value of 1.0 at grazing incidence ($\alpha = 90°$).

In contrast, the parallel component first decreases from the same starting value at $\alpha = 0°$, reaches a specific angle, called the *Brewster angle*, with zero reflectivity, and then steeply rises to the maximum value of 1.0 at grazing incidence.

In general, the Brewster angle α_{Br} for a transition from a transparent, that is, nonabsorbing material A (e.g., air) to a transparent material B (e.g., glass) is defined by the condition

$$\tan(\alpha_{Br}) = \frac{\sin(\alpha_{Br})}{\cos(\alpha_{Br})} = \frac{n_B}{n_A} \tag{1.4}$$

which, for the preceding examples, gives $\alpha_{Br} = 56.3°$ for air–glass (VIS) and $\alpha_{Br} = 75°$ for air–silicon (IR). For absorbing materials, the general form of the curves stays the same; however, the minimum may not reach zero and the Brewster angles may shift.

Thermal reflections are important in many applications of thermography. For quick numerical estimates, we mention Eq. (1.5), which gives the reflectivity R (portion of reflected radiation) in terms of the refractive indices for the case of normal incidence ($\alpha = 0°$). The material A from which radiation is incident is considered to be transparent (e.g., air), whereas the material B from which radiation is reflected can be transparent or opaque to the radiation. In the latter case, the index of refraction, which can be found as a function of wavelength in tables of several handbooks [18], is mathematically a complex number $n_B = n_1 + \mathrm{i}n_2$ and

$$R(\alpha = 0°, n_A, n_B = n_1 + \mathrm{i}n_2) = \frac{(n_1 - n_A)^2 + n_2^2}{(n_1 + n_A)^2 + n_2^2} \tag{1.5}$$

In the preceding examples, $n_A = 1.0$, $n_1 = 1.5$, and $n_2 = 0$, which gives $R = 0.04$ for air–glass at $\lambda = 0.5\,\mu m$ and $n_A = 1.0$, $n_1 = 3.42$, and $n_2 = 6.8 \cdot 10^{-5}$, which gives $R = 0.30$ for air–silicon at $\lambda = 10\,\mu m$. Some applications of these results are discussed in the section on suppression of thermal reflections (Section 3.4).

1.3 Radiometry and Thermal Radiation

In any practical measurement with an IR camera, an object emits radiation in the direction of the camera, where it is focused on the detector and measured quantitatively. Since thermography is mostly done with solid objects, which are, furthermore, opaque to IR radiation, the emission refers to the surfaces of the objects only (the most important exception – gases – will be treated separately in Chapter 8). Let us consider a small surface area element dA that emits thermal radiation in the specific direction of the detector, which occupies a certain solid angle. To characterize the emission, propagation, and irradiance of any kind of radiation – that is, also the thermal radiation discussed here – with respect to the detector, a set of several radiometric quantities has been defined, which will be introduced in Section 1.3.1. As will become evident, a certain class of emitters – so-called black-

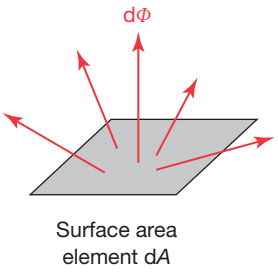

Figure 1.13 The total energy flux, dΦ, emitted by a surface area element, dA, is emitted in a hemisphere above dA.

bodies – has unique properties concerning the total amount of emitted radiation as well as their geometrical distribution. This will be discussed in Section 1.3.2.

1.3.1 Basic Radiometry

1.3.1.1 Radiant Power, Excitance, and Irradiance

Consider an element dA of the radiating surface of an object. The total energy flux dΦ from this surface element dA into the hemisphere is called *power*, *radiant power*, or *energy flux* with the SI unit W (watt) (Figure 1.13). This quantity can only be measured directly if the detector collects radiation from the hemisphere completely. This is usually not the case.

If this radiant power is related to the emitting surface area, we find the excitance, M, in W m^{-2}, using

$$M = \frac{\mathrm{d}\Phi}{\mathrm{d}A} \tag{1.6}$$

Obviously excitance (sometimes also called *emittance* or *emissive power* [16, 20]) characterizes the total radiant power within the hemisphere divided by the surface area. It contains the contributions of all emitted wavelengths (for the sake of simplicity, we write total derivatives; note, however, that these are partial derivatives, since the radiant power depends also on angles and wavelength).

If, in contrast, we consider the total incident power from a hemisphere on a given surface dA, the same definition leads to the irradiance $E = \mathrm{d}\Phi/\mathrm{d}A$. Obviously, excitance and irradiance refer to the same units of measurement, namely, watts per meter squared (W m^{-2}), but the corresponding energy flux is either emitted or received by a particular surface area dA.

1.3.1.2 Spectral Densities of Radiometric Quantities

So far, radiant power, excitance, and irradiance for an area dA refer to the total power emitted to or received from a hemisphere. In practice, all radiometric quantities do, however, also depend on wavelength. Therefore, one can easily define the spectral densities of the various radiometric quantities. As an example, Figure 1.14 illustrates the relation between radiant power Φ and its spectral den-

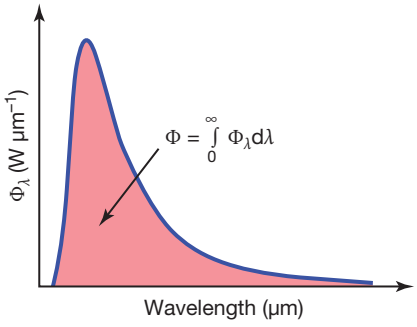

Figure 1.14 Relation between radiant power Φ and its spectral density: The total radiant power Φ (red area) is found by summing up the contribution of Φ_λ (blue curve) over the whole wavelength range.

Table 1.3 Overview of important radiometric quantities.

Name	Symbol	Unit	Definition
Energy flux or radiant power	Φ	W	Emission of energy per time in hemisphere
Excitance	M	W m^{-2}	$M = \frac{d\Phi}{dA}$ dA: emitting surface, into hemisphere
Irradiance	E	W m^{-2}	$E = \frac{d\Phi}{dA}$ dA: receiving surface, from hemisphere
Radiant intensity	I	W (sr)$^{-1}$	$I = \frac{d\Phi}{d\Omega}$
Radiance	L	W (m^2 sr)$^{-1}$	$L = \frac{d^2\Phi}{\cos\delta\, d\Omega\, dA}$
Spectral density X_λ of any chosen radiometric quantity X	X_λ	(unit of X) (µm)$^{-1}$ or (unit of X) (nm)$^{-1}$ or (unit of X) m^{-1}	$X_\lambda = \frac{dX}{d\lambda}$

sity Φ_λ.

$$\Phi_\lambda = \frac{d\Phi}{d\lambda} \tag{1.7}$$

Similar relations hold for all other radiometric quantities (Table 1.3). The excitance, that is, emissive power, would then be called, for example, *spectral excitance* or *spectral emissive power*.

1.3.1.3 Solid Angles

Most often, surfaces of objects do emit radiation, but not uniformly in the hemisphere. To account for this directionality of emitted radiation, we must introduce angles in three-dimensional coordinate systems and the concept of the solid angle. Figure 1.15a depicts the geometry: the emitting area is located in the x–y plane,

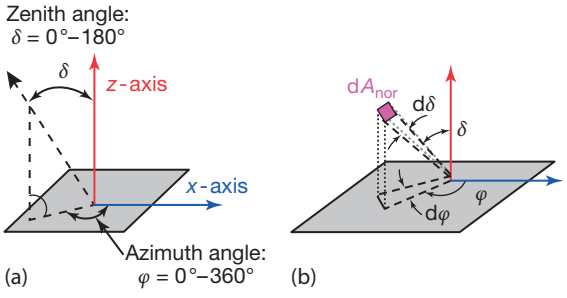

Figure 1.15 (a) Definition of angles in space and visualization of solid angle, which, (b) at a given distance from the surface, is related to the area dA_{nor}, which is normal to the chosen direction.

that is, the z-axis is perpendicular to the area. Then, any direction in space (broken arrow) can be defined by two angles, the azimuth angle φ, which is measured from the x-axis to the projection line of the chosen direction onto the x–y plane, and the zenith angle δ.

Usually, the direction itself is not important; rather, radiation is emitted toward a detector of a given surface area. For simplicity we assume an area dA_{nor} that is oriented perpendicular to the chosen direction at a distance R from a chosen point on the emitting surface. The area can be characterized by the small increments of angles $d\varphi$ and $d\delta$, as shown in Figure 1.15b. This leads to the definition of the solid angle element $d\Omega$ (for details, see textbooks on mathematics):

$$d\Omega(\delta, \varphi) = \sin\delta \cdot d\delta \cdot d\varphi = \frac{dA_{nor}}{R^2} \tag{1.8}$$

The unit of solid angle is the steradian (sr), similar to the radian (rad) for the planar angle. The full solid angle is 4π. Using δ, φ, and $d\Omega(\delta, \varphi)$, any emission of radiation in any given direction can be characterized using the quantities radiant intensity and radiance.

1.3.1.4 Radiant Intensity, Radiance, and Lambertian Emitters

The radiant intensity I is the radiant power that is emitted from a point source of a radiating object into a solid angle element $d\Omega$ in a given direction, characterized by (δ, φ). Mathematically it is given by $I = d\Phi/d\Omega$, with unit watt/steradian ($W\,sr^{-1}$).

Radiant intensity (which, by the way, is the only quantity in optics where intensity is properly defined [28]) is related to the most often used quantity in radiometry, the radiance L. Radiance is used to characterize extended sources. It is defined as the amount of radiant power per unit of projected source area and per unit solid angle:

$$L = \frac{d^2\Phi}{\cos\delta\, d\Omega\, dA}, \quad \text{i.e.,} \quad d^2\Phi = L\cos\delta\, d\Omega\, dA \tag{1.9a}$$

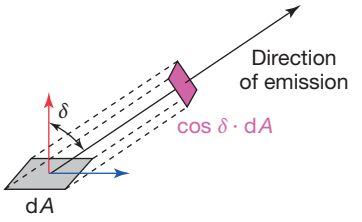

Figure 1.16 For a given direction, only the projection $dA \cdot \cos\delta$ can be seen from the emitting area dA.

The significance of this slightly more complicated definition of radiance may become obvious if Eq. (1.9a) is written in such a way as to calculate the total radiant power from the radiance:

$$\Phi = \iint L \cos\delta \, d\Omega \, dA \tag{1.9b}$$

The total radiant power results from summing up radiance contributions over the area and solid angle of the hemisphere. If only integration over a solid angle is done, one ends up with the excitance:

$$M = \frac{d\Phi}{dA} = \int_{\text{hemisphere}} L \cos\delta \, d\Omega \tag{1.10a}$$

whereas only integration over a surface area results in radiant intensity:

$$I = \frac{d\Phi}{d\Omega} = \int_{\text{source area}} L \cos\delta \, dA \tag{1.10b}$$

The geometrical factor $\cos\delta$ can be easily understood from Figure 1.16. Any emitting surface area dA is observed to be largest for a direction that is perpendicular to the surface. For any other direction, only the projection of dA perpendicular to it can contribute to the emitted radiation.

Hence, radiance is a measure of the radiant power of an emitter with surface area dA that passes through a surface that is normal to the emission direction. Since this surface defines a solid angle in this direction, radiance is a true measure of the amount of radiation that is emitted in a certain direction and per unit solid angle.

A summary of important radiometric quantities is listed in Table 1.3. SI units are used; however, for the spectral densities the wavelength interval is often given in micrometers or nanometers. This helps to avoid misinterpretations. Consider, for example, the spectral density of the excitance, which is the total radiant power per area and wavelength interval. Its unit can be expressed as $\mathrm{W\,(m^2\,\mu m)^{-1}}$ or also as $\mathrm{W\,m^{-3}}$. The first choice is much better since it avoids any misunderstanding. For example, a quantity with unit $\mathrm{W\,m^{-3}}$ could be wrongly interpreted as the power density per volume.

The difference between radiant intensity and radiance will become most obvious for so-called Lambertian radiators (after J.H. Lambert, an eighteenth-century

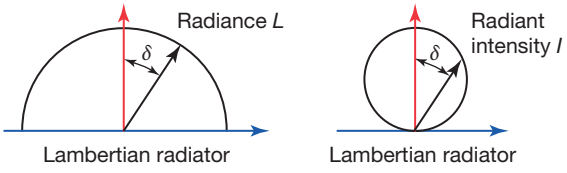

Figure 1.17 Lambertian radiators have constant radiance, but the radiant intensity depends on the direction of emission.

scientist who made significant contributions to the field of photometry). A Lambertian radiator is one that emits or reflects a radiance that is independent of angle, that is, it emits uniformly into the hemisphere. Lambertian radiators are theoretical constructs that can be approximated in the real world by blackbody sources (Section 1.4.6) or perfect diffusely scattering surfaces. In this case, L = constant and $I = L \cdot A \cdot \cos\delta = I_0 \cdot \cos\delta$. This angular dependence of radiant intensity and radiance is schematically depicted in Figure 1.17.

Why is constant radiance important? As stated earlier, radiance describes the amount of radiation emitted by an emitting area in a given direction and per unit solid angle; therefore, a Lambertian source appears to emit equal amounts of radiation in every direction. A typical example of such behavior is known from visual optics. Diffusely scattering surfaces like, for example, a tapestry, reflect the same amount of radiation in every direction. This means that, visually, the illuminated surface has the same brightness irrespective of the direction of observation. Similarly, IR cameras detect radiance from objects since the area of the camera lenses defines the solid angle, which is used for detection in the direction of the camera. If an object emits like a Lambertian source, the detected IR radiation will therefore be independent of the direction of observation. More practically speaking, the detected radiation relates to the temperature of an object. Therefore, a Lambertian source observed with an IR camera will appear to have the same temperature irrespective of the observation direction – which is, of course, a prerequisite for useful and accurate temperature measurements. Conclusion: objects studied with IR cameras should ideally behave like Lambertian sources; otherwise, complicated angle-dependent corrections would be needed.

For Lambertian surfaces, the relation between the excitance M and radiance L of a surface is given simply by $M = \pi L$. This also holds for the corresponding spectral densities, that is, in general, the excitance of Lambertian radiators equals π times their radiance. A summary of properties of Lambertian radiators is given in Table 1.4.

Table 1.4 Some relations holding for Lambertian radiators or reflectors.

Radiance	L = constant	Isotropic
Radiant intensity	$I = I_0 \cos\delta$	δ angle of direction to surface normal
Relation of excitance to radiance	$M = \pi \cdot L$; $M(\lambda) = \pi \cdot L(\lambda)$	

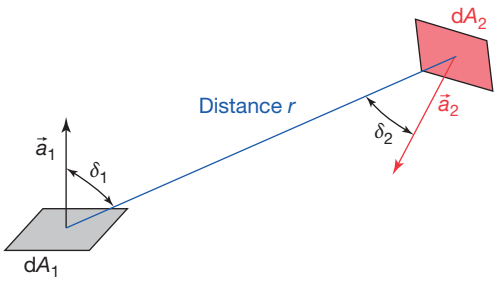

Figure 1.18 Geometry for radiation transfer between two surfaces dA_1 and dA_2.

1.3.1.5 Radiation Transfer between Surfaces: Fundamental Law of Radiometry and View Factor

The concept of radiance helps to formulate radiation exchange between two surfaces. This will become important later when we discuss practical examples such as building thermography, where neighboring buildings or objects have a significant influence on the measured surface temperature of a wall or a roof (Section 7.4). The basic relations are introduced here.

Consider two surface area elements, dA_1 and dA_2, that are arbitrarily positioned and oriented in space (Figure 1.18).

According to Eq. (1.9a), the radiant power $d^2\Phi$ that is emitted by area dA_1 and intercepted by dA_2 can be written

$$d^2\Phi = L_1 \cos\delta_1 \, dA_1 \, d\Omega_2 \tag{1.11}$$

where L_1 is the radiance from dA_1, and $d\Omega_2$ is the solid angle under which dA_2 is seen from dA_1. The latter is given by $(\cos\delta_2)\, dA_2/r^2$, which leads to the *fundamental law of radiometry*:

$$d^2\Phi = \frac{L_1 \cos\delta_1 \cos\delta_2}{r^2} \, dA_1 \, dA_2 \tag{1.12}$$

The radiant power that is emitted by dA_1 and received by dA_2 depends on the distance and relative orientation of the two areas with respect to the connecting line. Equation 1.12 makes it possible to calculate the portion of the total radiant power of a finite area A_1 of an emitting object that is incident on a finite area A_2 of a receiving object (Figure 1.19).

From Eq. (1.12), the total radiant power Φ_{12} from area A_1 that is incident on area A_2 is given by

$$\Phi_{12} = L_1 \iint\limits_{A_1,A_2} \frac{\cos\delta_1 \cos\delta_2}{r^2} \, dA_1 \, dA_2 \tag{1.13}$$

Since the total radiant power Φ_1 that is emitted by A_1 into the hemisphere can be computed to be $\Phi_1 = \pi L_1 A_1$, one needs to find the portion of Φ_1 that is inter-

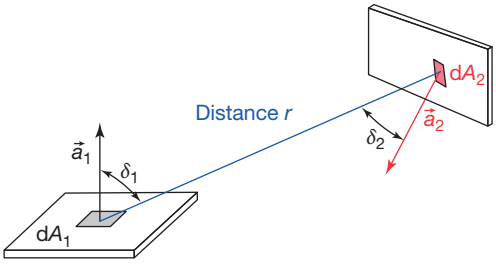

Figure 1.19 Geometry for definition of view factor. For simplicity, areas A_1 and A_2 are plotted as planar, but any kind of arbitrarily curved surface would also work.

sected by A_2, the so-called view factor:

$$F_{12} = \frac{\Phi_{12}}{\Phi_1} = \frac{1}{\pi A_1} \iint_{A_1,A_2} \frac{\cos\delta_1 \cos\delta_2}{r^2} \, \mathrm{d}A_1 \, \mathrm{d}A_2 \tag{1.14a}$$

Similarly, one may define the view factor F_{21} that describes the portion of Φ_2 that is intersected by A_1. From these definitions it follows that

$$A_1 F_{12} = A_2 F_{21} \tag{1.14b}$$

For any practical situation, one usually deals with at least two objects (the object under study and the IR camera itself) at different temperatures; hence, view factors will be used to help analyze the total net energy flux from an object to an IR camera. We return to the topic of view factors when discussing radiation exchange between objects (Section 7.4.4).

1.3.2 Blackbody Radiation

1.3.2.1 Definition

On the basis of fundamental physics, every object at any given absolute temperature above 0 K emits radiation. The maximum radiant power that can be emitted by any object depends only on the temperature of the object. Therefore, this emitted radiation is called *thermal radiation*. For real bodies, an additional material property, the emissivity, comes into play (Section 1.4).

In this section, we only deal with perfect emitters (see also Section 1.4.5) of thermal radiation, that is, those that emit the maximum radiant power. These are called *blackbodies*. Blackbodies resemble ideal surfaces having the following properties [20]:

1. A blackbody absorbs all incident radiation, regardless of wavelength and direction.
2. For a given temperature and wavelength, no surface can emit more energy than a blackbody.

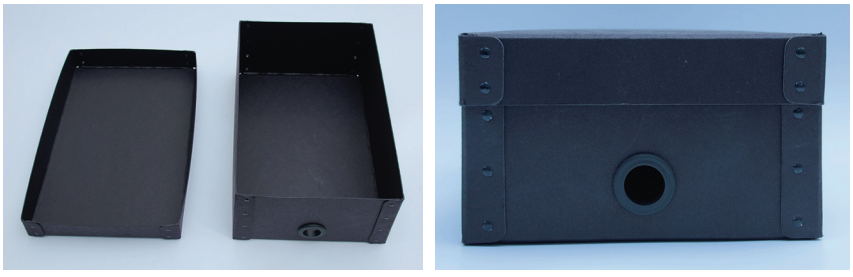

(a) (b)

Figure 1.20 A shoebox-like container, made of black cardboard with a small hole and a lid (a) resembles a cavity. Similar cavities are used as blackbody sources. The hole looks very black in the VIS, nicely illustrating the name *black*body (b).

3. Radiation emitted by a blackbody depends on wavelength; however, its radiance does not depend on direction, that is, it behaves like a Lambertian radiator.

As perfect absorbers and emitters, blackbodies serve as standards in radiometry.

Experimentally, the most simple commercial blackbodies are cavities whose walls are kept at constant temperature. The notion of black (as defined by property 1) can easily be understood from an optical analog in the visible spectral range. If one observes a distant building with an open window, the inner part of the window looks black indeed. A small box, preferably with inner black surfaces, with a small hole serves the same purpose (Figure 1.20).

1.3.2.2 Planck Distribution Function for Blackbody Radiation

Very precise spectral measurements of thermal radiation of cavities, that is, experimental blackbodies, existed by the end of the nineteenth century. However, it was not before 1900, when Max Planck introduced his famous concept of the Planck constant h, that measured spectra could be satisfactorily explained. Planck's theory was based on thermodynamics, but with the quantum nature of the emission and absorption of radiation, he introduced a totally new concept not only in the theory of blackbody radiation but in the whole world of physics. In modern language, the spectral excitance, that is, total radiant power into the hemisphere, of a blackbody of given temperature T in wavelength interval $(\lambda, \lambda + \mathrm{d}\lambda)$ can be written as

$$M_\lambda(T)\,\mathrm{d}\lambda = \frac{2\pi hc^2}{\lambda^5}\frac{1}{\mathrm{e}^{hc/(\lambda kT)} - 1}\,\mathrm{d}\lambda \tag{1.15}$$

The corresponding radiance is $L_\lambda(T) = M_\lambda(T)/\pi$. Here, $h = 6.626 \cdot 10^{-34}$ J s is Planck's constant, $c = 2.998 \cdot 10^8$ m s^{-1} is the speed of light in a vacuum, λ is the wavelength of the radiation, and T is the absolute temperature of the blackbody given in Kelvin. The currently accepted values for the fundamental physical constants such as c, h, and others can be found on the NIST web site [29].

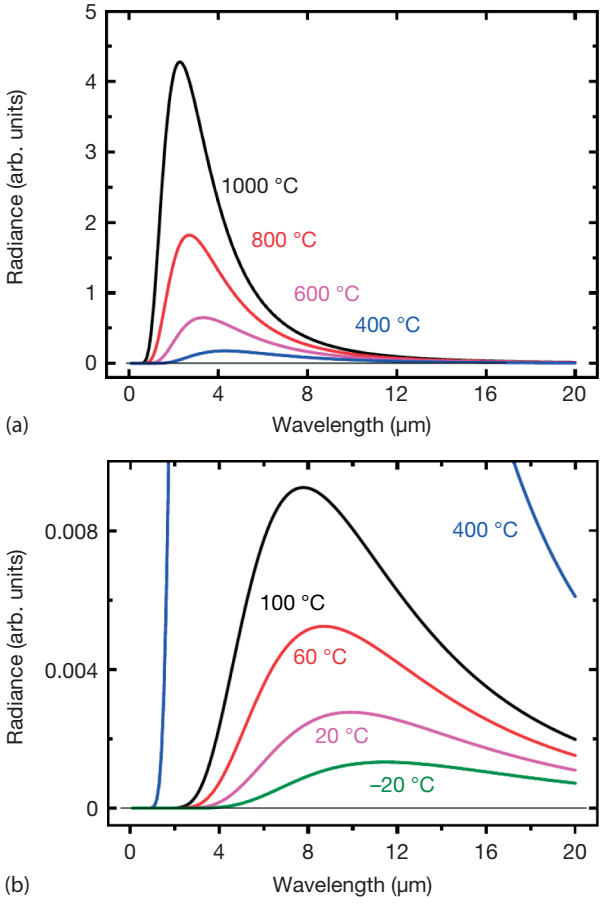

Figure 1.21 Radiance of blackbodies of temperatures between –20 and 1000 °C. Radiance is given in the same arbitrary units for (a) and (b).

Figure 1.21 depicts a series of blackbody spectra for various temperatures. The spectra refer to either radiance or excitance (the scale has arbitrary units; for absolute values see Figure 1.22). They have several characteristic features:

1. In contrast to emission from spectral lamps, these spectra are continuous.
2. For any fixed wavelength, radiance increases with temperature (i.e., spectra of a different temperature never cross each other).
3. The spectral region of emission depends on temperature. Low temperatures lead to longer wavelengths, high temperatures to shorter wavelength emission.

The wavelength of peak transmission in this representation is found by locating the maximum via the condition $\mathrm{d}M_\lambda(T)/\,\mathrm{d}\lambda = 0$. This leads to Wien's displace-

ment law:

$$\lambda_{\max} \cdot T = 2897.8\ \mu\text{m K} \tag{1.16}$$

For blackbodies at 300, 1000, and 6000 K, maximum emission occurs around 10, 3, and 0.5 µm, respectively. The first case resembles environmental radiation, the second, for example, a hot plate from an electric stove, and the third, the apparent average temperature of the outer layers of the Sun. From daily experience, hot plates start to glow red because the short-wavelength part of the thermal emission enters the red part of the visible spectrum. Radiation from the Sun appears white to us since it peaks in the middle of the visible spectrum.

1.3.2.3 Different Representations of Planck's Law

Besides the usual textbook representation of Planck's law in terms of radiance or excitance as a function of wavelength (Eq. (1.15)), other equations can be found illustrating the same phenomenon. Many spectrometers that are used to measure the spectra of blackbody radiation measure, for example, signals as a function of frequency $\nu = c/\lambda$ (in Hz) or wavenumber $\tilde{\nu} = 1/\lambda$ (in cm^{-1}). The corresponding representation of spectra reveals important differences compared to the wavelength representation. For example, Eq. (1.17) gives the frequency distribution of blackbody radiation:

$$M_\nu(T)\,\mathrm{d}\nu = \frac{2\pi h\nu^3}{c^2}\frac{1}{\mathrm{e}^{h\nu/(kT)} - 1}\,\mathrm{d}\nu \tag{1.17}$$

Figure 1.22 compares a set of blackbody spectra in terms of excitance (i.e., spectral emissive power) as a function of wavelength $M_\lambda\,\mathrm{d}\lambda$ and as a function of frequency $M_\nu\,\mathrm{d}\nu$ in double log plots. Similar to Wien's displacement law for wavelength (Eq. (1.16)), a displacement law also exists for the frequency representation:

$$\frac{\nu_{\max}}{T} = 5.8785 \cdot 10^{10}\ \text{Hz/K} \tag{1.18}$$

A note of caution: obviously the two representations have their peaks at different parts of the spectrum at the same temperature since the distribution functions include $\mathrm{d}\lambda$ and $\mathrm{d}\nu$, which are related via a nonlinear equation [30]. For example, $M_\lambda\,\mathrm{d}\lambda$ for $T = 5800$ K peaks in the VIS range at 500 nm, whereas $M_\nu\,\mathrm{d}\nu$ peaks at $3.41 \cdot 10^{14}$ Hz, which, according to $c = \nu\lambda$, corresponds to a wavelength of 880 nm. This behavior is a consequence of using distribution functions. One needs to be very careful when arguing about the maxima of Planck blackbody spectra. The position of a maximum actually depends on the chosen representation. For IR cameras, this has no effect, of course, since we are always interested in the total radiant power within a certain spectral interval; and, of course, in the total radiant power within a certain spectral range, for example, the VIS for $T = 5800$ K (or the range 8–14 µm for 300 K radiation or any other range) is the same in both representations.

Blackbody radiation is one of the few topics that have inspired several Nobel Prizes in physics. First, Wilhelm Wien received the prize in 1911 for his work

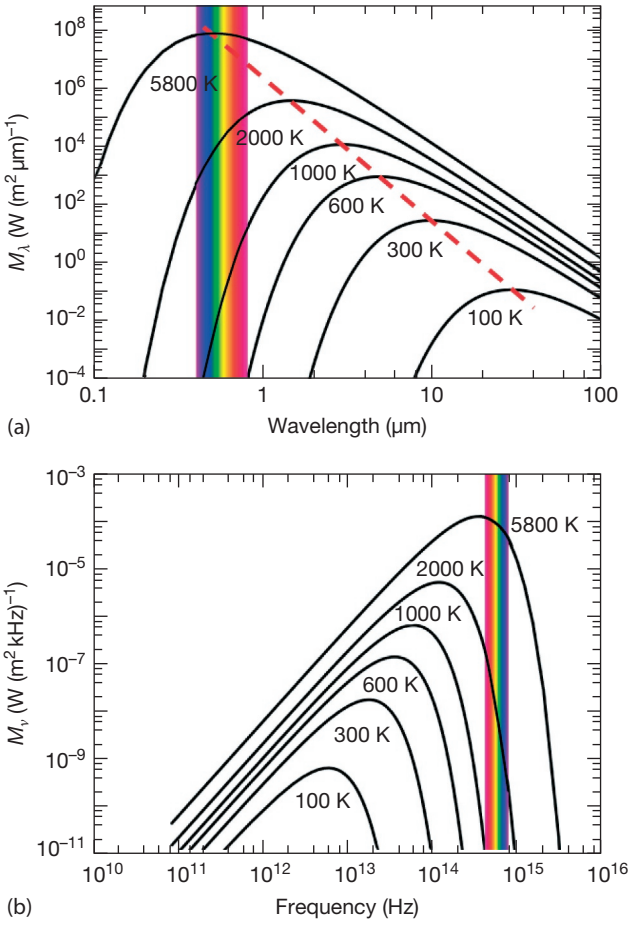

Figure 1.22 (a,b) Comparison of two representations of Planck's law for blackbody radiation. The maxima of the curves lie at different spectral positions, depending on the choice of the variable. The dotted line in the wavelength representation (a) gives the position of the maxima according to Wien's displacement law.

on thermal radiation, although it was Max Planck who finally solved the theoretical puzzle of correctly describing blackbody radiation. Nevertheless, Planck received the prize in 1918 for his general concept of the quantum nature of radiation, which had consequences reaching far beyond thermal radiation in the entire field of physics. The third prize in this field was awarded in 2006 to George Smoot and John Mather. They succeeded in recording the most famous blackbody radiation spectrum in astrophysics. This spectrum of cosmic background radiation is thought to resemble a kind of echo of the Big Bang of our Universe. It was recorded in the early 1990s by the NASA satellite COBE. Figure 1.23 depicts the results of this spectrum, which can be fitted with very high accuracy to a Planck function of temperature 2.728(±0.002) K.

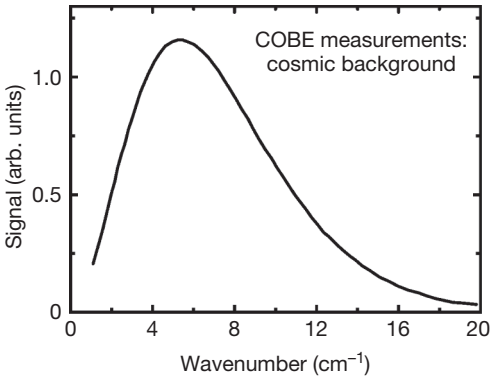

Figure 1.23 Cosmic ray background spectrum measured with COBE satellite. The theoretical fit refers to $T = 2.728$ K (Courtesy NASA).

Usually, only part of the spectrum of blackbody radiation is utilized in IR imaging. In the following two subsections, we deal with the total amount of radiation within certain spectral limits. The Stefan–Boltzmann law deals with the whole spectrum, extending from zero to infinity, whereas band emission is slightly more complicated.

1.3.2.4 Stefan–Boltzmann Law

The excitance of a blackbody source is calculated from

$$M(T) = \int_0^\infty M_\lambda(T)\,\mathrm{d}\lambda = \int_0^\infty M_\nu(T)\,\mathrm{d}\nu = \sigma T^4 \tag{1.19}$$

Here, $\sigma = 5.67 \cdot 10^{-8}\ \mathrm{W\,m^{-2}\,K^{-4}}$ denotes the Stefan–Boltzmann constant.

The area under the spectral excitance (spectral emissive power) curve (Figure 1.24) gives the excitance (emissive power), which depends exclusively on the temperature of the blackbody. Hence, the total radiance associated with blackbody radiation is M/π. In astrophysics, the Stefan–Boltzmann law is used to calculate the total energy production of stars, for example, of the sun, from its known surface area and surface temperature.

1.3.2.5 Band Emission

In IR imaging, one never detects radiation of the whole spectrum, but rather the radiation in a predefined spectral range, which is determined by the detector and material properties of the optics and the atmosphere. Unfortunately, the integral of Eq. (1.19) does not have analytical solutions for arbitrary values of lower and upper limits. To simplify the results, one defines a blackbody radiation function $F_{(0\to\lambda)}$ as the fraction of blackbody radiation in the interval from 0 to λ, compared

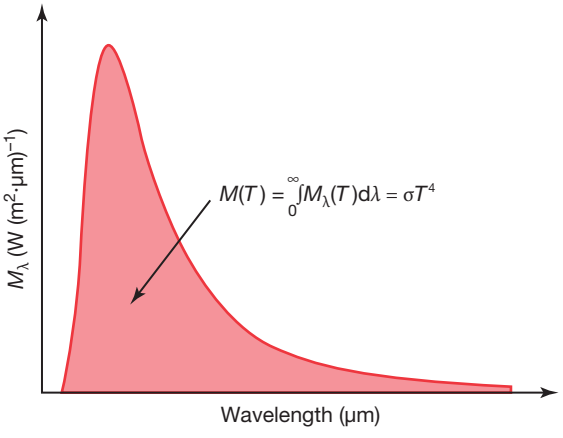

Figure 1.24 Visualization of Stefan–Boltzmann law.

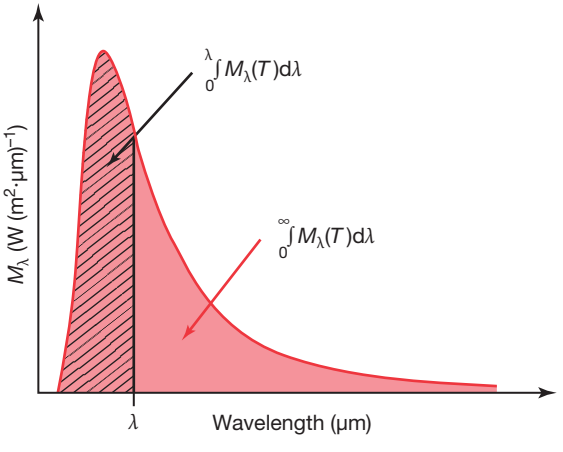

Figure 1.25 Definition of blackbody function: fraction of emitted excitance in spectral band (see text for details).

to the total emission from 0 to ∞ (Figure 1.25):

$$F_{(0\to\lambda)} = \frac{\int_0^\lambda M_\lambda \,\mathrm{d}\lambda}{\int_0^\infty M_\lambda \,\mathrm{d}\lambda} \tag{1.20}$$

We note that, unfortunately, view factors F_{ij} and this blackbody radiation function $F_{(0\to\lambda)}$ are denoted by the same letter F, the only difference being the subscripts. The context of the two quantities is, however, quite different and can be easily guessed from the subscripts. We therefore adopt this general similar notation for both.

The mathematical analysis shows that the integrand only depends on the parameter $\lambda \cdot T$; therefore, integrals can be evaluated numerically for this parameter,

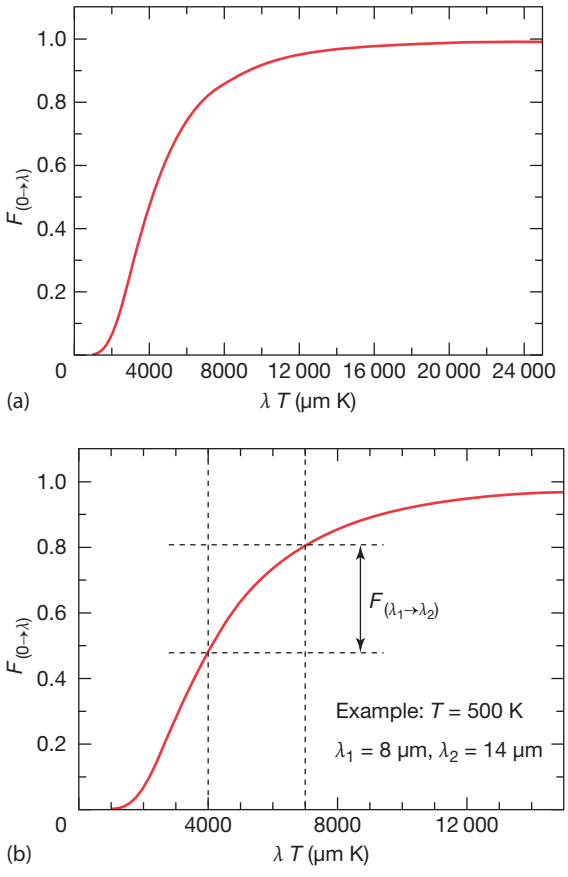

Figure 1.26 Fraction $F_{(0\to\lambda)}$ of excitance of blackbody radiation in wavelength interval 0–λ as function of λT (a) and how it can be used to estimate the fraction $F_{(\lambda_1\to\lambda_2)}$ in a wavelength interval λ_1–λ_2 (b).

and hence, $F_{(0\to\lambda)}$ is tabulated as a function of λT (e.g., [20]). Figure 1.26a depicts the corresponding results.

Obviously, the function $F_{(0\to\lambda)}$ can be easily used to calculate the fraction of blackbody radiation in an arbitrary wavelength interval (λ_1, λ_2):

$$\mathrm{F}_{(\lambda_1\to\lambda_2)} = F_{(0\to\lambda_2)} - F_{(0\to\lambda_1)} \tag{1.21}$$

Figure 1.26b illustrates an example of how quick graphical estimates of $\mathrm{F}_{(\lambda_1\to\lambda_2)}$ are possible for $T = 500$ K and a wavelength range between 8 and 14 μm. In general, a given temperature and wavelength range $\lambda_1 \to \lambda_2$ defines $\lambda \cdot T$ values (vertical broken lines). They intercept the $F(0, \lambda)$ curve at two specific values. Their difference (the distance between the horizontal broken lines) gives $F_{(\lambda_1\to\lambda_2)}$.

We present three examples for object temperatures of 300, 500, and 2800 K (Table 1.5). The fraction of blackbody radiation within the hemisphere of an object of

Table 1.5 Examples of band emission.

Range T	VIS $F_{0.38-0.78\,\mu m}$	SW $F_{0.9-1.7\,\mu m}$	MW $F_{3-5\,\mu m}$	LW $F_{8-14\,\mu m}$
300 K	$\approx 10^{-22}$	$\approx 3 \cdot 10^{-9}$	$\approx 1.3 \cdot 10^{-2}$	$\approx 37.6 \cdot 10^{-2}$
500 K	$\approx 10^{-12}$	$\approx 4 \cdot 10^{-5}$	$\approx 14.9 \cdot 10^{-2}$	$\approx 32.7 \cdot 10^{-2}$
2800 K	$\approx 9.9 \cdot 10^{-2}$	$\approx 43.6 \cdot 10^{-2}$	$\approx 9.2 \cdot 10^{-2}$	$\approx 0.84 \cdot 10^{-2}$

500 K in the LW wavelength interval is approximately 32.7%, but only 14.9% in the MW range. A very hot object, for example, a filament of a light bulb at a temperature of 2800 K, leads to a fraction of approximately 10.0% in the VIS wavelength interval, more than 43% in the SW infrared, and, similarly, approximately 9.2% in the MW range and less than 1% in the LW.

More examples of band emission and detection and further relevant radiometric quantities for complete IR camera systems will be discussed in Section 2.3.2.

1.3.2.6 Order-of-Magnitude Estimate of Detector Sensitivities of IR Cameras

Usually, blackbody radiators are used to calibrate IR cameras (Chapter 2). Using the concepts of radiometry and the laws of blackbody radiation, we can estimate the typical order of magnitude for the sensitivity of thermal radiation detectors, that is, how many watts of input power on a detector element are needed to detect, for example, a 1 K temperature difference between two objects. Consider, for example, a blackbody radiator of temperature T_{BB} at a distance of $R = 1$ m in front of a LW IR camera at ambient temperature T_{cam}. The blackbody radiator has a circular shape and diameter $2r_{BB} = 5$ cm, and the front lens of the IR camera should also have a diameter of $2r_{cam} = 5$ cm. The camera detects radiation in the spectral range from 8 to 14 µm.

The total radiant power that is incident on the camera from the object is given by Eq. (1.11):

$$d^2\Phi = L_1 \cos\delta_1 \, dA_1 \, d\Omega_2$$

Here, $\cos\delta_1 \approx 1$, the integral over the blackbody area gives $A_1 = \pi r_{BB}^2$, $L_1 = M_{BB}/\pi$, and $d\Omega_2 = \pi r_{cam}^2/R^2$. Therefore the spectrally integrated radiant power incident on the camera is given by

$$\Phi_{BB\to cam} = M_{BB}(T_{BB}) \frac{r_{BB}^2 \cdot r_{cam}^2 \cdot \pi}{R^2} \tag{1.22}$$

Of course, there is also a similar radiant power emitted from the detector toward the blackbody source; however, the corresponding contributions to Φ due to the detector temperature cancel since we are dealing only with changes in radiant power with object temperature. Therefore, this argument should also hold for all detector types (cooled as well as room-temperature ones).

In the following numerical example, we consider a LW camera system (a similar calculation can also be done for a MW or SW system). The emitted energy flux from a blackbody of temperature T_{BB} in the detector wavelength range is given by

$$\Phi_{BB\to cam} = \frac{r_{BB}^2 \cdot r_{cam}^2 \cdot \pi}{R^2} \int_{8\,\mu m}^{14\,\mu m} M_{BB}(T_{BB})\,d\lambda \tag{1.23}$$

The integral is given by $F_{(\lambda_1\to\lambda_2)}\sigma T^4$. Any further calculation requires numerical temperature values. For simplicity, let us assume $T_{BB1} = 303\,K$, $T_{BB2} = 302\,K$, since most detector sensitivities are rated at $T = 30\,°C$. The integral values can be easily derived from $F_{(\lambda_1\to\lambda_2)}$. For 303 and 302 K, they are very similar (0.378 and 0.377); therefore a single value of 0.38 is assumed.

In this case, the difference in incident radiative power for a variation from 303 to 302 K of the blackbody temperature is given by

$$\Delta\Phi \approx \frac{r_{BB}^2 \cdot r_{cam}^2 \cdot \pi}{R^2} \cdot F_{\lambda_1\to\lambda_2} \cdot \sigma \left(T_{BB1}^4 - T_{BB2}^4\right) \tag{1.24}$$

Inserting the preceding values, we find $\Delta\Phi/\Delta T = 2.9 \cdot 10^{-6}\,W\,K^{-1}$ (the total radiative power Φ_{BB} (8–14 μm) due to a blackbody of 303 K is about $2.2 \cdot 10^{-4}$ W).

A typical standard lens of an IR camera has an acceptance angle of 24°. At a distance of 1 m, the blackbody source will only occupy an angular diameter of 2.86°. If 24° corresponds to the 320 pixel width of the detector, the blackbody source will be imaged on an angular diameter of about 38 pixels, corresponding to a circular area with about 1140 pixels. This means that each pixel will receive on average a difference in radiant power of $2.54\,nW\,K^{-1}$.

These numbers are probably still a factor of at least 3 too large since, first, part of the radiation may be attenuated within the atmosphere on its way from the source to the camera (Section 1.5.2), second, the camera optics has a transmission smaller than 100%, and third, the active detector area is only about 50% of the complete pixel area. As a final result, one may expect values on the order of $1\,nW\,K^{-1}$ for the difference in radiative power received by each detector pixel for a 1 K difference. For a camera with the same 24° optics, but a 640 pixel width of the detector, values would be smaller by a factor of 4. We return to this estimate when discussing detectors and relate it to the noise-equivalent temperatures (Section 2.2.2).

One may gain confidence in this kind of estimate by similarly deriving the solar constant, that is, the total radiant flux onto an area of $1\,m^2$ outside of the (attenuating) atmosphere of the earth. Starting again with Eq. (1.11) and using $A_1 = \pi r_{sun}^2$, $L_1 = M_1/\pi$, and $d\Omega_2 = 1\,m^2/R_{sun-earth}^2$, we find

$$\Phi_{solar\ constant} = M_{BB}(T_{sun})\frac{r_{sun}^2 \cdot 1}{R_{sun-earth}^2} \tag{1.25}$$

$r_{sun} = 6.96 \cdot 10^5\,km$, $R_{sun-earth} = 149.6 \cdot 10^6\,km$, and $T = 5800\,K$ gives $\approx 1390\,W\,m^{-2}$, which, considering that the sun is not a true blackbody emitter, is a very good approximation for the solar constant.

1.4 Emissivity

1.4.1 Definition

Blackbodies are idealizations, and no real object can emit the maximum thermal radiation at a given temperature. The real emission of thermal radiation from any object can, however, be easily computed by multiplying the blackbody radiation by a quantity that describes the influence of the object under study, the emissivity ε. In other words: *the emissivity of an object is* the ratio of the amount of radiation actually emitted from the surface to that emitted by a blackbody at the same temperature.

Differing definitions of emissivity are possible (Eq. 1.26), depending on which quantity is used to describe the radiation. In radiometry, four definitions are used based on radiance L and excitance M. The relevant radiometric quantities are (i) spectral directional emissivity, (ii) spectral hemispherical emissivity, (iii) total directional emissivity, and (iv) total hemispherical emissivity.

They are defined as follows:
Spectral directional emissivity (L, spectral radiance)

$$\varepsilon(\lambda, \delta, \phi, T) = \frac{L(\lambda, \delta, \phi, T)}{L_{\mathrm{BB}}(\lambda, T)} \tag{1.26a}$$

Spectral hemispherical emissivity, directionally averaged (M, spectral excitance):

$$\varepsilon(\lambda, T) = \frac{M(\lambda, T)}{M_{\mathrm{BB}}(\lambda, T)} \quad \text{with} \quad M = \int_{\text{hemisphere}} L \cos\delta \, \mathrm{d}\Omega \tag{1.26b}$$

Total directional emissivity (wavelength averaged):

$$\varepsilon(\delta, \phi, T) = \frac{L(\delta, \phi, T)}{L_{\mathrm{BB}}(T)} \tag{1.26c}$$

Total hemispherical emissivity (wavelength and direction averaged):

$$\varepsilon(T) = \frac{M(T)}{M_{\mathrm{BB}}(T)} = \frac{M(T)}{\sigma T^4} \tag{1.26d}$$

Unfortunately, none of these definitions refers to the required conditions for practical IR imaging, where one first usually deals with objects that are observed near normal incidence or at small angles. Hence, a directional quantity, averaged over the desired angular range, is needed. Second, IR cameras operate at predefined wavelength ranges. Obviously, the required emissivity needs to be averaged over the desired wavelength range. Symbolically, we need an emissivity ε ($\Delta\lambda$,

$\Delta\Omega, T$). In practice, mostly the directional, near-normal emissivity is used, which is furthermore assumed to be independent of wavelength and temperature. We will return to the consequences of this for practical work at the end of this chapter.

1.4.2 Classification of Objects according to Emissivity

From the definition of emissivity it is clear that $0 \leq \varepsilon \leq 1$. Figure 1.27 illustrates spectral hemispherical emissivities and corresponding spectra of emissions of thermal radiation at given temperatures first for a blackbody, second for a so-called gray body with constant ε value, that is, ε is independent of wavelength, and third for a so-called selective emitter where ε varies as a function of wavelength.

For most practical applications in thermography, ε is independant of wavelength resembling a gray body. Whenever substances are studied that have absorption and emission bands in the thermal IR spectral range, for example, gases or plastic foils, one must deal with selective emitters, which may complicate the quantitative analysis.

1.4.3 Emissivity and Kirchhoff's Law

The emissivity can be guessed from *Kirchhoff's law* (e.g., [20, 31]), which states that the amount of radiation absorbed by any object is equal to the amount of radiation that is emitted by this object. This is usually written in the form

$$\varepsilon = \alpha \tag{1.27}$$

where ε and the so-called absorptivity α denote the fraction of radiation that is either emitted or absorbed. Energy conservation requires that any radiation (Φ_0) incident on any object must be reflected (Φ_R) (whether it is directed according to the law of reflection or diffusely scattered from rough surfaces), transmitted (Φ_T) through the object, or absorbed (Φ_A) within the object:

$$\Phi_0 = \Phi_R + \Phi_T + \Phi_A \tag{1.28a}$$

Considering the fraction of the incident radiation (e.g., in excitance or radiance), this law reads

$$1 = R + T + \alpha \tag{1.28b}$$

where R and T denote the fraction of radiation that is either reflected or transmitted. Combining Eqs. (1.27) and (1.28b) allows for estimates of the emissivity ε. The simplest examples are opaque solids with $T = 0$. In this case,

$$\varepsilon = 1 - R \tag{1.29}$$

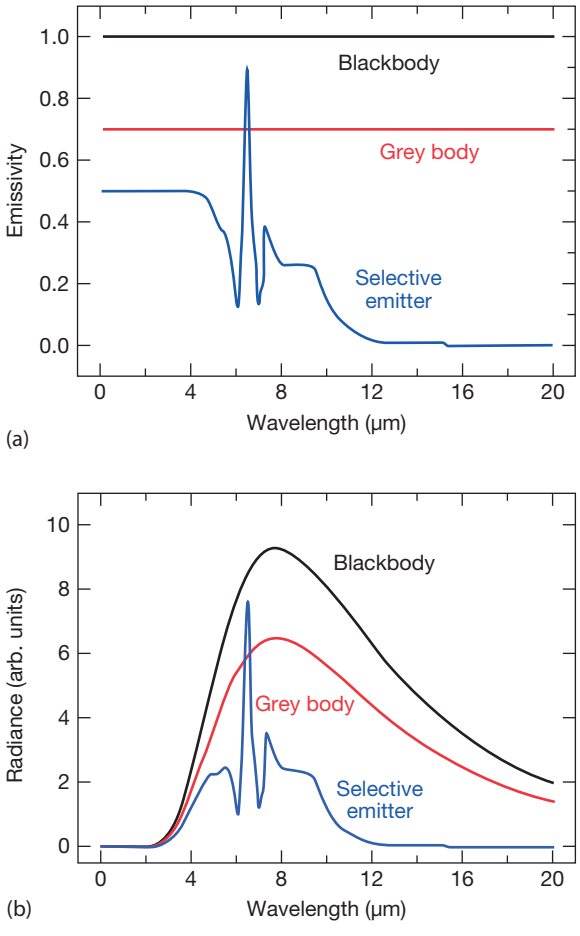

Figure 1.27 Spectral hemispherical emissivities (a) and corresponding thermal radiation (b) spectra for blackbodies, gray bodies, and arbitrary selective emitters.

that is, the emissivity follows directly from known values for the total reflectivity. It is important to note that R includes not only directed reflectivity (Figure 1.9), as is usual for polished surfaces, but also diffuse reflectivity (Figure 1.11), which additionally occurs for rough surfaces. Equation 1.29 makes it possible to guess ε values. For example, glass, which is more or less opaque in the IR with reflectivities in the IR range of a small percentage, will have emissivities of $\varepsilon > 0.95$. In contrast, metals with high reflectivities above 90% will have emissivities below 0.1. Some very well-polished metal surfaces can have the lowest possible emissivities of order 0.01, which practically render IR imaging impossible.

Table 1.6 Parameters that affect emissivity ε.

Intrinsic object properties	Variations due to other parameters
Material (e.g., metal, insulator)	Regular geometry (e.g., grooves, cavities)
Surface structure (rough/polished)	Wavelength (e.g., LW/MW/SW)
Observation direction (viewing angle)	Temperature (e.g., phase changes)

1.4.4 Parameters Affecting Emissivity Values

As a material property, the emissivity depends on the following parameters (Table 1.6).

1.4.4.1 Material

The major parameter is the kind of material. Depending on the measurement techniques used, averages are taken over certain angular and spectral ranges as is useful in thermography. In a simplified classification, one can separately discuss nonmetals and metals, because – fortunately – most nonmetallic materials that are needed for practical thermography applications like skin, paper, paints, stones, glass, and so on are gray emitters and have fairly high emissivity values of above 0.8. In contrast, metals and, in particular, polished metals pose problems owing to their often very low emissivities with values below 0.2.

1.4.4.2 Irregular Surface Structure

For any given material, the emissivity may vary considerably as a result of the surface structure. This leads to the unfavorable situation where, for the same material, many different values for emissivity are reported. This effect is most pronounced for metals. Whereas some polished metals can reach values of ε as low as 0.02, the emissivity can be much larger and even reach values above 0.8 if the surfaces are roughened. The highest values for originally metallic parts are found where the surfaces are modified via oxidation/corrosion over the course of time. Imagine, for example, a metallic bolt of an electrical connection that is operated for many years while being exposed to the elements, oxygen from the air, water from rain, and so on. A value as high as 0.78 has been reported for strongly oxidized Cu and 0.90 for some steel compounds owing to such chemical modifications of the surface. This factor is most important for any inspection of, for example, bolts, nuts, electrical clamps, and similar parts in electrical components since a thermographer must have criteria for determining whether a components fails or passes. Therefore, a quantitative analysis is necessary, that is, one must know the exact temperature difference of these components compared to their surroundings of known emissivity, and the measured temperature will very strongly depend on the actual value of emissivity.

To illustrate the effect of material as well as surface structure on emissivity, we used a so-called Leslie cube. This is a hollow copper metal cube (with a side length of around 10 cm) whose side faces are treated in different ways. One side is covered with a white paint, one with black paint, one is not covered but just resembles polished copper, and the fourth side consists of roughened copper.

The cube is placed on some Styrofoam as thermal insulation and then filled with hot water. Owing to the good thermal conductivity of the metal, all the side faces of the cube will quickly have the same temperature. The emission of thermal radiation by each side face can easily be analyzed with an IR camera. Figure 1.28 depicts some results (for details of how temperatures are calculated within the used LW camera, see Section 2.3).

For the two painted side faces, the chosen ε value of 0.96 produced more or less the correct temperature (as can be verified by a contact probe). The rough copper surface had much less emission of thermal radiation and the polished copper surface even less. Using the camera software, one can adjust the emissivity values such that the copper surfaces also give the correct value of the wall temperatures. For our example we find emissivities of the polished copper surface to be around 0.03 and of the roughened copper surface to be about 0.11.

Figure 1.28 illustrates one way of finding correct values for emissivities: measure object temperatures with a contact probe, then adjust the emissivity in the camera until the camera shows the correct temperature reading (assuming, of course, that all other camera parameters are chosen correctly; see Section 2.3).

1.4.4.3 Viewing Angle

We have defined *emissivity* as the ratio of the amount of radiation actually emitted from a surface to that emitted by a blackbody at the same temperature. In particular, the spectral directional emissivity (Eq. 1.26a) is the ratio of the radiance of the radiation, emitted at given wavelength λ and in a direction defined by the two angles δ and φ (Figure 1.15), to the radiance emitted by a blackbody at the same temperature and wavelength.

Blackbodies behave like perfect isotropic emitters, that is, the radiance of any emitted radiation is independent of the direction in which it is emitted (compare the discussion of Lambertian radiators, Figure 1.17). Unfortunately, any real surface shows a different behavior, that is, its radiance shows variations depending on the direction of emission. This is schematically illustrated in Figure 1.29. In addition to the fact that any real surface emits less radiation than a blackbody at the same temperature (left side: red solid line), the radiance from a real gray object usually also depends on the angle of emission. In Figure 1.29, this manifests itself as a deviation between the real radiance (right side: solid blue line) and the Lambertian behavior of a gray object (right side: red broken line). Azimuthal symmetry is assumed in Figure 1.29, hence only the angle δ is shown.

This behavior can strongly affect any contactless temperature measurement using IR cameras, since an object that is observed from a direction normal to its surface ($\delta = 0°$) will emit more radiation than when observed at oblique angles. This means that the emissivity depends on the angle of observation with respect

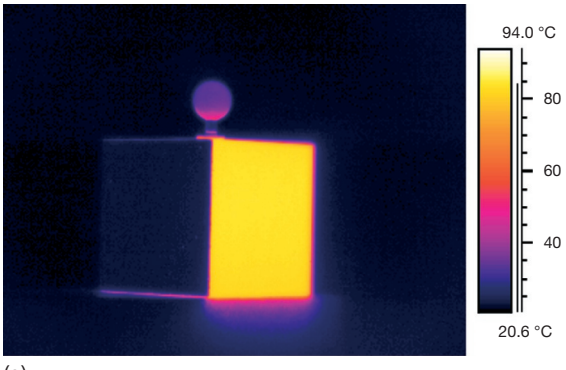

(a)

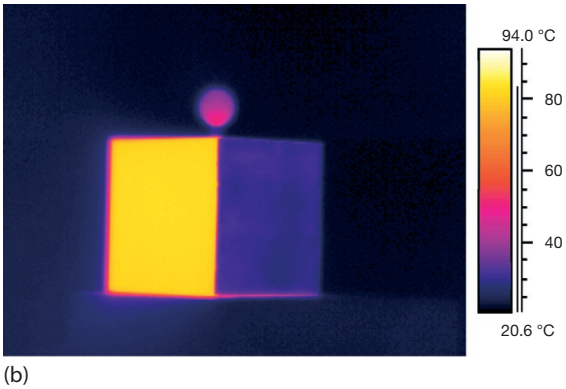

(b)

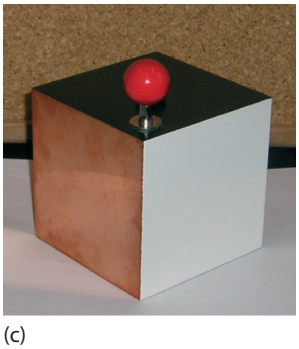

(c)

Figure 1.28 (a,b) Leslie cube, filled with hot water and viewed at an angle of 45° with respect to the side faces. The emissivity of the whole image was set to $\varepsilon = 0.96$, resulting in the following temperature readings (left to right). (a) Polished copper ($T = 22.6\,°C$), white paint ($T = 84.3\,°C$). (b) Black paint ($T = 83.4\,°C$), roughened copper ($T = 29.3\,°C$). The knob on top is a stirrer for reaching thermal equilibrium faster. (c) Visible image of such a cube.

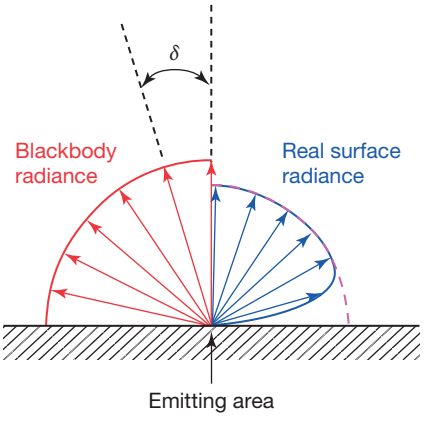

Figure 1.29 Schematic illustration of angle-independent radiance for blackbodies (left/red) and directionally dependent radiance of real surfaces (right side/blue).

to the surface normal. Fortunately, many measurements have been performed and a wide variety of materials has been studied in relation to their directional emissivities. A typical setup for such an experiment is shown in Figure 1.30a.

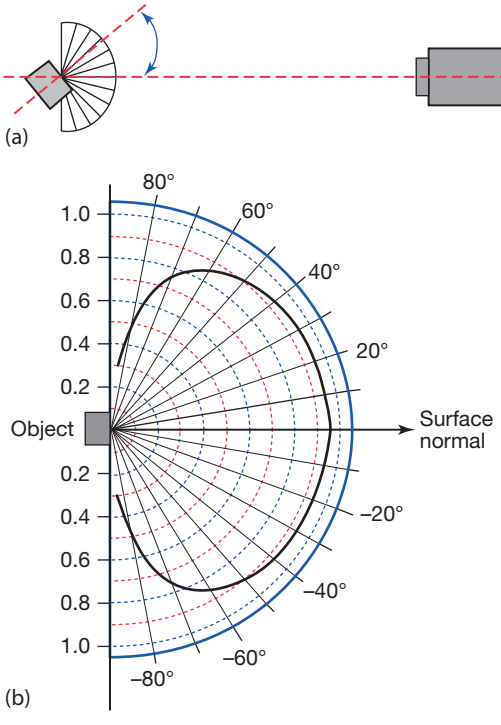

Figure 1.30 A Leslie cube with a painted side face (high emissivity) was used as object to measure the directional emissivity (averaged in the LW range) as a function of the viewing angle from 0 to 85° with respect to the surface normal. The cube was rotated with respect to the camera (a) and temperatures recorded. (b) The emissivity as a function of the viewing angle was then found by varying the emissivity in the camera software until the temperature readings of the rotated side face gave correct values.

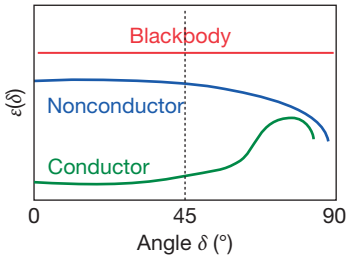

Figure 1.31 Overview of typical directional dependence of emissivities of nonconductors and conductor with respect to blackbodies.

An angular scale from 0 to 180° is attached to a table with 90° pointing to the IR camera. The (warm or hot) object to be studied is placed on top of the scale with its surface normal facing 90°, that is, the IR camera. Then measurements of the emitted radiation are recorded as a function of the angle while rotating the object. In Figure 1.30b, we show an example for the white paint side of a Leslie cube that was filled with hot water. The actual surface temperature can be measured by contact thermometry, which gives the correct value of the normal-direction emissivity. The angle-dependent values are found by changing the emissivity value in the camera software until the real temperature is shown (for details of signal processing in the camera, see Chapter 2). Another experiment on $\varepsilon(\delta)$ is discussed in Section 5.5.5.

Figure 1.30b nicely demonstrates an effect that fortunately holds for nearly all practically important surfaces: the emissivity is nearly constant from the normal direction 0° to at least 40° or 45°. The behavior at larger angles differs for metallic and nonmetallic materials (Figure 1.31). For nonconductors, one observes a characteristic drop of ε for larger angles, whereas metallic surfaces usually show first an increase toward larger angles before decreasing again at grazing incidence [7, 20, 32].

Neglecting diffuse reflections for the moment, this behavior can already be understood from the characteristic properties of directed reflection for different polarizations of radiation. Figure 1.32 schematically depicts plots for the portion R of directly reflected radiation in the IR spectral region for nonmetals and metals with polished surfaces (similar to Figure 1.12) as a function of the angle of incidence.

The directed reflectivity depends on the polarization of the radiation. Unpolarized radiation is characterized by the broken line, which represents the average of both polarizations. Obviously, the reflectivity for nonconductors exhibits a monotonous increase with angle of incidence, whereas metals show first an decrease before increasing again at larger angles. This characteristic feature (which can be explained theoretically by the Fresnel equations) explains the observed angular plots of emissivity, since $\varepsilon = 1 - R$ for opaque materials according to Eq. (1.29). However, we also note that most metallic objects have rough surfaces, which induce additional contributions to the emissivity and which can also induce changes in the observed angular distributions.

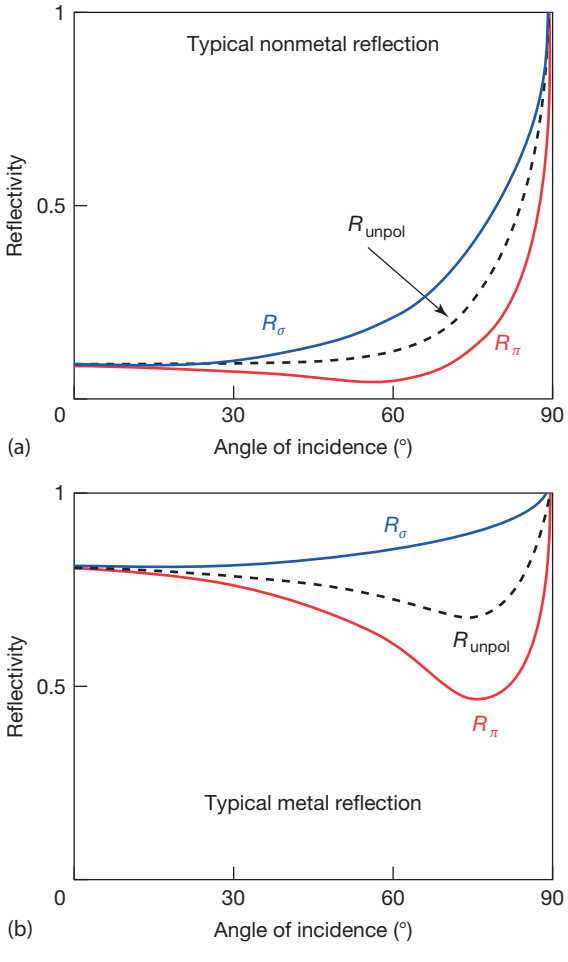

Figure 1.32 Schematic plot of reflectivities of polarized and unpolarized IR radiation of metals (a) and nonmetals (b) as a function of the angle of incidence.

1.4.4.4 Regular Geometry Effects

The geometry of a surface is related to the surface structure; however, in contrast to irregular surface roughness (Section 1.4.4.2), here we refer to well-defined geometric structures like grooves, which are used to systematically change emissivity. Cavities are discussed in detail separately in the context of blackbody calibration sources (Section 1.4.6).

Consider a polished metal surface (of, for example, $\varepsilon_{\text{normal}} = 0.04$) with a well-defined surface structure in the form of grooves of a given slope angle (Figure 1.33, here with an apex angle of 60°).

The grooves enhance the emissivity in the vertical direction, that is, perpendicular to the macroscopic surface, as can be understood from the following argument.

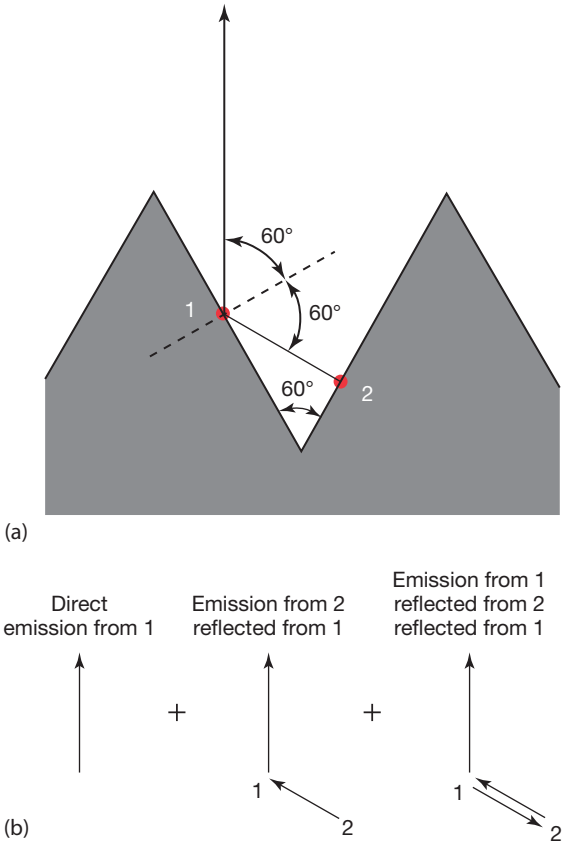

Figure 1.33 V-groove model of a polished metal surface with low emissivity (a). The macroscopic surface is horizontal. There are three contributions to radiance and, hence, emissivity for the groove surface in the vertical direction (b).

Radiation that is emitted from spot 1 in a direction normal to the macroscopic groove surface is composed of three radiance contributions:

1. Direct radiation emitted from spot 1: this contribution is characterized by $\varepsilon(60°)$ with regard to the real groove surface;
2. Radiation emitted from spot 2, which is then reflected from spot 1 in the normal direction: this contribution is characterized by $\varepsilon(0°) \cdot R(60°) = \varepsilon(0°) \cdot [1 - \varepsilon(60°)]$ with regard to the groove surface;
3. Radiation emitted from spot 1 in direction of spot 2, reflected back from spot 2 to spot 1, and then reflected in the normal direction: this contribution is characterized by $\varepsilon(60°) \cdot R(0°) \cdot R(60°) = \varepsilon(60°) \cdot [1 - \varepsilon(0°)] \cdot [1 - \varepsilon(60°)]$ with regard to the groove surface.

Adding up these radiance contributions and dividing by the blackbody radiance, one can easily see that the normal emissivity of the grooved surface has increased.

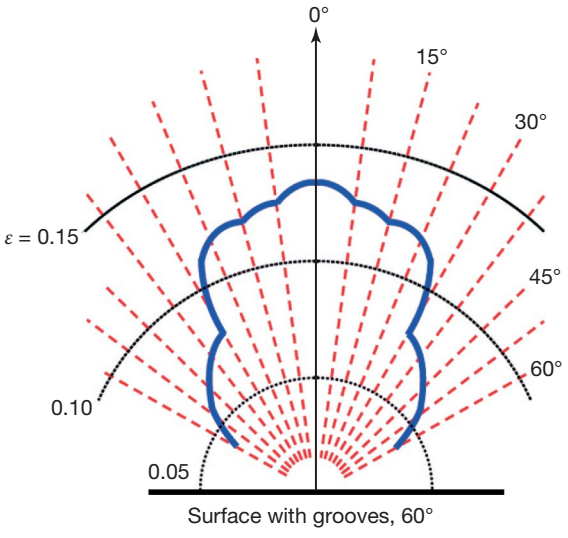

Figure 1.34 Polar diagram for expected dependence of emissivity as a function of observation angle for 60° V-groove model of a polished metal surface with flat surface emissivity of 0.04 (after [33]).

For a numerical estimate, we assume a polished surface emissivity of $\varepsilon(0°) = 0.04$ and $\varepsilon(60°) = 0.05$. In this case, the total normal emissivity of the grooved surface $\varepsilon_{\text{total,normal}} = 0.04 + 0.04 \cdot (1 - 0.05) + 0.05 \cdot (1 - 0.04) \cdot (1 - 0.05) = 0.124$, that is, the emissivity has increased by a factor of nearly 3 owing to this surface structure. The basic idea behind this enhancement explains why any rough surface has a higher emissivity than polished flat surfaces.

Regular surface structures often lead to nonuniform angular distributions of emissivity. Repeating the preceding calculation for different emission angles [33] with respect to the macroscopic groove surface (Figure 1.34) reveals strong variations of emissivity as a function of observation angles.

1.4.4.5 **Wavelength**

As is well known in optics, material properties usually depend on wavelength. Consider, for example, the reflectivity of the noble metals gold (Au), silver (Ag), and copper (Cu). Au and Cu have electronic interband transitions in the VIS range, which give rise to the wavelength-dependent reflectivities, finally resulting in the characteristic golden-yellow as well as red-brown color of these metals. Reflectivity is strongly related to the emissivity of materials, so any wavelength dependence on reflectivity will also show up in emissivity. Detailed theoretical arguments are beyond the scope of this book, so we refer the interested reader to the corresponding literature [20, 31, 34, 35] and give schematic diagrams of how the emissivities of certain materials change in general (Figure 1.35).

As can be seen from Figure 1.35, the emissivity of metals usually decreases with wavelength (an effect opposite to that of reflectance), whereas oxides and other

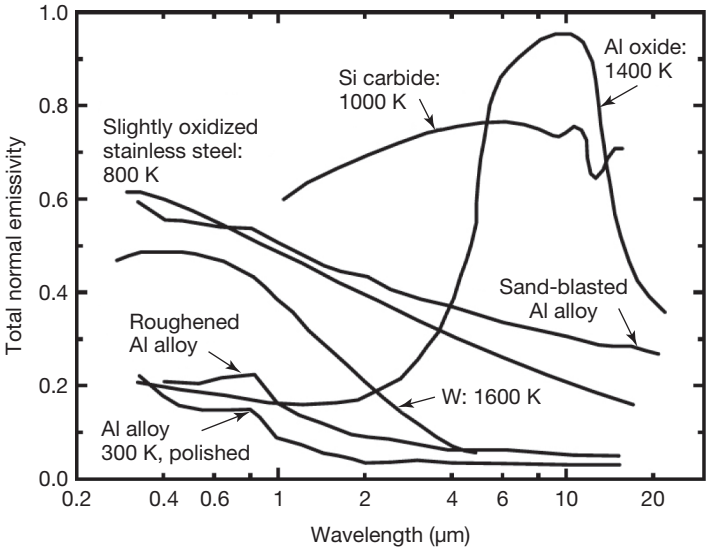

Figure 1.35 Examples of wavelength dependence of normal emissivity for different materials (after [20, 31]).

nonmetals can show increases as well. The examples of aluminum alloys clearly emphasize the effect that increasing surface roughness from polished surfaces to those roughened by grid paper or finally being sand blasted leads to drastic increases of emissivity. Whenever dealing with substances that have wavelength-dependent emissivity, one must first determine whether emissivities are constant in the IR camera spectral range being used. If not, it is advisable to use narrow-band filters or another wavelength band for thermography where emissivities are nearly constant. If this is not possible, one must be aware that any quantitative analysis will be much more complicated since signal evaluation must then use the known variation of emissivity.

We finally mention that in addition to these slowly varying emissivities as a function of wavelength, there are several examples of selective absorbers and emitters such as plastic foils or many gaseous species. These have special applications in IR imaging and are treated in detail in other chapters (Chapter 8, Section 10.8).

1.4.4.6 **Temperature**

Material properties usually change with temperature, and it is no surprise that this also holds for emissivity. Figure 1.36 gives some examples. Some materials show fairly strong variations, so it may be necessary for practical purposes to know whether the temperature of a process under IR observation will remain within a certain temperature interval such that the emissivity for this study can be considered constant. In addition, if the literature values for emissivity are used, one must know the corresponding temperatures. Particular care should be taken when

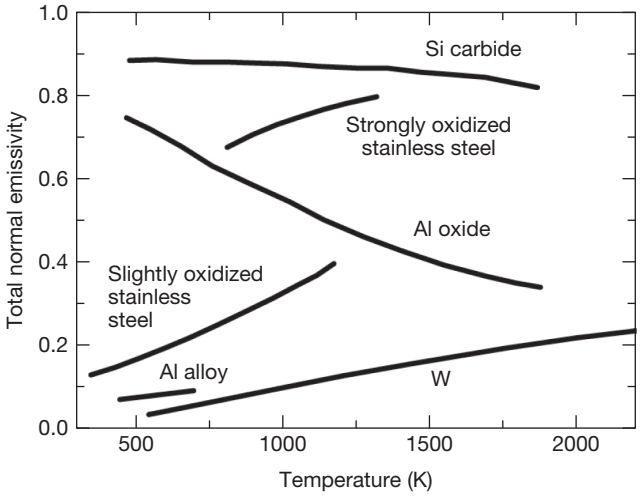

Figure 1.36 Examples of temperature dependence of emissivity for different materials (after [20, 31]).

studying materials that undergo phase changes, for example, when observing the melting of metals.

1.4.4.7 **Conclusion**

The material property of emissivity, which is essential in IR imaging, depends on many parameters. Accurate temperature measurement with thermography requires precise knowledge of this quantity. Several sets of tables of emissivities for various materials are available in books [1, 10, 23, 31] and from the manufacturers of related camera systems. Unfortunately, these cannot be used without a word of caution. Measurements always refer to specific experimental conditions, for example, temperature range, wavelength range (LW, MW, SW), or angles (directional or hemispherical measurement). These three factors are usually not critical since, for most (not all) practical cases in thermography, wavelength and temperature dependencies are not relevant. Furthermore, most practical emitters show directional dependencies only for observation angles larger than 45° with respect to the surface normal. This means that we mostly deal with gray objects of nearly Lambertian behavior whose emissivity can be guessed within a certain range of accuracy.

Unfortunately, however, metallic objects pose severe problems. Polished metals have very small values of emissivity. Small variations in ε can cause large errors in temperature; therefore, the smaller the emissivity, the more precisely must its value be determined (see also discussion in Section 2.3.3). This poses serious challenges since polished metals have ε values that are quite different compared to roughened or oxidized ones. In electrical inspections, one may often deal with highly oxidized or corroded metallic parts. In such cases, guessing the emissivity from tables may lead to results that are quite erroneous [36, 37]. In addition,

the metal industry (e.g., aluminum or steel production) may also need to consider variations of emissivity with temperature.

1.4.5 Techniques to Measure/Guess Emissivities for Practical Work

Owing to the problems in guessing accurate values for emissivity, it is common practice to measure ε directly. This can be done in various ways; some of those often used are listed in Table 1.7. In all cases, by "emissivities" we mean directional near normal emissivities, which are integrated over the selected wavelength range of the IR camera.

The easiest method is to attach tape or paint of known emissivity to the object under study. In the analysis, the surface temperatures of the tape or paint follow from their known ε. Assuming good thermal contact and waiting until thermal equilibrium is established, adjacent surface temperatures of the object are assumed to be the same; hence, the object emissivity is found by varying ε in the camera software until the object temperature is equal to known tape surface temperature. The accuracy of this method depends on the accuracy of the known emissivity. Owing to the lab measurements, they are related to the temperature accuracy of the contact probe (thermocouple).

One may also directly measure several spot surface temperatures with thermocouples and use them to calibrate the IR images. In this case, one must make sure that good thermal contact is achieved, thermal equilibrium is established, and – which is crucial for small objects – that the thermocouple itself does not change the object temperature via heat conduction. A useful condition is that the heat capacity of the thermocouple must be much smaller than that of the object. This method need not, but may, be more time consuming if objects made of many

Table 1.7 Some practical methods of adjusting normal emissivities in thermography.

Method	Tape	Paint, correction fluid, and so on	Contact thermometer	Hole drilling
Equipment needed	Tape	Paint	Thermocouple	Electric drill
Idea behind method	Known emissivity from lab experiments, calibrated with contact probe (usually thermocouple)		Spot measurements with contact probe	Known increased emissivity due to cavity effect
Advantage/disadvantage	Nondestructive, removable, problem of good thermal contact for very rough surfaces	Nondestructive, problem in removing paint, works also for rough surfaces	Nondestructive, may be time consuming	Destructive, independent of object surface structure

different materials are investigated. Also, one must make sure that no thermal reflections are present in IR images (Section 3.4) since these would introduce errors into the analysis.

Sometimes, in building thermography, one may have the chance to drill a hole in the wall, thereby creating a cavity with very high emissivity values that can then be used in images for a correct temperature reading. In a manner similar to the tape method, emissivity can then be estimated for adjacent regions.

1.4.6 Blackbody Radiators: Emissivity Standards for Calibration Purposes

In IR imaging, all commercial camera manufacturers must calibrate their cameras such that the user will be able to obtain temperature readings in IR images whenever the proper emissivity is chosen. In addition, some research cameras must be calibrated by the users themselves.

Calibration is usually done by observing the best available experimental approximations to blackbody radiation, so-called blackbody calibration standards. The national institutes that are responsible for standards (e.g., in the USA, NIST, in Germany, PTB) have developed standards (e.g., $\varepsilon > 0.9996$ in the form of heat pipe cavity-type blackbodies [38]). Commercial blackbody radiators, in particular, large area instruments, are used as secondary standards by IR camera manufacturers and other users in laboratory experiments (Figure 1.37). They can be tracked back to the primary cavity-type standards but usually have smaller emissivities of around $\varepsilon = 0.98$. They are made of high-emissivity materials with additional surface structures (e.g., pyramids) whose surfaces are temperature stabilized.

The principle for achieving high emissivities for primary standards is based on Kirchhoff's law (Eq. (1.27)). One needs to construct an object that has high absorptivity. As mentioned earlier, when introducing blackbody radiation, an open window of a distant building usually looks very black. The reason for this is illustrated in Figure 1.38.

Radiation is directed into the hole of an otherwise opaque cavity whose walls are stabilized at a given temperature. There is a certain absorption per interaction with the wall, and the radiation will be gradually attenuated. Usually, the inner surface is not polished, that is, it is not a reflecting surface according to the law of reflection (Eq. (1.2)) but rather it is diffusely scattering (Figure 1.11). If the hole is small compared to the total surface area of the cavity, the radiation will undergo many absorption losses before there is a chance of its leaving the cavity again through the entrance hole. For example, if $\alpha = 0.5$ (absorptivity of 50% per interaction), the radiation will be attenuated after 10 reflections already to $(0.5)^{10}$, which is less than 10^{-3}. This means that the overall absorptivity is larger than 99.9%, and therefore the corresponding emissivity has the same value.

The same thing happens, of course, to any radiation that is thermally emitted within the cavity. It interacts with the inner walls many times before leaving the cavity through the only hole. This is why such cavities are considered to be perfect emitters of thermal radiation. As a matter of fact, attempts to explain the results of

(a) (b)

(c)

Figure 1.37 Photograph of two commercial secondary standard blackbody source with $\varepsilon = 0.98$. (a,b) With circular symmetry structures, which are visible at grazing incidence. (c) Without structures.

very accurate cavity measurements of thermal radiation led Planck to his famous radiation law.

Many different geometries and sizes of cavities and holes have been studied (Figure 1.39) for a variety of different materials over the years [1, 31]. The simple geometries of sphere and cylinder are usually replaced by either conical shapes or at least cylinders with conical end faces. For high-emissivity sources, the inner surfaces are rough and of materials with high emissivity (see also Section 5.5.4).

It is now easy to generate very high emissivities, but it has also been shown that, using low ε wall materials, it is possible to design cavities with intermediate emissivity values in the range 0.3–0.7 [39]. As an example, Figure 1.40a shows the

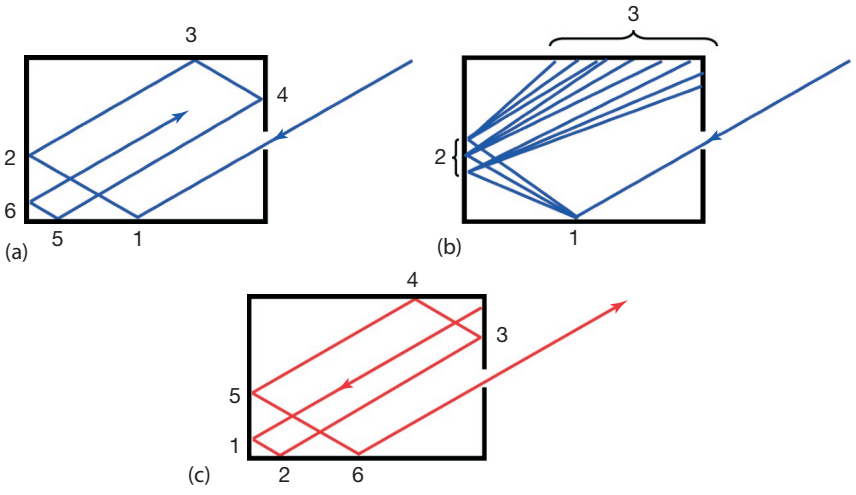

Figure 1.38 A cavity with a hole can trap incident radiation (blue) even if the absorption per interaction with the surface is small since radiation undergoes many reflections before there is a chance of being emitted again (a). If the inner surfaces are diffusely reflecting (b), the effect is even stronger. Similarly, any thermal radiation emitted from some spot on the wall (c, red) will be in thermal equilibrium before leaving the opening.

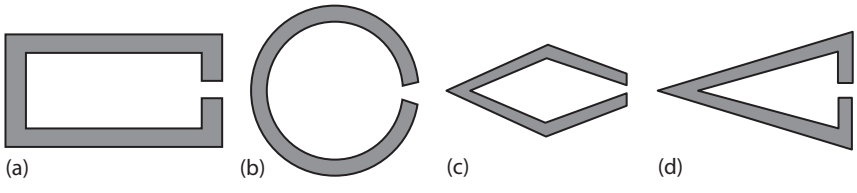

Figure 1.39 Various geometries for cavity blackbody radiators.

geometry of a polished metal cavity. Figure 1.40b depicts the resulting theoretical emissivity as a function of material emissivity, and Figure 1.40c demonstrates the effect of cavity geometry on the resulting emissivity. The latter result is easy to understand: the larger the inner surface area, the lower the chance of radiation hitting the small-opening hole, hence the larger the emissivity.

Polished wall materials within well-defined geometries do, however, have the side effect of angular dependence of emissivity. As illustrated in Figure 1.34, there are specific angles at which more (or less) radiation is emitted with regard to other angles. These so-called geometrical resonances are illustrated in Figure 1.41, which depicts IR measurement results from the heated cavity shown in Figure 1.40 for $L = 5\,\text{mm}$.

In conclusion, for cavity blackbody sources, whenever the inner surfaces are made of polished metals, it may be possible to obtain low and medium emissivities in the range 0.2–0.6; however, the directional character of emissivity usually still shows up, that is, the cavities do not yet resemble Lambertian sources. The

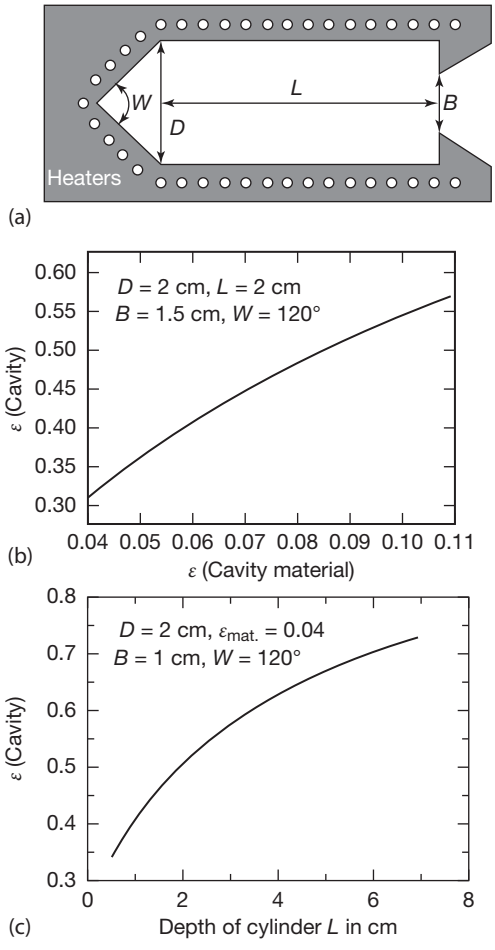

Figure 1.40 (a–c) Design of a blackbody radiator cavity and theoretical expectations for cavity emissivities as function of wall material and geometry.

best high-emissivity Lambertian blackbody sources are made of cavities with wall materials of high emissivity in the first place, perhaps additionally roughened.

Finally, a rather recent new development of a large area, high-emissivity blackbody was developed for in-flight blackbody calibration of an interferometer on research airplanes. It consists of 49 aluminum pyramids having a Nextel coating with $\varepsilon > 0.967$ from 5 to 12 μm and covering an area of $126 \cdot 126\ \text{mm}^2$. Three different pyramid base types – all with steep angles of around 80° – were arranged to form light traps. In this way, a large area blackbody with an emissivity exceeding 0.9996 could be designed (Figure 1.42) [40].

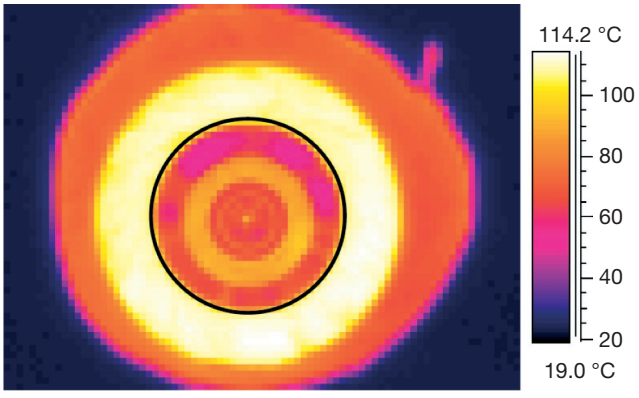

Figure 1.41 Geometrical resonances in emissivity of metallic cavities. The black circle indicates the size of the aperture.

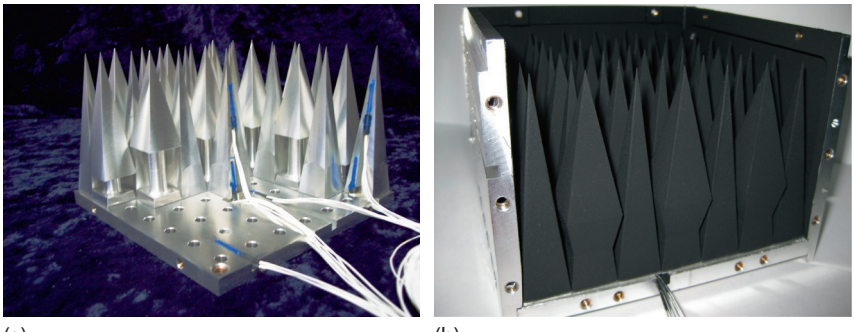

(a) (b)

Figure 1.42 Pyramid-based blackbody calibration source for airborne instruments (after [40]. Image courtesy F. Olschewski).

1.5 Optical Material Properties in IR

In any practical contactless temperature measurement with either pyrometry or IR imaging, the radiation from an object under study must reach the detector. However, this requires the IR radiation to pass through the space between object surface and detector within the camera housing (Figure 1.43). The radiation is usually attenuated on this path since it must pass through various kinds of matter, usually at least the gaseous atmosphere and the solid focusing optics materials. Additional solid materials, for example protection windows, can lead to additional attenuation and thermal reflections and – if at elevated temperatures – to additional emission of thermal radiation, which may contribute to the object signal. Certain special applications may include additional matter between object and detector, such as other gases, liquids, or additional solid filters.

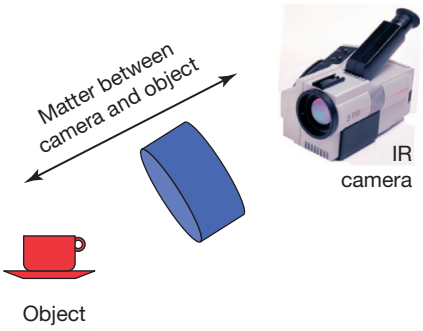

Figure 1.43 Typical setup for thermography. The object is observed through matter, which can be a gas, a liquid, or a solid material, so it can become attenuated. The same holds for the camera optics in front of the detector.

Here, we summarize optical material properties due to the atmosphere and common solid window or lens materials in the thermal IR spectral range. Additional materials, for example special gases or plastics, are dealt with separately in Chapter 8 and Section 10.8. More information can be found in the literature [1, 4, 12, 13, 17, 31, 41–43].

1.5.1
Attenuation of IR Radiation while Passing through Matter

The most common case is the study of objects already present in the atmosphere, that is, objects and the camera already immersed in a gas. IR radiation is emitted from the object surface into the atmosphere. Once the scattering, absorption, or emission processes within the gas are known, one may calculate the modification of the object IR radiation.

Similarly, for any kind of solid material, incident radiation will be modified as it is regularly reflected, diffusely scattered, absorbed, or emitted (Figure 1.44).

In most cases, emission can be neglected. A general treatment of attenuation of IR radiation must therefore be able to compute absorption/scattering within matter as well as reflection losses at material boundaries.

Attenuation of radiation along its original direction within matter is described by the Bouguer–Lambert–Beer law (Eq. (1.30)), which yields the transmitted portion T of the radiance as a function of traveled distance d within matter:

$$T(\lambda, d) = \frac{I(\lambda, d)}{I(\lambda, 0)} = \mathrm{e}^{-\gamma(\lambda)\cdot d} \tag{1.30}$$

Here, $\gamma(\lambda) = \alpha(\lambda) + \sigma(\lambda)$ denotes the total attenuation coefficient, which is due to the absorption (α) of radiation as well as scattering (σ), that is, a change in the direction of radiation. Both absorption and scattering can be calculated from first principles. In gases, both are due to electronic, vibrational, or rotational excitations, and γ can be expressed as

$$\gamma_{\mathrm{gases}}(\lambda) = n \cdot (\sigma_{\mathrm{abs}}(\lambda) + \sigma_{\mathrm{sca}}(\lambda)) \tag{1.31}$$

where n is the volume concentration of the gas (in number of particles/volume), and σ_{abs} and σ_{sca} are the so-called absorption and scattering cross sections. Re-

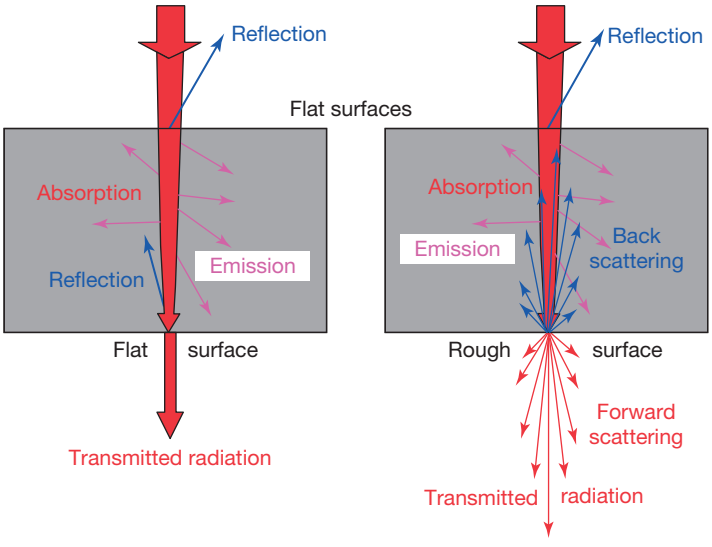

Figure 1.44 IR radiation that is incident on matter with flat surfaces can be reflected, absorbed, or emitted. For rough surfaces, diffuse scattering may take place.

sults for atmospheric gases – in the thermal IR range these refer more or less exclusively to ro-vibrational excitations – are known from many laboratory experiments (Chapter 8).

For solid matter, attenuation is due to excitations within electronic bands and lattice vibration processes. The attenuation coefficient in nondiffusely scattering solids (e.g., glasses or crystalline materials with polished surfaces) can be related to a macroscopic well-known quantity, the imaginary part of the index of refraction $n = n_1 + \mathrm{i}n_2$ (Eq. (1.32)):

$$\gamma_{\text{solids}}(\lambda) = \alpha_{\text{solids}}(\lambda) = \frac{4\pi \cdot n_2}{\lambda} \tag{1.32}$$

The index of refraction has been measured for many solids and is tabulated in a series of handbooks [18].

1.5.2 Transmission of Radiation through the Atmosphere

The dry atmosphere is composed of several natural gases (Table 1.8). In addition, there is a varying amount of water vapor of several percent volume concentration. Atomic gases (e.g., Ar) and diatomic gases of the same atomic species (N_2 and O_2) cannot absorb IR radiation in the thermal IR range. However, molecules, made up of two or more different atomic species, for example, NO, CO, CO_2, CH_4, and, of course, H_2O, are, in principle, able to absorb IR radiation. Figure 1.45 depicts two overview transmission spectra of horizontal atmospheric paths of lengths 10 and 1000 m, demonstrating that mostly CO_2 and H_2O dominate attenuation in

Table 1.8 Composition of dry air (for CO_2, August 2016: http://www.esrl.noaa.gov/gmd/ccgg/trends/).

Gas	Symbol	Volume (%)	Concentration (ppm)
Nitrogen	N_2	78.08	–
Oxygen	O_2	20.95	–
Argon	Ar	0.93	–
Carbon dioxide	CO_2	0.040 2	402
Neon	Ne	0.001 8	18
Helium	He	0.000 5	5
Methane	CH_4	0.000 19	1.9

otherwise pure air. Aerosols and clouds can induce additional attenuation (see also Section 11.5.1).

Several characteristic absorption features are present, in particular, some bands around 2.7 µm (H_2O and CO_2), around 4.2 µm (CO_2), between 5.5 and 7 µm (H_2O), and above 14 µm (H_2O, CO_2). These absorption bands are important for defining the spectral bands of IR cameras (Figure 1.8).

In addition to Table 1.8, there are gases with lower concentrations like krypton (Kr), hydrogen (H_2), nitrous oxides (N_2O, NO), xenon (Xe), ozone (O_3), and so on. The composition depends on the height above sea level. Some gas concentrations vary with time, e.g. the current increase in CO_2 is about 2 ppm/year, and for methane it is about 7 ppb/year.

Several computer models compute very precise transmission spectra of IR radiation within the atmosphere, the best-known being the Low Resolution Transmittance (LOWTRAN), Moderate Resolution Transmittance (MODTRAN), or High Resolution Transmittance (HITRAN) codes. These radiative transfer models for the atmosphere incorporate absorption and scattering constants for all relevant gaseous species in the atmosphere, and they also include vertical distributions of the constituents in order to provide an adequate modeling for the gas attenuation. LOWTRAN is a low-resolution propagation model and computer code for predicting atmospheric transmittance and background radiance. MODTRAN is similar to LOWTRAN, but with better spectral resolution. Similarly, HITRAN works with even higher resolution. The 2004 HITRAN model included 1 734 469 spectral lines for as many as 37 different molecules. For IR imaging, however, we mostly deal with two species and a few spectral bands, as shown in Figure 1.45.

Two aspects are particularly important for practical IR thermography. First, attenuation depends on the concentration of the absorbing gas species (Eq.(1.31)). For most gases of the atmosphere, concentrations are constant or slowly varying with time; water vapor, however, can have strong fluctuations; therefore, the relative humidity is an important quantity that needs to be measured for accurate compensation of water vapor attenuation between object and camera. Second, attenuation depends on the distance from an object to the camera (Eq.(1.30)), so

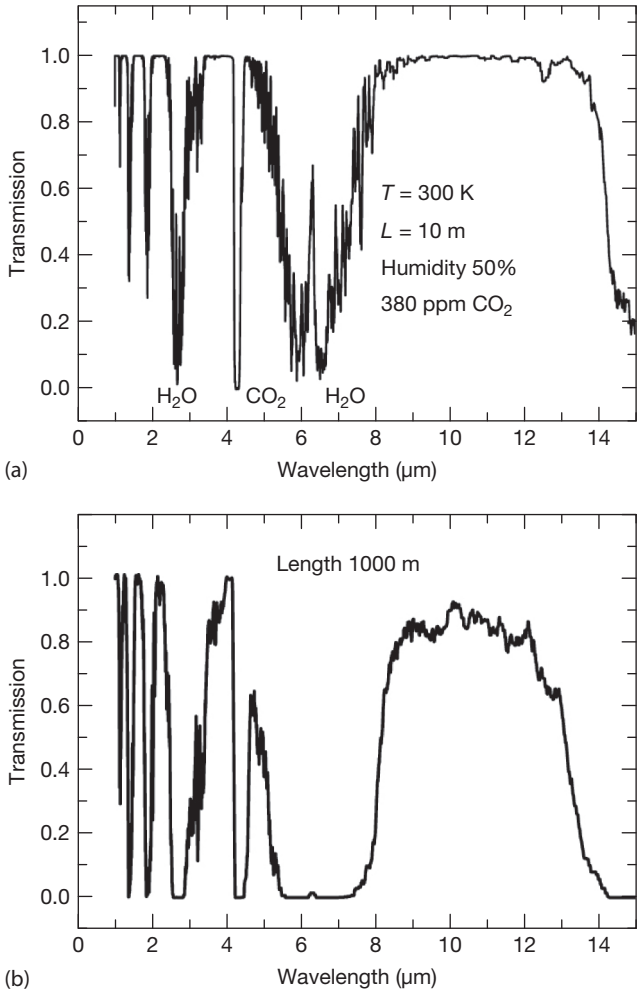

Figure 1.45 Atmospheric transmission $T(\lambda)$ for (a) 10 m and (b) 1000 m horizontal atmospheric paths. The spectra are nearly identical for the meanwhile slightly changed CO_2 concentration (400 rather than 380 ppm).

this quantity also needs to be known. Both humidity and distance are input parameters within the camera software packages.

Finally, for long atmospheric paths (e.g., hundreds of meters to kilometers) that are not usually encountered in thermography, additional effects due to aerosol scattering may become important, and the corresponding modeling must then include aerosol size and height distributions. If particles are small, as is the case, for example, in typical haze with water droplets of, say, 500 nm, visible light is scattered very effectively, whereas longer IR radiation is much less affected (Chapter 6, Section 10.9.2).

1.5.3
Transmission of Radiation through Slablike Solid Materials

1.5.3.1 Nonabsorbing Slabs

The attenuation of IR radiation in solid materials happens, for example, for lenses in IR cameras, but quite often objects are also observed through some windows. Mostly, flat (polished) surfaces are used such that scattering from surface roughness is neglected. The attenuation is then due to reflection at the boundaries as well as to absorption within the material. For the sake of simplicity we now discuss planar geometry, that is, slabs of material of a given thickness and well-defined index of refraction and IR radiation at normal incidence. For camera lenses with curved surfaces, one should redo the argument for finite angles of incidence. In this case, reflection coefficients will change according to the Fresnel equations, giving rise to polarization-dependent effects (Figures 1.12 and 1.32). However, if the distance from the object to the lens is large compared to the diameter of the lens, then the angles are small, and the general argument will still be valid.

Consider first a slab (coplanar plate) of a nonabsorbing material surrounded by a nonabsorbing material, usually the atmosphere (Figure 1.46). IR radiation of radiance L_0 is incident at normal incidence (in Figure 1.46, the propagation is drawn at oblique angles in order to visualize the various contributions separately).

In the simplest description (Figure 1.46a), there will be reflection losses L_R (characterized by the reflectivity $R = L_R/L_0$) of the radiation at the first interface. If the losses are small, the wave encounters similar losses at the second interface, that is, the total losses amount to about $2RL_0$ and the total transmission $T_{total} = L_{trans}/L_0$ can be written as $T_{total} \approx 1 - 2R$, with R from Eq. (1.5). A typical example for visible light and a glass plate in air would be $n_{air} = 1.0$, $n_{glass} = 1.5 + i0.0$, $R = 0.04$, and $T_{total} \approx 0.92$. This means that a typical glass plate transmits about 92% of incident visible light, which is why we can see quite clearly through windows. Before turning to IR windows, let us briefly generalize this result.

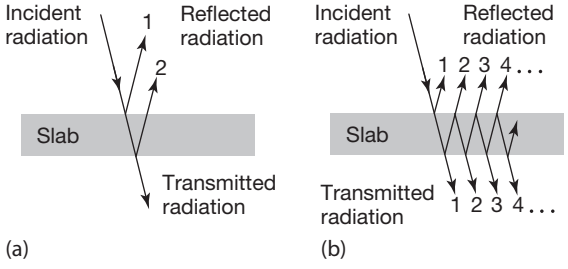

Figure 1.46 Scheme for calculating transmission of a slab in air. (a) Simplest approximation for small losses. (b) Complete analysis including all reflection contributions. The propagating radiation is drawn as oblique lines for clarity. In the calculation, however, they are assumed to be at normal incidence.

If the reflection losses upon hitting the first interface become larger (which will be the case for most IR transparent materials in the IR region), the derivation for the transmission must take into account all contributions of multiple reflections. Figure 1.46b depicts the idea behind the calculation. Part of the incident radiation is reflected at the first encounter with the slab. Using the symbols $R = L_R/L_0$ and $T = L_T/L_0 = (1 - R)$ for reflectivity and transmission at a single interface, this first reflection contribution (1) is given by $L_0 \cdot R$. The transmitted part $L_0 \cdot T$ enters the medium, which is initially assumed to be nonabsorbing. After the second transmission, and exiting the material, the radiance has decreased to $L_0 \cdot T^2$ (transmitted beam number 1). Following the beam, which is internally reflected within the slab, and subsequently studying more reflections and transmissions upon interactions with the slab surfaces, we end up with a number of rays (1, 2, 3, 4, …) contributing to the total reflected radiance and to the total transmitted radiance. For nonabsorbing materials, $T = 1 - R$; hence, the sum of all reflected contributions can be written as a geometrical sum

$$T_{\text{slab}} = (1 - R)^2 \cdot (1 + R^2 + R^4 + R^6 + \ldots) = \frac{(1 - R)^2}{1 - R^2} \tag{1.33}$$

Using Eq. (1.5) again for the air–glass example ($n_A = 1.0, n_B = 1.5 + \text{i}0.0$), the transmission can easily be evaluated to give

$$T_{\text{slab}} = \frac{2n_B}{n_B^2 + 1} \tag{1.34}$$

For $n_B = 1.5$ this gives $T_{\text{slab}} = 0.923$, which is only slightly higher than the previously estimated 0.92 value.

In contrast, a material like germanium at a wavelength of 9 μm has $n_B \approx 4.0 + \text{i}0.0$. The simple derivation of a Ge slab in air would give $T_{\text{total}} = 1 - 2 \cdot 0.36 = 0.28$, whereas the correct treatment according to Eq. (1.34) gives $T = 0.47$.

1.5.3.2 Absorbing Slabs

The propagation of radiation within an absorbing slab has the same type of contributions as in Figure 1.46b, the only difference being that during each successive passage through thickness d of the slab, there will be an additional attenuation described by Eq. (1.30).

Repeating the preceding calculation of the transparent-slab transmission and inserting R from Eq. (1.5) we finally find the transmission of an absorbing slab ($n_B(\lambda) = n_1(\lambda) + \text{i}n_2(\lambda)$) in air ($n_{1A} = 1$):

$$T_{\text{slab}}(\lambda, d) = \frac{16n_1^2 \cdot \text{e}^{-(4\pi n_2 d)/\lambda}}{\left[(n_1 + 1)^2 + n_2^2\right]^2 - \left[(n_1 - 1)^2 + n_2^2\right]^2 \cdot \text{e}^{-(8\pi n_2 d)/\lambda}} \tag{1.35}$$

Equation 1.35 makes it easy to compute slab transmission spectra, provided the thickness d of the slab as well as the optical constants $n_1(\lambda)$ and $n_2(\lambda)$ of the slab material are known.

1.5.4
Examples of Transmission Spectra of Optical Materials for IR Thermal Imaging

1.5.4.1 Gray Materials in Used IR Spectral Ranges

A number of common materials are available in the thermal IR spectral range [4, 9, 17]. These include crystals like BaF_2, NaCl, CdTe, GaAs, Ge, LiF, MgF_2, KBr, Si, ZnSe, and ZnS, and inorganic as well as organic glasses like fused silica IR grade or AMTIR-1. The materials can be characterized according to the corresponding wavelength range in which they are used. A number of examples are presented in what follows.

Figure 1.47a depicts the transmission, reflection, and absorption spectra for a 7.5 mm slab of NaCl. Obviously, NaCl has an excellent IR transmission of greater

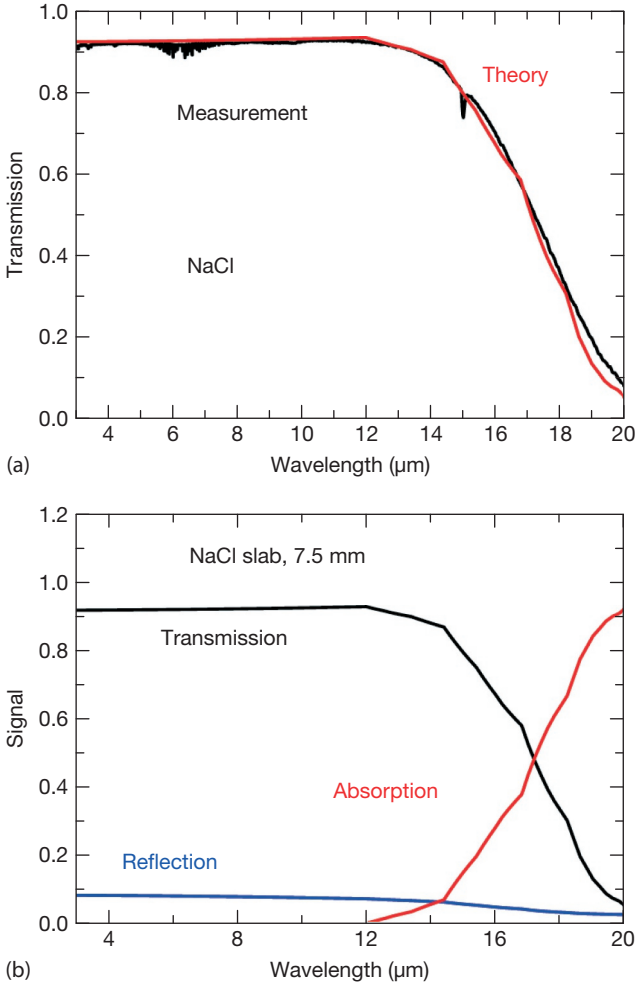

Figure 1.47 Experimental (black) and theoretical (red) transmission spectra of a 7.5 mm thick slab of NaCl (a) as well as the reflection and absorption contributions (b).

than 0.90 up to about 12 μm, and it still has a transmission of about 0.87 at 14 μm. The transmission depends on the slab thickness wherever absorption plays a role, here for $\lambda > 12$ μm. However, NaCl – as well as other alkali halides – has the disadvantage of being hygroscopic, that is, it must be protected from water moisture and humidity. Therefore, alkali halides are not used to manufacture lenses for IR camera systems. They are, however, sometimes used as special windows.

As is the case with all literature data, a word of caution is necessary for the theoretical spectra. Accurate measurements of optical constants of materials are difficult, and those collected over the years were subsequently refined after better sample preparation techniques became available. All of the following theoretical plots are based on the collection of data of optical constants from the literature [18]. Often, several slightly different sets of data are available. This is due to the fact that such measurements are usually made under ideal conditions, for example, clean samples, very good crystal or sample film quality, very few surface defects, scratches, and so on, with little sideways scattering. Hence, when comparing these data to real-world windows or lenses of the same materials, several percent deviations are common; in the case of severe surface damage with considerable side scattering, even larger deviations are possible. Hence, theoretical spectra should be regarded as order-of-magnitude expectations, and experimental spectra should be recorded for comparison whenever quantitative analysis is needed. In Figure 1.47b, the comparison of experimental spectra, recorded with Fourier transform infrared (FTIR) spectroscopy, and theoretical spectra based on tabulated optical constants shows very good agreement.

All data presented here refer to normal incidence. Spectra for obliquely incident radiation must take into account polarization-dependent effects described by the Fresnel equations (Figure 1.32). Lenses, windows, and filters for IR cameras are

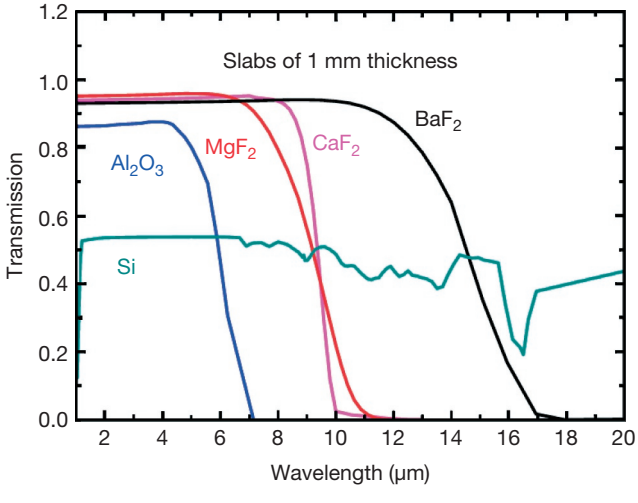

Figure 1.48 Overview of typical theoretical transmission spectra for 1 mm thick slabs of various materials that are used in the MW IR spectral region.

often manufactured from materials like BaF_2, CaF_2, MgF_2, Al_2O_3 (sapphire), and Si for a wavelength range up to 5 µm and Ge, ZnS, and ZnSe for the LW region. Some of these ideally suited materials for IR imaging are manufactured by special hot-pressing techniques and have special names like Irtran (acronym for IR transmitting).

Figures 1.48 and 1.49 show some examples of transmission spectra of materials that are used in the MW range.

Similar to the NaCl results (Figure 1.47), absorption features become important for longer wavelengths. In this case, the transmission spectra depend on the material thickness, as shown for BaF_2 and MgF_2 in Figure 1.49. Therefore, it is important to know the exact thickness of windows made of such materials if the

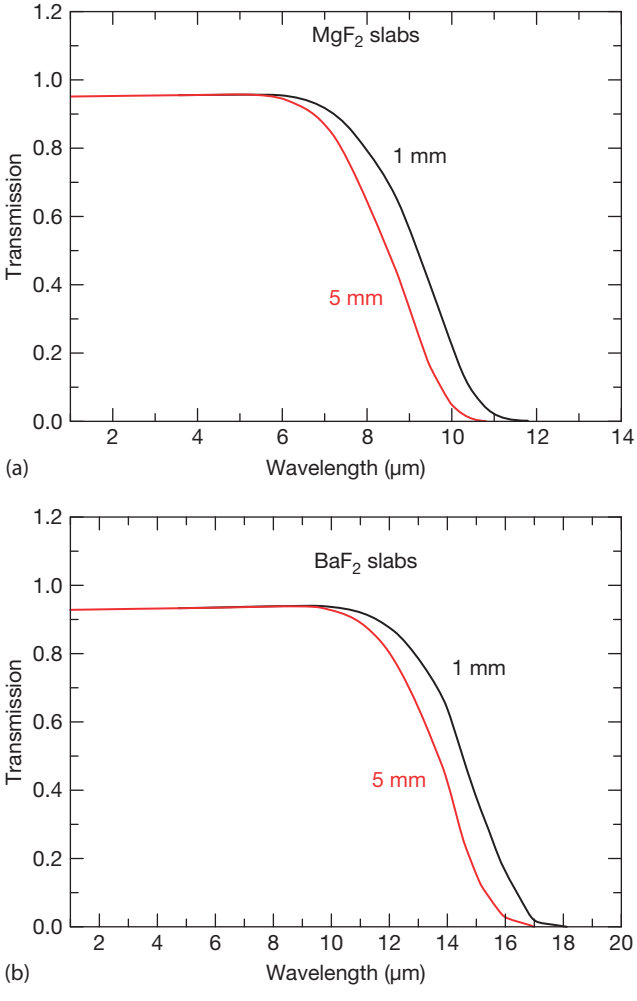

Figure 1.49 Transmission spectra depend on the thickness of the slabs owing to the onset of absorption.

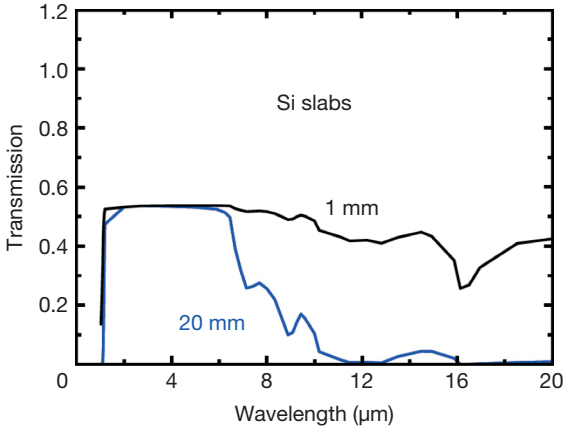

Figure 1.50 Transmission spectra of silicon slabs for different thicknesses. Absorption features are prominent for wavelengths above 5 μm.

IR camera used is sensitive in the corresponding spectral range of absorption features. Obviously, BaF_2 may also be used for LW cameras; however, one must take care to keep the thickness of window materials small.

Figure 1.51 provides an overview of spectra for materials that can be used in the LW range.

Figure 1.48 proves that the transmission for silicon is rather flat in the MW range; however, absorption features dominate the spectra in the LW range. This is illustrated in Figure 1.50, which presents a closer look of a silicon plate for different thicknesses. In the last few decades, the purity of silicon crystals has improved considerably. This means that high-quality oxygen-free silicon crystals may have appreciably less absorption than the sample shown here, which is based on a compilation of measured optical data from 1985 [18].

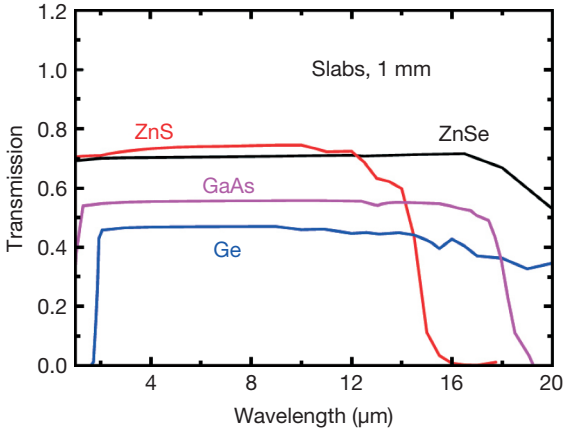

Figure 1.51 Overview of typical theoretical transmission spectra for 1 mm thick slabs of various materials that are used in the LW IR spectral region.

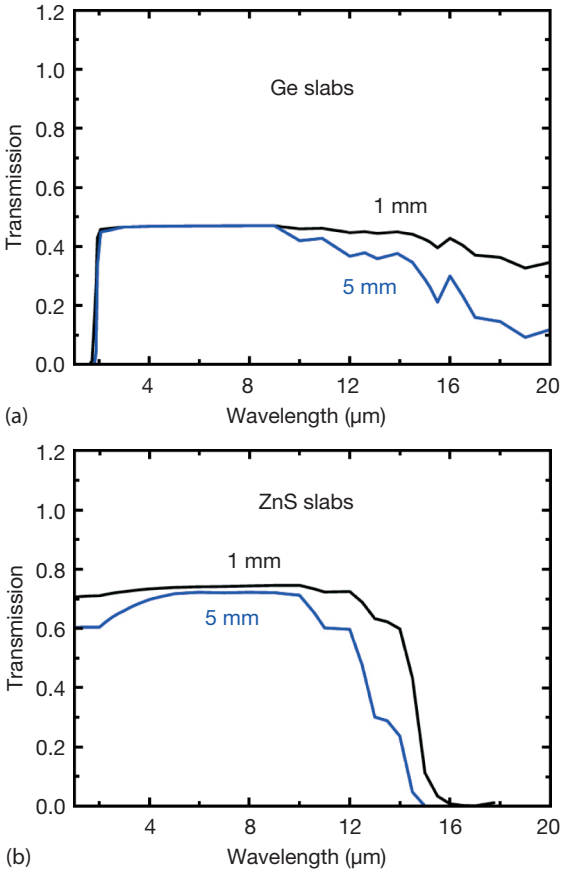

Figure 1.52 Transmission spectra of Ge (a) and ZnS (b) depend on slab thickness owing to onset of absorption.

It is should be mentioned that some of these materials have special trade names if manufactured in a certain way. For example, hot-pressed polycrystalline ZnS with about 95% cubic and 5% hexagonal crystals was called Irtran-2 by the manufacturer Eastman Kodak. Similar other trade names exist, like Irtran 4 for ZnSe, and so on. Since optical properties depend on crystalline structure, mixtures of different crystal forms can lead to differences in optical transmission spectra. ZnSe can be used throughout the LW range; for ZnS or Ge, however, thick samples show significant absorption features even below wavelengths of 15 μm (Figure 1.52). This effect is less pronounced for GaAs; however, GaAs is very expensive compared to the other materials, which affects its commercial use for lenses.

For comparison, Figure 1.53 depicts the respective spectra for regular laboratory glass BK7 (Schott) or fused silica, that is, amorphous silicon dioxide. Obviously, common glass cannot be used in either MW or LW IR cameras. Synthetic fused silica can, in principle, be used for MW systems, acting as bandpass filters.

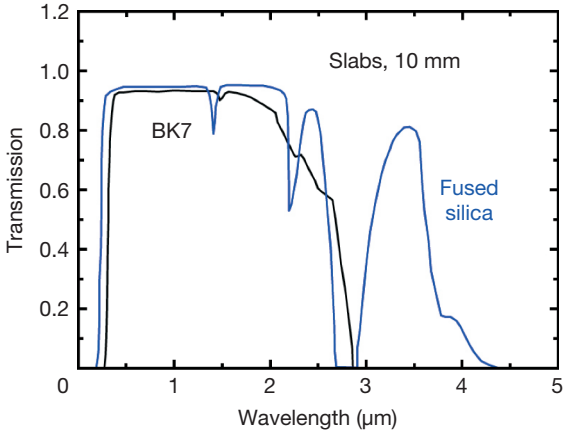

Figure 1.53 Transmission spectra of common laboratory glass BK7 and fused silica. There are usually batch-to-batch variations in the range around the water absorption band at 2.7 μm owing to fluctuations in the OH chemical bond contents in these materials.

1.5.4.2 Some Selective Absorbers

A common misconception among beginners in IR imaging is the expectation that they will be able to observe warm or hot objects immersed in water. This is more or less impossible, as can be seen from Figure 1.54, which depicts theoretical transmission spectra of thin slabs of water. For direct comparison with Figures 1.47–1.53, the slabs are assumed to be surrounded by air. Obviously, only the very thinnest layers of water still allow the transmission of radiation in the thermal IR spectral range.

Water that is 1 mm thick is sufficient to completely suppress any IR transmission in the MW and LW spectral range. In principle, SW IR imaging ($\lambda < 1.7$ μm) seems possible; however, the thermal radiation of objects at temperatures less than 600 K is very low in this spectral range (Figures 1.21 and 1.22).

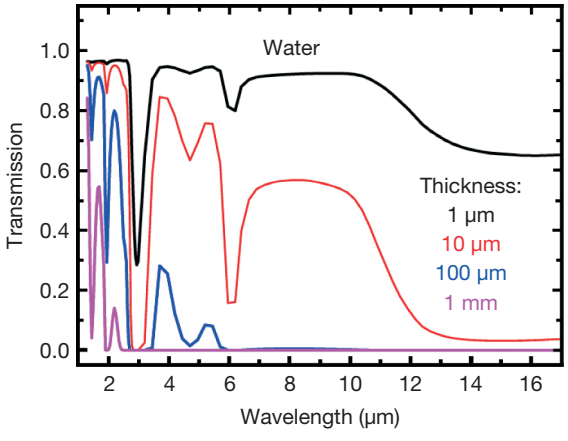

Figure 1.54 Transmission spectra of slabs of water of varying thickness.

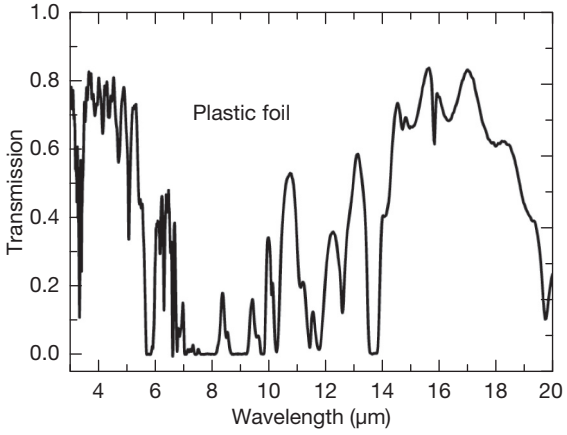

Figure 1.55 Experimental IR transmission spectrum of a plastic foil.

In principle, other liquids like oils or organic compounds can have finite IR transmission; they are, however, only used for special applications and are not treated here.

A final example of another frequently encountered material in IR imaging is shown in Figure 1.55, which depicts the IR transmission of a plastic foil. Plastics are complex organic compound materials that, depending on their type, show a huge variety in chemical composition. Therefore, they can also have large variations in their IR spectra. Obviously, the chosen example may be used for MW cameras. It has several absorption features in the LW range but could perhaps be used as band filter material for special investigations.

1.6 Thin Film Coatings: IR Components with Tailored Optical Properties

Many IR transparent optical materials have transmission values much lower than 100%, some of them being in the range of 70% and others like Ge or Si even in the range of only 50% (Figures 1.48–1.52). These transmission losses are mostly due to the reflection losses from air to the material, with a high index of refraction. Obviously, any optical system using such materials would suffer from substantial losses of IR radiation reaching the detector. To reduce these losses, the lenses and optical components of IR cameras are usually treated with antireflection (AR) coatings. In addition, the coating technique can also be used to tailor desired optical properties like, for example, band filters for IR radiation. The technique to modify optical properties by deposition with thin film coatings is well known from the visible spectral range [25, 27, 44–46] and also has been successfully applied to the IR spectral range [2, 4, 17].

1.6.1 Interference of Waves

The principle behind AR coatings is based on the wave nature of radiation, in particular the phenomenon of interference. Figure 1.56 illustrates interference schematically. IR radiation is an EM wave, which may be described by the oscillation of the electric field vector (Section 1.2.1). Whenever two individual waves (e.g., light waves, sound waves, water waves) meet each other at the same time and location, their elongations (here the electric field) superimpose, that is, they add up to give a new total wave elongation and a new maximum elongation, or wave amplitude. In Figure 1.56a, the two waves superimpose in such a way that the first wave is just shifted by half a wavelength, that is, it is out of phase with the second wave. In this case, the adding up of the two elongations results in complete cancellation of the electric field, and the new total elongation is zero. This is called *destructive interference*. In Figure 1.56b, the two waves superimpose in such a way that the first wave has no shift, meaning it oscillates in phase with the second wave. In this case, the adding up of the two elongations results in a larger elongation of the electric field, that is, the new total amplitude is twice as large as the one from each individual wave. This is called *constructive interference*. The overall energy transported by a wave is then proportional to the square of the amplitude of the wave, that is, in the first case, there is no net energy flux, whereas in the second case, there is twice as much energy flux with regard to the two individual

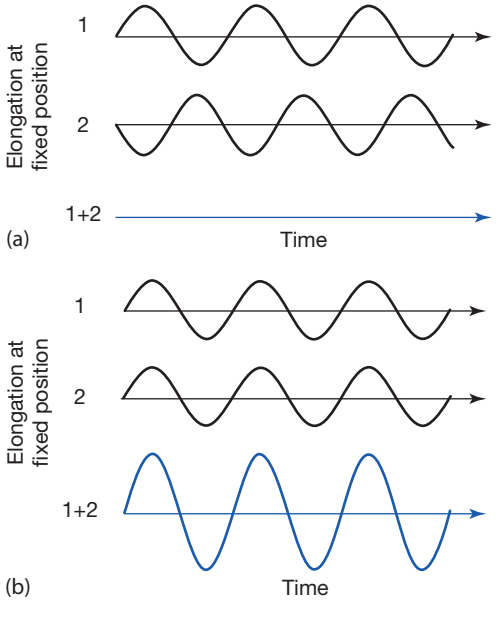

Figure 1.56 Destructive (a) and constructive (b) interference of waves as observed at a fixed location.

waves. Whenever interference happens, the energy flux of waves is redistributed such that in certain directions, destructive interference reduces the flux, whereas in other directions, there is constructive interference with larger flux. Of course, energy conservation is satisfied overall.

1.6.2 Interference and Optical Thin Films

Interference can be utilized to tailor the optical properties of materials by depositing thin films on top of the desired optical material. The idea behind this is schematically illustrated in Figure 1.57. Suppose IR radiation is incident on an optical component made up of a certain material, for example, Ge, Si, or ZnSe. This component material is called the *substrate*. For the sake of simplicity, we assume the substrate to be thick, that is, we only treat the first reflection from the top surface (Figure 1.57a). We can easily calculate the reflectivity for normal incidence from Eq. (1.5).

If a thin transparent film is deposited onto the substrate (Figure 1.57b), there are at least two dominant reflections, one from the top surface of the film and the other from the interface between film and substrate (for the sake of simplicity of argument, we neglect additional reflections). For normal incidence, the two contributions overlap spatially, and at the top surface of the film, the two reflected waves can interfere with each other. With regard to the top reflection (1), the radiation (2) reflected from the interface has traveled an additional distance of twice the film thickness before interfering with the first wave. In this way, a phase shift is induced. For proper film thickness and index of refraction, the phase shift can be chosen such that the two waves interfere destructively. In this case, the thickness of the film needs to be $\lambda/4$, with λ being the wavelength of the EM radiation within the film material. If in addition the amplitudes of the two reflected waves can be made equal, destructive interference can lead to a total suppression of reflected radiation. Alternatively, it is possible to enhance the reflected portion of the radiation using constructive interference. Five parameters determine the optical properties of reflected or transmitted radiation: first, the index of refraction of

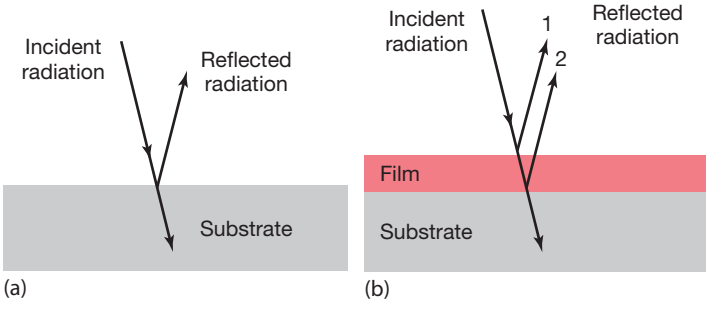

Figure 1.57 (a,b) Idea behind optical coatings (see text for details).

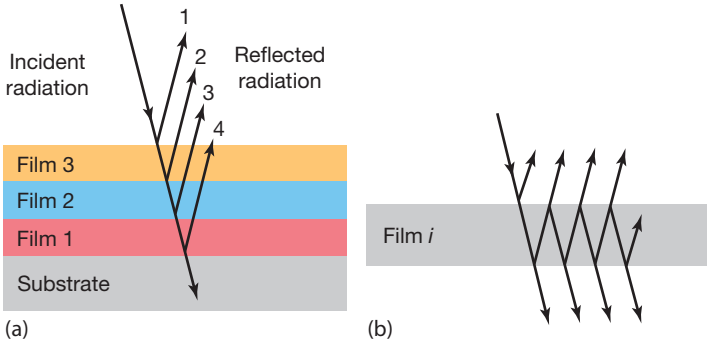

Figure 1.58 Schematic of a multilayer thin film optical coating. In a simplified overview (a), there is a reflection component from each interface; in reality, there are multireflection contributions from each film (b) that need to be summed up.

the substrate material; second, the index of refraction of the film material; third, the thickness of the film material; fourth, the angle of incidence; and finally, the wavelength of the IR radiation.

Optical interference coatings have been studied for many decades in the visible spectral range, the most common and well-known example being AR coatings for eyeglasses. Research has shown that single layers work only for one specific wavelength but are less effective for neighboring wavelengths. If special properties like AR coatings, mirrors, or bandpass filters are needed for broader wavelength ranges, multilayer coatings are used (Figure 1.58). They can range from a few (like three) to several hundreds of layers. Matrix formulations have been developed to analytically treat such multilayer films [44–46]; however, it is obvious that such solutions become very complex, and nowadays computer codes are used to compute the optical properties. We show a few selected results in what follows. However, a word of caution is needed when theoretically discussing thin film properties. Besides the aforementioned theoretical parameters that influence optical properties, one also needs to consider the availability of transparent film materials as well as their growth properties on the given substrate materials. If the lattice constants of the selected film material deviate too much from those of the substrate, it may be that the coating cannot be manufactured.

1.6.3
Examples of AR Coatings

The effectiveness of thin film optical coatings is first illustrated by an example with visible light. Figure 1.59 depicts the reflectivity for normal glass as well as for the same glass substrate coated with either a single layer of MgF_2 (thickness ≈ 90 nm, corresponding to $\lambda/4$ for the chosen reference wavelength of 500 nm) or a triple layer using MgF_2, ZrO_2, and Al_2O_3. The typical glass reflectivity of a single interface is reduced from around 4% to a minimum of about 1.5% for a single-layer coating and to less than 0.1% for an appropriate three-layer coating. The

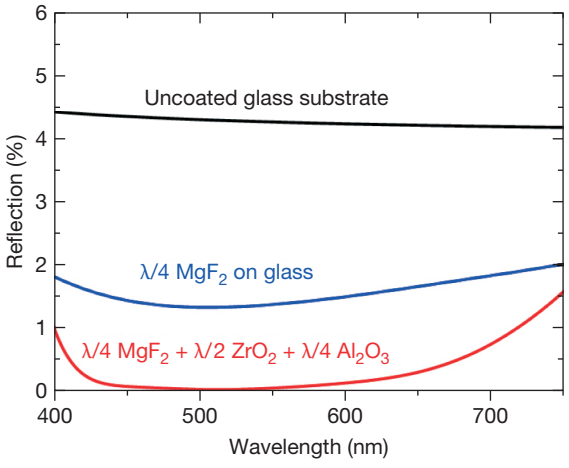

Figure 1.59 Optical antireflection (AR) coatings for glass in the visible spectral range, optimized for a reference wavelength of 500 nm. Multilayer coatings can lead to a broadband reduction of reflectivity (computed with the commercial program Essential McLeod [46]).

multilayer coating has the additional advantage of a very broadband reduction of reflectivity within the visible spectral range. Nowadays such AR coatings are of standard use in eyeglasses and glass lenses (of course, both glass surfaces must be treated).

Similarly, AR coatings can be applied to materials used for IR optical components like IR cameras. For example, silicon has a reflectivity well above 40% and a corresponding low transmission in the MW range. Again, a simple two-layer coating made of MgF_2 and ZrO_2 could easily reduce the reflectivity to below 10% (Figure 1.60), that is, enhance transmission to over 90% (the sum of both is slightly less than 100% because of absorption). Similar AR coatings can be applied to other materials in the LW range. In practice, all component surfaces are treated with AR coatings, not just the front surface.

In conclusion, AR coatings of IR optical components can be easily produced. The exact multilayer composition of manufacturers is usually not known, but the principle behind the method is obvious. Figure 1.61 depicts transmission spectra of a simple single-layer AR coating made of 530 nm ZnS on a silicon wafer. The model result (blue solid line) corresponds quite well with the corresponding real system, which was produced by evaporation techniques in a vacuum chamber and subsequently analyzed using FTIR spectroscopy.

1.6.4 Other Optical Components

Finally, some applications in IR imaging require special optical coatings. There are several common examples. First, one might want to use high-pass or low-pass filters, that is, either only long or only short wavelengths are transmitted

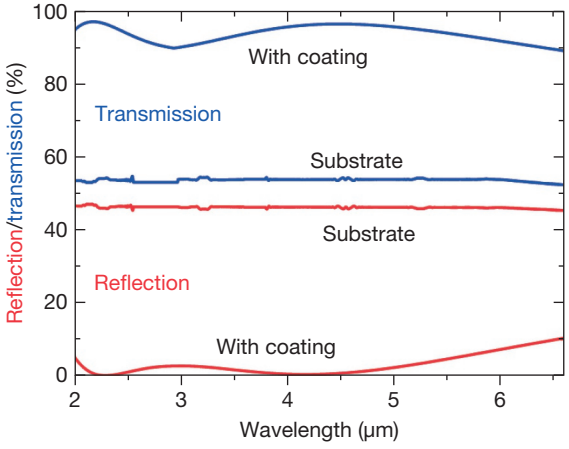

Figure 1.60 Example of antireflection (AR) coatings for silicon in MW IR spectral range (computed using commercial program Essential McLeod [46]).

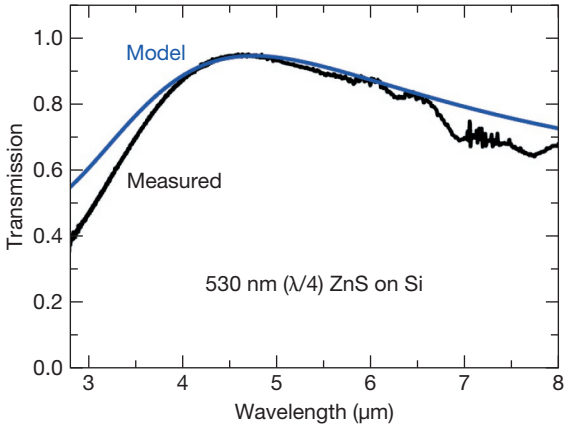

Figure 1.61 Example of a modeled (blue curve) and experimental single-layer antireflection coating of ZnS on top of a silicon wafer.

with respect to a defined reference wavelength. This may be useful if background radiation of well-defined wavelengths need to be suppressed. Second, so-called neutral density filters may be useful if the total radiance incident on a camera is attenuated in a well-defined way. These filters can have a transmission (which can be chosen more or less arbitrarily over a wide range) that is independent of wavelength. Third, several applications require bandpass filters. Such filters are similar to interference filters known from the visible spectral range. Figure 1.62 depicts a typical commercial filter whose transmission corresponds to the CO_2 absorption lines at $\lambda \approx 4.23$ μm. It is characterized by maximum transmission, a bandwidth at half maximum, and sometimes the slope of the curve. Commercially,

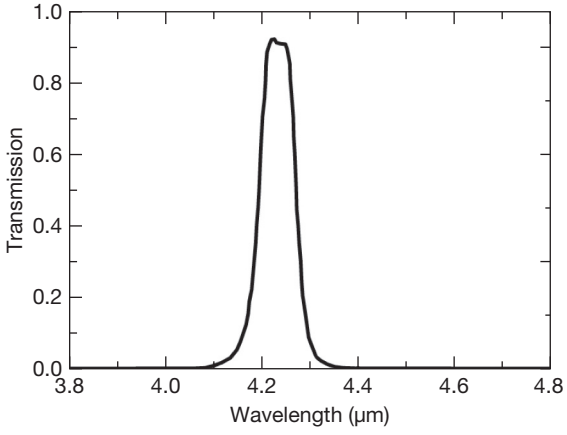

Figure 1.62 Typical example for transmission spectrum of commercially available narrowband IR filter at 4.23 μm.

a wide variety of broadband or narrowband filters are available for nearly every wavelength in the thermal IR range (e.g., [47]).

In conclusion, using thin optical film coatings, it is possible, within certain limits, to tailor desired optical properties of IR optical components. The only important issue to keep in mind is that the materials for the thin films must not absorb in the respective spectral range. Otherwise, they would behave in a manner similar to absorbing windows, that is, absorb part of the radiation, thereby heat up and emit IR radiation, which would introduce an error in the measurement of object temperatures.

Interference filters in the IR are usually a combination of a cut-on and a cutoff filter (Figure 1.63). The use of filters is discussed in Section 3.2.1 and Chapter 8. Many filter materials transmit short IR waves and start to absorb wavelengths larger than a certain wavelength. Ideally, a filter substrate material should absorb only at wavelengths larger than the filter cutoff wavelength. However, in this case, it is important to choose the direction of IR object radiation through the filter. It should pass first through the cutoff filter such that longer wavelengths are reflected, that is, cannot be absorbed in the filter. If radiation passed through the filter in the wrong direction, the filter itself would absorb longer wavelengths and thereby heat up, leading to an additional source of thermal radiation, which would affect the signal-to-noise ratio (Chapter 2). Unfortunately, however, whenever a filter substrate material is absorbing in the used spectral range, it is itself also a source of IR radiation (Eq.(1.27)). Therefore, any warm filter (irrespective of being potentially heated up by absorbing object radiation) will also emit additional broadband background radiation toward the detector. Therefore, the selection of available filters does depend on the application. IR radiation emitted from a filter, in particular if uncooled, may still be tolerated in IR spectroscopy. In contrast, the additional filter radiation – if used as warm filters (Section 8.3) – would dramati-

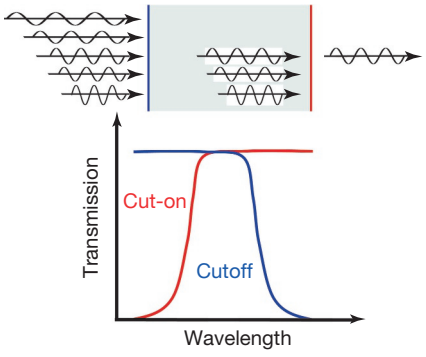

Figure 1.63 An interference filter that has interference coatings on both sides, one acting as a cutoff filter (blue, reflecting long wavelengths), the other acting as cut-on filter (red, reflecting short wavelengths). Together they result in a bandpass filter. Only incident IR radiation with suitable wavelength is transmitted; the rest is reflected, and ideally none is absorbed within the filter.

cally reduce the signal-to-noise ratio in IR imaging. As a remedy, absorbing filters are cooled or filters from nonabsorbing materials must be used. Both absorbing and nonabsorbing filter materials for IR are available [47].

1.7 Some Notes on the History of Infrared Science and Technology

Nowadays, science and technological developments often go hand on hand, stimulating each other. Concerning the beginning of IR thermal imaging, science and technology developed more or less independently. Therefore, we will begin discussing the science alone up to about 1900 before dealing with developments in IR technology.

1.7.1 Infrared Science

Table 1.9 gives a brief overview of early IR science. It may be subdivided into three parts: the discovery of IR radiation, the introduction of the concepts of blackbodies and their radiation, and the development of the laws of radiation. Some concepts and laws were discussed earlier in the introductory sections to provide a scientific basis of the discussed topics; here, however, we focus on the historical perspective.

1.7.1.1 Discovery of Heat Rays and Atmospheric Absorption

The modern history of IR science started around 1737, when Émilie du Châtelet first predicted IR radiation. Châtelet was a French mathematician and physicist who, for example, also translated Newton's *Principia*. In 1737, she entered a contest sponsored by the French Academy of Sciences on the nature of light, heat, and fire. Although she did not win the contest, her work was later published. In this paper, "Dissertation sur la nature et la propagation du feu," she suggested that different colors of light carried different heating power, that is, she anticipated the existence of what is now known as IR radiation [48, 49].

Table 1.9 Timeline of important early IR science discoveries.

Year	Person	Important event in IR science
1737	E. du Châtelet	Prediction of IR radiation
1786	B. Thompson	Transport of heat through vacuum
1800	W. Herschel	Discovery of IR radiation
1804	J. Leslie	Emissivities of different surfaces, Leslie cube
1830s	M. Melloni	Absorption spectrum of liquids and solids
1840	J. Herschel	Atmospheric windows
1859	G.R. Kirchhoff	Blackbody theorem: absorption ↔ emission
1879	J. Stefan	Stefan–Boltzmann law Empirical
1884	L. Boltzmann	Derived from thermodynamics
1893/1896	W. Wien	Wien radiation and displacement laws
1898	O. Lummer/ F. Kurlbaum/ E. Pringsheim	Very precise measurements of cavity (blackbody) radiation at PTR in Berlin
1900/1905	Lord Rayleigh/ J. Jeans	Radiation law
1900	M. Planck	General blackbody radiation law: birth of quantum theory

However, more than 60 years would pass before IR radiation was experimentally discovered by Sir William Herschel. In 1800, Herschel studied the heating power of solar radiation [50, 51]. Radiation from the sun was passed through a prism before different parts of the spectrum would hit sensitive thermometers (Figure 1.64). Herschel found that the resulting temperature rise depended strongly on the location of the thermometer in his spectrum, the visible part of which extended around 10 cm. Herschel found that violet light raised the temperature by 2 °F (for conversions from Fahrenheit into Celsius or Kelvin, see Table 1.2), green by around 3.5 °F, and red light by as much as 7 °F above ambient temperature. Surprisingly, however, the maximum heating effect occurred way beyond the red edge of his visible spectrum, where he measured 9 °F. No effect was observed beyond the violet edge. Herschel observed that these so-called heat rays obeyed the same laws of reflection and refraction as light.

Herschel's work was immediately subjected to severe criticism by Leslie, who challenged the accuracy of the experiments and completely denied the existence of invisible heat rays [52–54]. At that time, the majority of scientists still thought heat could only be transferred by matter. However, it was already proposed in Query 18 by Newton in his *Opticks* [55] that the transfer of heat through a vacuum was possible.

"If in two large tall cylindrical Vessels of Glass inverted, two little Thermometers be suspended so as not to touch the Vessels, and the Air be drawn out of one of these Vessels, and these Vessels thus prepared be carried out of a cold place into a warm one; the Thermometer in vacuo will grow warm as much, and almost as soon as the Thermometer which is not in vacuo." Newton concludes that heat, like

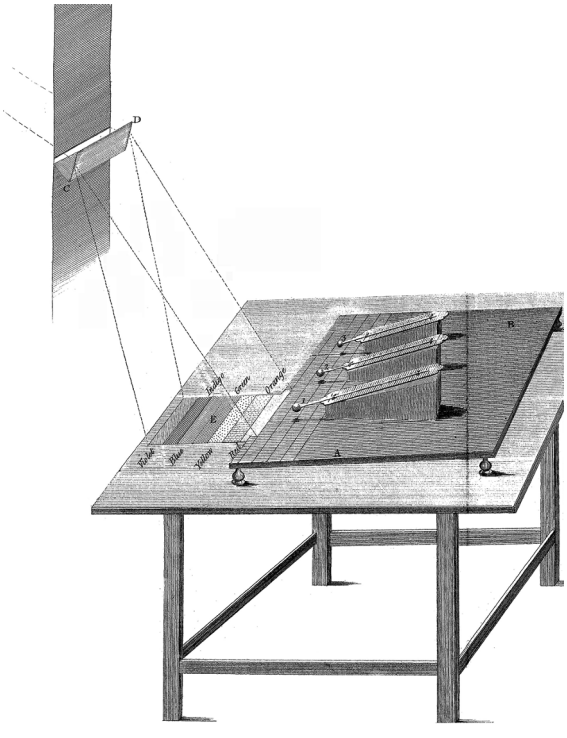

Figure 1.64 Experimental setup used by William Herschel that was used to discover IR radiation (after [51]).

light, is transferred by what others called the ether, a much more subtle medium than air, which remained in the vacuum even after the air was drawn out.

In 1786, Benjamin Thompson, also known as Count Rumford, reported more experiments along these lines. He described some experiments using the vacuum of Torricelli tubes to measure heat transfer through a vacuum [56].

Assuming, therefore, that heat could indeed be transported even in the absence of regular matter (nowadays we no longer need the hypothesis of the ether), it is obvious that Herschel – had he surrounded his thermometers by a vacuum – would have observed more or less the same effect.

Although Leslie, with his denial of invisible heat rays, was not successful in the long run, his rather ingenious attempts to verify his own ideas led to an instrument that is widely known today as the Leslie cube [57] (see Figure 1.28 for modern version of this cube). This instrument makes it possible to directly prove that different surfaces have characteristic abilities to emit heat and that dark or rough surfaces emit heat better than polished ones. He had even already formulated the law that the sum of reflection and absorption (i.e., emission) is the same for all opaque objects.

The first investigation into atmospheric gas absorption in the IR spectral range had to wait a few more decades. In 1840, Sir John Herschel, son of William, while

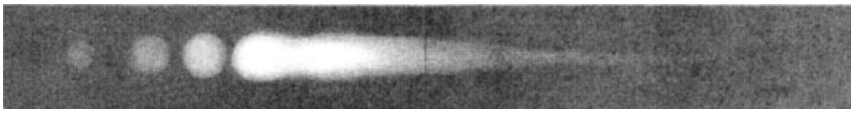

Figure 1.65 Example spectrum (horizontal coordinate related to wavelength) from wet-paper method to demonstrate absorption spectra (after [58]).

focusing his work on the then newly discovered method of photography, discussed the distribution of so-called calorific rays (as they were called at the time) in the solar spectrum by visualizing not only their spectrum but also their absorption features using a wet-paper method (Figure 1.65) [58]. The wet paper dries more efficiently at locations where it is hit by IR radiation. He concluded that the absorption features may be due to the earth's atmosphere, and, if future work supports this idea, "we should see reason to believe that a large portion of solar heat never reaches the earth's surface …" In modern language, the results indicated that IR radiation is strongly attenuated by the atmosphere in certain spectral regions, a discovery that later led to the definition of the atmospheric windows that define the thermal IR wavebands (SW, MW, and LW) used for IR astronomy as well as IR thermal imaging. Much like Herschel, his contemporary M. Melloni also studied absorption spectra, but mostly for liquids and solids (see following discussion).

1.7.1.2 Blackbodies and Blackbody Radiation

The next milestone in understanding thermal radiation was reached in 1859, when German physicist Gustav Kirchhoff, while at the University of Heidelberg in Germany, formulated his famous radiation law. Kirchhoff was collaborating with Bunsen on methods of spectral analysis. In an attempt to understand absorption and emission from a general point of view, he also studied the absorption and emission of thermal radiation emitted from cavities and invented the term *blackbody*. Based on thermodynamics, he formulated what is now known as Kirchhoff's radiation law, which states that the amount of absorption of a blackbody at any given temperature is the same as the amount of emission of the same body provided it is in thermal equilibrium [59–61]. Furthermore, the amount of emitted radiation only depends on wavelength and temperature. The correct corresponding radiation laws were not discovered before the turn of the next century. The main difficulties were, first, to accurately produce and, second, to accurately measure the spectrum of blackbody radiation for a wide temperature range. These problems were solved in the group of Lummer in Berlin first by constructing very precisely temperature-stabilized cavity blackbodies and second by developing very accurate bolometer detectors [62].

Figure 1.66 depicts two of the most famous and precise blackbody spectra of the nineteenth century, which – after Rubens added some at even longer wavelengths [63, 64] – later led Max Planck to his famous radiation law (see subsequent discussion). The spectra were recorded at the Physikalisch Technische Reichsanstalt in the late 1890s by Lummer and coworkers. Besides the observ-

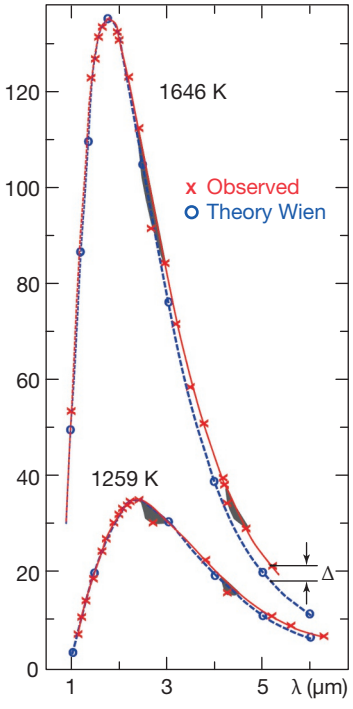

Figure 1.66 Two examples of observed (x) blackbody spectra and those calculated from Wien's radiation law (o) (detail from [62]). Although deviations between theory and experiment seem small (indicated by Δ), they are reproducible and call for improvements in the theory. Gray areas around 2.7 to 3 μm and 4.2 to 4.3 μm refer to H_2O and CO_2 absorption bands.

able residual absorption features of H_2O (between 2.7 and 3 μm) and CO_2 (4.2 to 4.3 μm) from the ambient air, students might think that there was very good agreement between theory and experiment. However, the measurements were so accurate that the experimenters claimed that there was a systematic disagreement between theory and experiment for long wavelengths at high temperature and that the theory of Wien, one of the leading theoreticians of the time, was wrong. Think about how self-confident you must be regarding your own experiments in order to make such a statement!

1.7.1.3 Radiation Laws

Rather than presenting an exhaustive historical discussion on the laws of radiation (which is beyond the scope of this section), we will summarize the most important laws describing thermal radiation for blackbodies in the 40 years between Kirchhoff (1860) and about 1905.

An often used and quite accurate radiation law based on thermodynamics was the one formulated by Wien in the 1890s [65]. As can be seen from Figure 1.66, it described blackbody radiation spectra very well, with only very small deviations for long wavelengths and high temperatures. In modern language, his radiation law in terms of spectral excitance is written

$$M_\lambda^{\text{Wien}}(T)\,\mathrm{d}\lambda = \frac{A}{\lambda^5}\mathrm{e}^{-B/(\lambda T)}\,\mathrm{d}\lambda \tag{1.36}$$

Wien used unspecified constants in the exponent and the nominator in front of the exponential function. This Wien law describes nicely the existence of a maximum and yielded reasonable fits to experimental data at the time. Only later, when Lummer, Pringsheim, and Rubens published more accurate measurements (Figure 1.66), did it become evident that Wien's law was only an approximation that worked very well for short wavelengths, that is, high frequencies, but a better description had to be found for the long-wavelength regime.

Surprisingly, it is also possible to use classical physics to derive a good approximation of blackbody radiation spectra for long wavelengths [66, 67]. This was done by Rayleigh (1900) and Jeans (1905). Their approximation, known today as the Rayleigh–Jeans law (see Eq. (1.37) as a function of wavelength or frequency) faces, however, the issue of the so-called UV catastrophe: according to the law, radiation should increase to infinity for high frequencies (short wavelengths), which is, of course, not the case:

$$M_{\lambda}^{\text{Rayleigh–Jeans}}(T)\,\mathrm{d}\lambda = \frac{C \cdot T}{\lambda^4}\,\mathrm{d}\lambda \quad \text{or} \quad M_{\nu}^{\text{Rayleigh-Jeans}}(T)\,\mathrm{d}\nu \propto T\nu^2\,\mathrm{d}\nu \tag{1.37}$$

Both laws, Wien's (Eq. (1.36)) and the Rayleigh–Jeans law (Eq. (1.37)), are nowadays simple approximate derivations from Planck's law (Eq. (1.15) or (1.17); see also Section 3.2.2.2 and Figure 3.10). Initially Planck believed in Wien's law, which can be derived from general thermodynamic arguments of minute entropy changes for a system in thermodynamic equilibrium. However, in 1900, when confronted with the experimental spectra by Lummer, Pringsheim, and especially by Rubens at even longer wavelengths, Planck changed his mind. It is reported [68–70] that Rubens told Planck on 7 October 1900, about his very-long-wavelength measurements and the problem with the theory. His measurements unequivocally demonstrated that Wien's law could not explain the data. Just one day later, Planck wrote a postcard to Rubens and explained that he had guessed the correction needed. What he had done and what he spoke about some days later on 19 October, directly after Rubens and Pringsheim presented their measurements, was extremely simple: he just changed Wien's law ever so slightly by writing the exponential function as a fraction and adding a 1 in the denominator. As a matter of fact, this change was also supported by some general thermodynamic arguments, though Planck himself noted that he arbitrarily constructed expressions for the entropy that gave similar but improved versions of Wien's radiation law [71]. Therefore, science historians later referred to a very lucky guess. Though Planck's change may appear simple, it has enormous consequences. Only after six grueling weeks of intensive work was Planck able to theoretically derive the new radiation law. In the derivation he had to introduce a new constant and in particular the fact that radiation is not a continuous quantity but only happens in steps of h. This marks the birth of quantum theory.

Spectra of blackbody radiation according to Planck's law were discussed in detail in Sections 1.3.2.2 and 1.3.2.3. Here we briefly add that using Planck's law it is now easy to derive two other very famous radiation laws. Historically they were

derived differently and still in the nineteenth century. The first, called Wien's displacement law (Eq. (1.38), see also Eq. (1.16), [72]), relates the wavelength of maximum spectral emission of radiation with the blackbody object temperature. In brief, it explains that the product of maximum wavelength and temperature is constant (more details can be found in Section 1.3.2.2, Eq. (1.16)):

$$\lambda \cdot T = const \tag{1.38}$$

The second law, the Stefan–Boltzmann law, is again named after two scientists who dealt with blackbody radiation at different times. In 1879, the Slovenian-Austrian physicist Josef Stefan [73, 74], based on experimental data for cooling of mercury thermometers of different initial temperatures (experiments from Dulong and Petit), stated that the total amount of radiation emitted from an object is proportional to the fourth power of its absolute temperature. In modern parlance (see also Eq. (1.19)), we write

$$P_{\text{total}}(T) = \varepsilon A \sigma T^4 \quad \text{in W with} \quad \sigma = 5.67 \cdot 10^{-8}\,\text{W}/(\text{m}^2\,\text{K}^4) \tag{1.39}$$

where ε is emissivity and A the emitting area. (It was subsequently questioned whether Stefan really deserved to be mentioned in the context of this law [75], but here we stick with the general story.) About 5 years later, Ludwig Boltzmann theoretically derived this relation [76]. Similar to the Wien displacement law, the Stefan–Boltzmann law can be directly derived from Planck's law by integrating it over the whole spectral range (Section 1.3.2.4).

The great popularity of the Stefan–Boltzmann law stems from the fact that it allows for easy and quick estimates of surface temperatures and, on the basis of those estimates, estimates of the energy production of stars as derived from their spectra. Stefan in his 1879 paper already compared the estimates available at that time of the surface temperature of the sun and, assuming it to be a blackbody, estimated it be around 5586 °C. Since the sun is not a blackbody emitter, modern estimates derived from its spectrum typically range between 5700 and 6000 K, that is, quite close to Stefan's estimate. Let us briefly demonstrate the usefulness of the Stefan–Boltzmann law, knowing the value of the constant, by considering the total energy flux of the sun. Assuming a temperature of 5800 K, $\varepsilon = 1$, and a sun radius of 696 000 km, we immediately find the total energy flux from the sun to be

$$P_{\text{total}}(T) = 5.67 \cdot 10^{-8} \cdot 5800^4 \cdot 4\pi \cdot (696 \cdot 10^6)^2\,\text{W} \approx 4 \cdot 10^{26}\,\text{W} \tag{1.40}$$

Obviously, only fusion processes within the interior of the sun can permanently produce this huge energy flux, and its value must be consistent with stellar fusion models.

Coming back to earth, this energy flux from the solar surface must also equal the energy flux passing through a sphere with a radius corresponding to the sun–earth distance, that is, a sphere with a radius of around 150 million km:

$$P_{\text{total}}(\text{sun}) = S 4\pi R^2_{\text{sun–earth}} \tag{1.41}$$

This immediately gives a solar constant of around $S \approx 1370\,\mathrm{W/m^2}$ outside of the earth's atmosphere.

1.7.2 Development of Infrared Technology

After the establishment of IR science by 1900, a huge field of applications lay ahead. For the purposes of this book, we will discuss only the following fields:

- Quantitative IR spectroscopy either analytically in laboratories or in astronomy
- Quantitative spot measurements of temperature with either band-pass or broadband pyrometers
- First qualitative and then quantitative thermal imaging

All of these applications are strongly correlated with, first, the development of detector technologies (see details of detector principles in Chapter 2) and, second, further scientific developments in precise definitions in radiometry and technological developments of IR optics (e.g., optical materials, windows, lenses, prisms, filters), as well as calibration sources (blackbodies). With regard to IR imaging, there are obviously two ways to review the further development of IR technology. First, we could just give a chronological discussion, which would have the disadvantage that contributions to the various fields would be strongly mixed, or, second, we could divide this huge field into various subfields, which would help in following the developments in the various fields. We will proceed with the second option and divide the subsequent discussion into three parts:

A. Prerequisites for IR imaging
   1) Detectors and underlying physics
   2) Materials
   3) Blackbodies and radiation sources
   4) Radiometry
B. Development of quantitative measurement techniques
   1) Spectroscopy and IR astronomy
   2) Beginning of contactless T measurement
   3) Vanishing filament band-pass pyrometers
   4) Broadband pyrometers
C. Applications and imaging techniques
   1) Industrial/military applications
   2) Qualitative imaging
   3) Quantitative imaging

We would like to add two general remarks. First, we will make mention of quite a few – mostly freely available – early references that in the nineteenth and early twentieth centuries were often published in German, the then dominant scientific language. One of the most important journals at the time were the *Annalen der Physik*. Unfortunately, the volume count started several times anew with new series, which means that the same volume number refers to different series and

different years. To overcome this sometimes puzzling situation (e.g., when the series number is not mentioned), it was decided to only use a new counting system when the old journals started to be digitized. The relation between the various counting schemes is described in [77]. There, links to web sites are given for free downloads.

We also mention that, in Germany, the IR spectral range was initially called *ultrarot* (or ultrared, "rot" being German for "red"). Similarly, there are a number of other synonyms in the older English literature, such as *caloric rays* or *radiant heat*. This lasted to about World War II, after which the general term *infrared* took over in scientific publications. Another German term lasted for a while, the so-called *Reststrahlen* (Table 1.10). However, this term is no longer important in research or technological applications.

1.7.2.1 Prerequisites for IR Imaging

Table 1.10 presents a timeline for many important discoveries and developments in connection with IR detectors, materials, and other prerequisites for quantitative thermal imaging. We will just mention some milestones here and refer to the extensive literature with reviews of this huge field concerning detectors (e.g., [78–82]), materials [17, 83], and radiometry and instrumentation [1, 84, 85], as well as other early developments including military ones (e.g., [86]).

The discovery of IR radiation by Herschel was accomplished by measuring temperature rises within rather large and bulky thermometers due to the absorption of radiation. Even before these first quantitative measurements, human senses were used to detect radiant heat, that is, IR radiation. There are reports from the sixteenth century [87] that a hand or face in front of a curved mirror that collects radiation, for example from a candle or ice, senses the radiation, that is, acts as a detector. Around 1600, this kind of experiment was supposedly conducted repeatedly using thermometers as detectors [87]. An account of this and related experiments [88] not only demonstrated that a pane of glass in between a source and the skin strongly attenuated the heat perception from a fire (Figure 1.67a) [89, 90], but in particular it described an ice experiment, often named after Pictet. This experiment, performed in the late eighteenth century, seems counterintuitive for many physicists.

Figure 1.67b depicts a setup with the main difference from earlier demonstrations that thermometers were used instead of skin to quantitatively measure the effect. Cold or hot objects are located close to the focal region of a mirror such that emitted radiation is made more or less parallel. It is focused by a second mirror, and a thermometer is placed close to its focal region. The obvious experiment is to have a hot object and detect a temperature rise. Saussure and Pictet used a red glowing metal bullet (about 5 cm in diameter), which they allowed to cool down, such that no visible emission was detectable by the eye. Still, however, there was a strong thermometer signal. Inserting a glass pane reduced the signal. They reproduced these results also with a pot of water that had just boiled. However, when the hot object was replaced by a container of ice or an iced liquid, the temperature dropped several degrees below ambient temperature. At the time, this initially un-

Table 1.10 Prerequisites for IR imaging: detectors, materials, blackbodies, radiometry.

Subfield	Year	Person/reference	Important event of infrared technology
A2	1682	Mariotte [89]	Glass in front of fire decreases sensed radiation. Lambert: glass pane in front of face, even if lens-focused fireplace radiation is directed toward face: no feeling of heat
A2	1779	Lambert [90]	
A3	ca. 1790	Pictet [88]	So-called cold rays emitted from cold objects
A3	1800	Herschel [51]	Discovery of IR radiation in sun spectrum
A1	1821	Seebeck [92]	Thermoelectric effect, ΔT generates voltage
A1	1830	Nobili [93]	Applied thermal element to detect IR radiation
A1	1830/1833	Nobili/Melloni [94]	From thermocouple to thermopile: 10 Sb-Bi pairs in series
A2	1830s	Melloni [97–101]	Transmission IR transparent materials
A1	1834	Peltier [102]	Peltier effect: current generates ΔT, application: cooling system of IR cameras
A1	1839	Becquerel [105, 106]	Photovoltaic effect discovery
A1	1857	Svanberg [110]	Wheatstone Bridge coupled with galvanometer, ΔR due to ΔT, i.e., sensitive thermometer. If hand approaches apparatus: signal due to radiant heat
A1	1873	W. Smith [107]	Photoconductive effect in selenium
A1	1876	W.G. Adams, A.E. Day [108]	Photovoltaic effect selenium (photoelectric currents) "the question … as to whether it would be possible to start a current in the selenium merely by the action of the light"
A1	1880	S.P. Langley [104]a	Platinum foil bolometer. Wheatstone Bridge measurement, sensitivity greater than contemporary thermopiles with similar accuracy. Bolometer: radiation balance
A3	1897	Rubens [63, 64]; see also [112]	Reststrahlen: method to generate large amount of long-wavelength IR radiation
A1	1901	Langley [104]b	Improved bolometer, IR sun spectrum up to 5.3 µm using a 60° rock salt prism
A4	1903	W.W. Coblenz [84, 85]	IR radiometry
A1	1917	T.W. Case [124]	First IR photoconductor Tl_2S up to 1.2 µm and its use for IR telegraphy
A1	1930	[125]	Schäfer/Matossi book: sensitive thermopiles important, in contrast: bolometer seldom used
A1	1938	Ta [109, 126]	Use of pyroelectric crystals for IR radiation, review: [127]
A2	1940s	[117]	KRS5 synthesis of crystals, characterization for IR applications
A1,2	1952	Welker [128]	First synthetic InSb crystal

Table 1.10 Continued.

Subfield	Year	Person/reference	Important event of infrared technology
A4	1950–1960s	Nicodemus, Zissis, Jones [114–116]	Nomenclature, radiometry
A1	1959	W.D. Lawson *et al.* [129]	First studies on HgCdTe, also acronym MCT for mercury cadmium telluride
A2	1950s	[83, 118, 119]	Coatings, filters for IR components
A1	1960s	[78, 160, 204]	Extrinsic detectors Ge:Hg
A1	1970	W.S. Boyle, G.E. Smith [120–122]	Charge-coupled devices (CCDs), Nobel Prize 2009: start signal for multielement detectors in IR
A1	1970s	[123]	Replacement of LN2 cooling by other methods like Stirling coolers
A1	1980s	[130]	Hybrid focal-plane arrays (FPAs): interconnecting detector array to multiplexing (silicon-based) readout, allows independent optimization of detector array and readout Second-generation systems: hybrid HgCdTe(InSb)/Si (readout) FPAs
A1	1982	T.S. Elliott (e.g., [131–133])	Signal Processing In The Element (SPRITE) sensor used with MCT photoconductors
A1	1985	[134–138]	From idea (1973) to 1040 × 1040 Schottky diode FPAs from PtSi
A1	1990s	[139–143]	Quantum well IR photoconductor (QWIP), Stirling coolers, thermoelectric coolers
A1	After 1990s	[144–148]	Cameras with uncooled microbolometer FPAs Peltier T stabilization

expected result led famous physicists such as Lord Rumford to conclude [88] that there is also "emission of frigorific rays from … bodies when they are cold."

The main problem of researchers in thermal physics at the time was the lack of availability of very precise thermometers. Therefore, many physicists„ such as Leslie [57] or Benjamin Thompson, later called Count Rumford [91], built their own apparatus.

A breakthrough, which subsequently spurred the development of much smaller temperature sensors, was made in 1821 by Seebeck, who discovered the thermoelectric effect for a Sb–Cu sample [92]. The principle of this fundamental physical effect is depicted in Figure 1.68a. A temperature difference results in a voltage that is proportional to ΔT:

$$U = C(T_2 - T_1) \tag{1.42}$$

It was soon understood that this effect could be used in measuring absorbed radiation and building sensitive thermometers. Already in 1830, Nobili for the first time used a thermal element of this kind to detect IR radiation [93]. Together

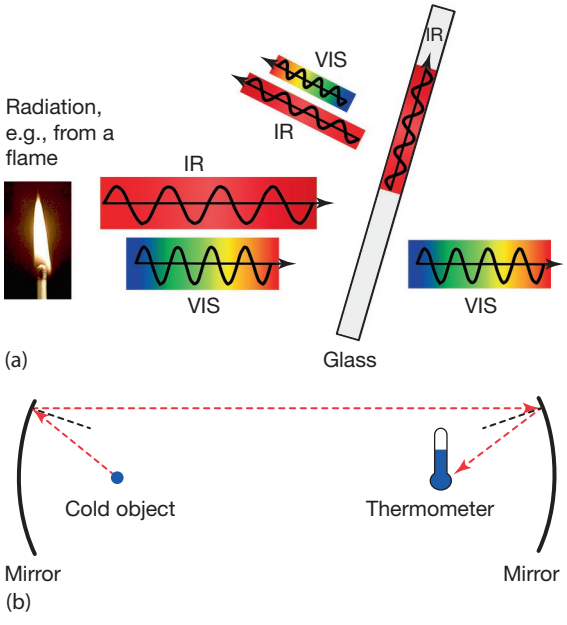

Figure 1.67 (a) Illustration of experiments described by Mariotte and Lambert. In modern terms, most of the IR radiation will be absorbed and some parts will be reflected. (b) Schematic setup to demonstrate so-called cold rays after Pictet.

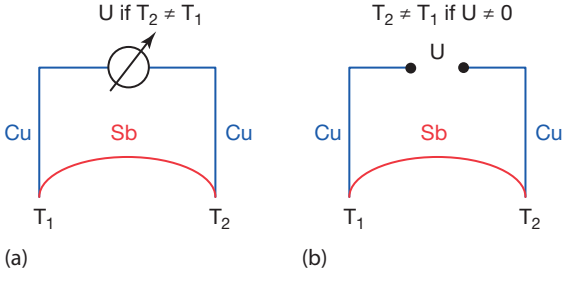

Figure 1.68 Principal setup for thermoelectric effect (a) and Peltier effect (b). If two contacts from two different metals are held at different temperatures, a voltage $U = const.\,(T_2 - T_1)$ results that is characteristic of the two materials. Conversely, if a voltage is applied, then a temperature difference results that can be used, for example, for cooling.

with Melloni [94] he greatly improved sensitivity by adding many of these thermocouple elements together to form a so-called thermopile detector. For example, in 1833 Nobili and Melloni used 10 Sb–Bi pairs in a series circuit. The resulting thermopile was 40 times more sensitive than the best available conventional thermometer, and they could detect the thermal signatures of humans from a distance of up to about 10 m (30 feet) (see also [95, 96]). To obtain the most sensitive instruments, a thermopile was combined with a sensitive galvanometer, and the resulting device was called a *thermo-multiplicator*. Melloni was very productive

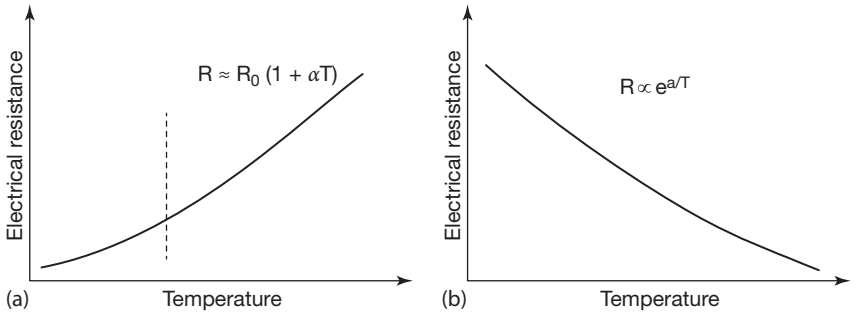

Figure 1.69 Schematic temperature dependence of electrical resistance of metals or alloys (a) and semiconductors (b). Conductors show a nearly linear increase in resistance with temperature, whereas semiconductors show a decrease. Both materials can be used for temperature measurements.

and investigated many thermal effects in the IR range, such as the transmission of solids and liquids for IR radiation [97–101].

The inverse of the photoelectric effect, the so-called Peltier effect (Figure 1.68b), was discovered as early as 1834 [102]. It was also used in IR cameras, for example, as a temperature stabilization unit in uncooled bolometer cameras.

In the following decades, many researchers used thermopiles by building their own devices. A typical commercial device is the thermopile named after Moll made from 16 thermocouples of constantin-manganin. The response time is several seconds, and sensitivity is around 0.16 mV/mW for wavelengths from 150 nm to 15 μm (e.g., [103]).

Another typical thermal detector, the bolometer, followed soon after [104]a. In strongly modified versions this detector type is currently used in many LW IR cameras. It is based on the temperature dependence of the electrical resistance of the materials used. Absorbed radiation leads to a temperature increase, which in turn leads to a change in electrical resistance (Figure 1.69) that is measured.

The next development came with the discovery of photoelectric detectors. Shortly after Becquerel [105, 106] discovered the photovoltaic effect in 1839, photoconductivity [107] and photovoltaic effects [108] were discovered in selenium. In 1938, the first pyroelectric detectors for IR radiation were investigated [109]. The principle of photoelectric radiation detection is schematically shown in Figure 1.70.

It was only a matter of time before other promising materials were investigated, for example, Tl_2S, InSb, HgCdTe, and many others.

Parallel to the development of IR radiation detectors, researchers studied three more fields. The first one dealt with sources of IR radiation. Around the turn of the nineteenth to the twentieth century blackbody sources that emitted broadband IR spectra (Figure 1.66) were widely available. The most precise ones were constructed at the Physikalisch Technische Reichstanstalt in Berlin ([111], Figure 1.71).

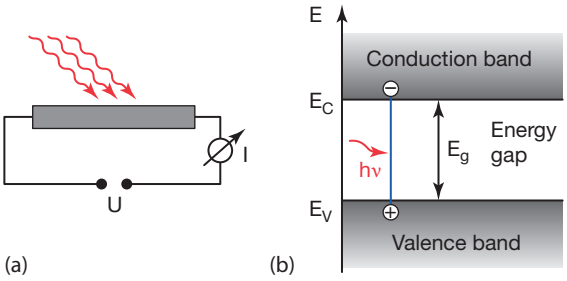

Figure 1.70 (a) Incident radiation on a photoelectric element leads to a change in electrical signals, for example, the current. (b) Simple band structure model: the incident radiation leads to charge carriers within the conduction and valence bands of the material (for more details, see Chapter 2).

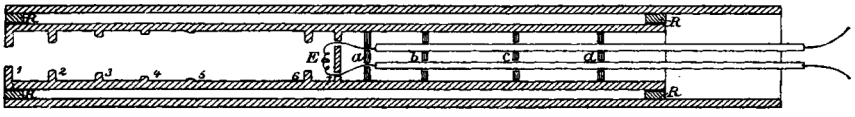

Figure 1.71 Cavity blackbody radiation source (after [111]). Only the inner part near the thermocouple *E* was at the desired stable temperature such that blackbody radiation was emitted through the cavity with diaphragms 1 to 6. The inner cylinder of 0.01 mm thin platinum had a length of 40 cm and diameter of 4 cm.

Intense IR sources for selected wavebands were more difficult to obtain. An ingenious nonspectroscopic and quite easy way to obtain more or less pure IR radiation is the *Reststrahlen* method developed by Rubens [63, 64, 112]. Rubens had discovered that alkali halide crystals showed strong wavelength-dependent absorption bands even for thicknesses of only a few micrometers (excitation of optical phonons plus higher-order additional acoustic phonons that broaden the feature). If broadband IR radiation, for example from an incandescent source such as a blackbody, is incident on alkali halide crystals, these selected bands are reflected better than adjacent wavelengths (Figure 1.72a). Repeating the reflections a few times (Figure 1.72b) leads to rather pure IR radiation wavebands, the so-called *Reststrahlen* (which translates as residual rays that are still there after the multiple reflections), which can be used for further experiments. For example, LiF crystals favor wavebands around 20–30 µm, whereas NaCl results in bands around 50–60 µm.

The second parallel field, developed mostly after around 1950, had to do with how to correctly and quantitatively describe the various quantities associated with IR thermal radiation. As discussed in detail in Section 1.3.1, there are a number of quantities, and some of them, like radiance, are more important for IR imaging than others. Although nomenclature and radiometry may be a dry topic, its development (e.g., [114–116]) was particularly important for any later quantitative application.

The third field, which partially developed independently of the others, concerns optical materials for the IR spectral range. Of course, a huge number of materi-

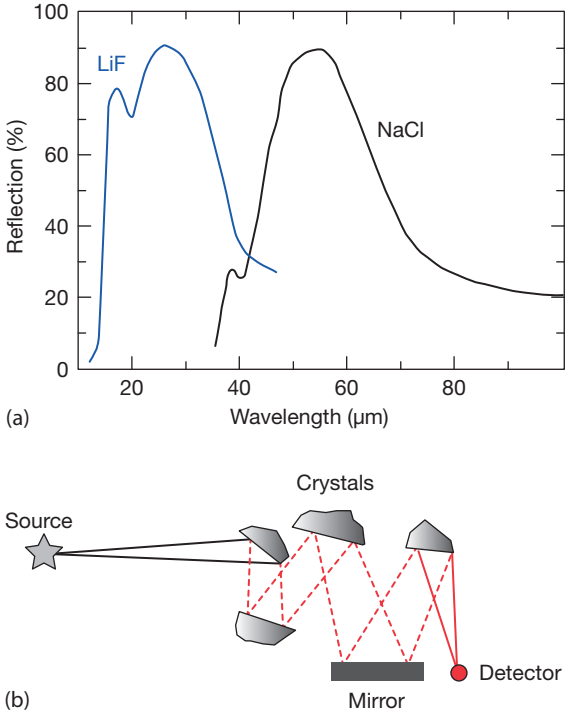

Figure 1.72 (a) Reflectivity from two alkali halide crystals: selected bands are reflected better than other wavelengths (after [113]). (b) Setup to generate *Reststrahlen* using multiple reflections from alkali halide crystals (after [64]).

als have virtually no absorption in the IR range. Some of them were given special names, such as IRTRAN (for IR transmission), for example, Irtran-1 to Irtran-5 are MgF_2, ZnS, CdF_2, ZnSe, and MgO, respectively. In addition, other IR transparent materials are known in industry with acronyms that seem totally unrelated to their chemical composition, such as KRS-5 or KRS-6 for thallium-bromide-iodide or thallium-chloride-bromide. Early research along these lines dates back to the first half of the twentieth century (e.g., [117]). Unfortunately, most IR transparent materials have high refractive index values, which means that they have large reflection losses at the air–material interface. This problem was tackled by optical interference coatings for IR components (e.g., [17, 83, 118, 119]).

A new revolutionary change in detector technology with enormous influence on IR imaging dates back to 1970 when – at first only for the visible spectral range – CCD sensors were introduced by Boyle and Smith [120, 121]. This invention was considered so important that both researchers received the 2009 Nobel Prize in Physics for their work [122]. CCDs are devices that can be used as detectors to record images in electronic digital form. This led to the development of consumer product digital cameras. The CCD surface structure resembles a matrix of a large number of radiation-sensitive cells, called pixels, arranged horizontally

in rows and vertically in columns. Each pixel comprises a metal oxide semiconductor (MOS) capacitor. When a photon impinges upon a pixel, it is converted via the photoelectric effect into one or several electrons that are stored in the capacitor. The number of electrons in a pixel is proportional to the irradiation.

Therefore, the charge distribution in the pixels is a representation of an image.

By reading out the contents of the different pixels using successive charge shifting row by row and within each row column by column (this is done by a readout circuit, ROC), one can reconstruct the image in digital form. A huge advantage of CCD sensors is that they are manufactured on silicon wafers by large-scale integration processes including photolithographic steps, which are well known from microelectronics.

The development of IR detector systems changed rapidly with the introduction of IR multielement sensors, similar to visible CCD chips. In brief, detector elements have been developed as sensor arrays using MCT, PtSi, pyroelectric detectors, microbolometers, and quantum well IR photodetectors (QWIPs). Depending on the required operation temperature, the photoelectric systems were originally cooled by liquid nitrogen. This was later simplified by compact closed cycle cooling systems using the Stirling process or multistage thermoelectric Peltier coolers [123]. Better signal processing became available with the development of SPRITE sensors, which had signal processing already on their sensor elements. The latest and most advanced detectors available now are multiwaveband sensors, which can detect MW as well as LW bands separately.

1.7.2.2 Quantitative Measurements

The development of quantitative IR measurements started in two different fields, pyrometry (i.e., quantitative temperature spot measurements) and spectroscopy (quantitative λ-measurements).

Obviously, generations of potters, metal workers, blacksmiths, and glass blowers had the personal experience to estimate the amount of heat during their process from the color of the kiln, metal melt, or glass. The ideas for measurements of temperature started as early as 1836, when Pouillet suggested estimating temperatures from the color of incandescent bodies [149] (Table 1.11).

Keeping in mind that more than 50 years earlier Wedgewood had noted that it is quite difficult to judge the temperature from the color and brightness of heated objects, and that the brightness of a fire increases through numerous gradations, which can neither be expressed in words nor discriminated by the eye [150], we may be surprised by Pouillet's table. His description of colors was indeed very subjective; however, he was the first to come up with a rule for color change with temperature, although today we are surprised that the perception of white color should start already at temperatures of 1300 °C.

In 1862 Becquerel [151] referred to Pouillet when he suggested that one may indeed use the color to measure temperatures of incandescent bodies. However, since the eye was used as sensor, only very rough estimates could be achieved. This changed by the end of the century when the first laboratory radiative thermome-

Table 1.11 Perceived color of a hot body as a function of its temperature (after [149]).

Dull red	525 °C
Dark red	700 °C
Start of cherry red	800 °C
Cherry red	900 °C
Clear cherry red	1000 °C
Dark orange	1100 °C
Clear orange	1200 °C
White	1300 °C
Shining white	1400 °C
Dazzling white	1500 to 1600 °C

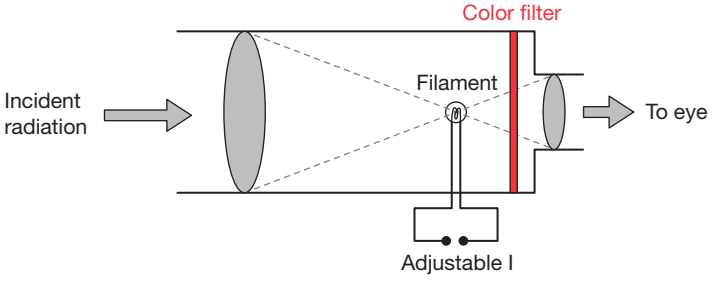

Figure 1.73 Scheme of vanishing filament pyrometer. Radiation from an unknown source is matched to one from a filament whose electrical input power is adjustable.

ters were developed (Table 1.12). The most commonly used type is the vanishing filament pyrometer (Figure 1.73) [152, 153]. In brief, its working principle is similar to that of a telescope that has an electrically heated tungsten filament in the focal plane of the objective lens. Therefore, the image of the lamp filament and its radiation are superimposed on the target radiation. The brightness of the filament is then adjusted until it matches that of the target. This means that within the image the filament disappears against the target. The red filter avoids any misinterpretation thanks to the color differences. Furthermore, it enhances the instrument's sensitivity. The device is calibrated by viewing blackbodies of known temperatures. Errors estimated around 1900 were around 100 °C. Meanwhile, the accuracy of typical commercial devices – if properly operated – is around 1 °C at 775 °C to 5 °C for temperatures at 1225 °C [153]. The most precise modern photoelectric laboratory pyrometers achieve uncertainties better than 0.1 K at 1063 °C and about 2 K at 3525 °C [154] by using much narrower red pass-band filters and photomultiplier tubes as detectors. Additional gray filters may be used to deal with different brightness levels.

Nowadays the vanishing filament pyrometer is rarely used in industry, mostly because it does not allow automated operation, and this is due to the availability of easier-to-operate modern pyrometers [31] that have direct readouts and do not

Table 1.12 Timeline of some important developments in quantitative IR measurements with pyrometers.

Subfield	Year	Person/Ref.	Event
B2	1836	Pouillet [149]	Incandescent color relates to temperature
	Around 1860	Bunsen–Kirchhoff [125]	Start of spectral analysis of atoms; however, initially there was a lack of suitable means to decompose spectrum in IR
B2	1862	Becquerel [151]	Proposed to use red glow of hot bodies to measure T
B2	1892	Le Chatelier [156]	First laboratory radiative thermometer, compared luminance of a target with central part of oil lamp flame, red filter
B3	1899	Morse [157]	US patent, disappearing filament pyrometer; for more details see, for example, [153] for comparison of various temperature measurement methods: accuracies, for example, 61 °C at 775 °C and 65 °C at 1225 °C
B3	1901	Holborn–Kurlbaum [158]	Similar pyrometer, unaware of Morse patent
B4	1901	Fery	Patent on total radiation pyrometer with thermoelectric sensor [31]
	After 1890	Many researchers	First investigations of IR spectra with grating spectrometers of atoms (e.g., [159, 160]); molecular spectra, initially unresolved broadbands [161], later resolved fine structure (e.g., [162]) (e.g., reviews [125, 163])
B3	1923	Fairchild [164, 165]	Changes of pyrometer design into approximately the present form
	1966	Lee [154]	Example of very precise modern photoelectric pyrometers, for example, uncertainties better than 0.1 K at 1063 °C and about 2 K at 3525 °C achieved owing to much narrower pass band in red and VIS photomultiplier tube

rely on the human eye as detector. Three types are common, all of which rely on the same principle as all modern IR cameras do, the main difference being that only one detector element is used. They all detect absorbed IR radiation giving rise to some signal (see corresponding sections in Chapter 2). First, narrowband pyrometers detect IR radiation within a narrow spectral band, much like IR cameras detect in the SW, MW, or LW band.

Second, to avoid the need to know correct emissivity values, ratio or two-color pyrometers were developed, which assume that emissivity does not change when two different wavelengths are used. Third, multiple-wavelength pyrometers were introduced (e.g., [155]) with the aim of becoming totally independent of emissivity (Section 3.2.2).

Parallel to the development of quantitative pyrometry, the first applications of IR spectrometry started as early as the nineteenth century. The birth of spectroscopy probably dates back to Fraunhofer, who in 1814 discovered dark lines within the continuous solar spectrum. In 1859, Bunsen and Kirchhoff interpreted the Fraunhofer lines as absorption lines due to gases in the solar atmosphere, and they developed the method of spectral analysis. Initially, it was mostly applied to atoms in the visible spectral range, and results were used to analyze spectra of stars to learn about their elemental composition. However, it was just a matter of time before the IR spectral range was used as well thanks to the increasing knowledge about it and technologies for generating and detecting the corresponding radiation.

For example, an extensive set of IR spectra of gases, liquids, solids, and minerals is due to Coblentz between 1900 and 1910 (e.g., [166–169]) and others, for example, near-IR (NIR) line spectra of atoms of hydrogen, helium, alkalis, and others were recorded shortly after 1900 by Paschen [159].

After the Bohr model of the atom was developed in 1913, other line spectra, for example, the Brackett and Pfund series of hydrogen in the IR region were predicted and experimentally investigated (e.g., [160, 170]). In parallel, the first investigations of molecular IR spectra started around the turn of the nineteenth to the twentieth century. The development was initially slow, as may be seen in Figure 1.74, which displays the rotational-vibrational spectra of HCl over a period of more than 30 years from 1893 until 1929.

At this time, Angstrom had just succeeded in detecting the location of absorption bands; however, these were very broad and showed no fine structure at all due to the then available low resolution of around 400 nm. In subsequent years the resolution of the spectrometers in the IR range was undergoing continual improvement. In Figure 1.74 this is illustrated by the single broad-band feature

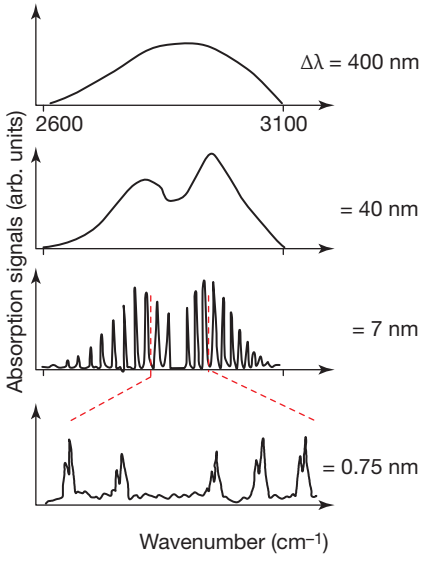

Figure 1.74 Improvements in optical resolution in spectrometers allowed a much better recording of spectra. Here a schematic overview is given for HCl ro-vibrational molecular spectra around 3.4 μm wavelength, which were recorded between around 1890 (top) and 1939 (bottom) (data after [163, 171]).

showing two peaks, then a large number of a few dozen individual peaks, separated by a characteristic missing line in the middle of the spectrum. This spectrum, with 7 nm resolution, represents a typical spectroscopic fingerprint spectrum of a given molecule, here the HCl molecule. Owing to the distinct spectral features that resemble coupled rotational-vibrational excitations in the spectral range, which sensitively depend on the molecule under study, the corresponding spectral region between $\lambda = 2$ to about 25 μm is the fingerprint region for molecules, which is optimally suited for quantitative analysis.

However, it did not end there. With the finest optical resolution available, one could determine that a single one of these individual peaks could still be split into two individual lines. The interpretation in this case is that the nuclear mass of HCl, which has an influence on the rotational motion of the molecule, depends on the isotopes. Two Cl isotopes exist, ^{35}Cl and ^{37}Cl, and the molecular spectra even allow one to investigate isotope effects and the composition of molecules. Besides these coupled rotational-vibrational excitations of molecules in the thermal IR range, purely rotational excitations at larger wavelengths of around 40 to 100 μm were also analyzed (e.g., HCl [172]).

In parallel to these experiments, the further development of quantum mechanical methods in the first decades of the twentieth century led to a very good theoretical understanding of electronic, vibrational, and rotational molecular excitations [173]. However, real experimental progress was made only after fully automated spectroscopic instruments became available after around 1940. Initially they were based on prisms and gratings, but following the invention of the fast Fourier transform (FFT), Fourier transform infrared (FTIR) spectroscopy began to dominate spectroscopic investigations in the thermal IR region starting in the 1980s [174, 175].

Astronomy also started to use the IR spectral range once the first detectors became available (e.g., review [176, 177]). Early applications included measuring the moon or planets and the thermal radiation of stars. In addition, NIR spectroscopy was used to identify corresponding lines from elements within star spectra [178]. The first interstellar and extragalactic molecules, CO, ammonia, and other polyatomic molecules, were detected in the microwave region; however, the IR range was being used, too. A prominent current example is the detection of methane on Mars using ground-based telescopes [179].

1.7.2.3 Applications and Imaging Techniques

There is a huge amount of IR applications, and it is impossible to list them all. Here a short survey of some of the most important milestones is given (Table 1.13). Coming closer to the present time, most advances are being made in modern IR cameras, which is a rapidly growing field in terms of both applications and new developments in detector and imaging technologies. Therefore, the timeline in this section stops at around the year 2000. Later developments are discussed in Chapter 2 on detectors.

The earliest visualizations of thermal signatures are probably medical applications [180] dating back to the Egyptians, who moved hands across the bodies of

ill people to detect temperature changes with their fingers. Later, the Greek Hippocrates (around 400 BC) asserted that body heat was a useful diagnostic indicator of acute diseases [181]. Consequently, it is stated [182, 183] that the Greeks immersed bodies in wet mud and examined the drying process. Areas that dried more quickly were warmer regions, which helped to identify diseased regions of a body.

It took more than 2000 years before new techniques for visualizing temperature distributions on objects were developed [80]. The principle is simple: one needs a specially prepared surface such that incident absorbed radiation causes some observable change in the surface. Herschel in 1840 was the first to come up with the idea of recording/visualizing the invisible IR spectrum of the sun [58]. This may be regarded first as the birth of IR astronomy and, second, as the year of the first IR image of an object, here the spectrum of the sun (Figure 1.65), with absorption bands due to the atmosphere. Herschel moistened a strip of black paper with alcohol. Incident IR radiation led to evaporating alcohol whose pattern was immediately observable to the naked eye. Working on photography, Herschel also tried to produce permanent results by fixing images using a dye that remained on the surface after the evaporation of the alcohol. The dye concentration depended on the velocity of evaporation [58].

Owing to the low sensitivity of the method, it only works well for intense radiation sources, in this case, the sun. Some 25 years later, Tyndall wanted to convert IR images into visible ones [184]. He noted that "We must discover a substance which shall filter the composite radiation of a luminous source by stopping the visible rays and allowing the invisible ones free transmission." Tyndall used carbon arc lamps as intense IR radiation sources, with the VIS filtered out by saturated solution of iodine in carbon disulfide. Tyndall used various detectors, for example, very thin platinum foils (thin to reduce thermal conduction) in a vacuum. The side facing the source was coated with aluminum black and absorbed IR radiation. This led to a permanent image of the carbon arc on the detector owing to the chemical reduction of platinum (Figure 1.75). Tyndall also noted that

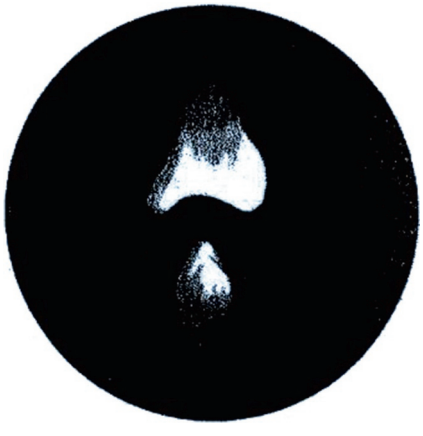

Figure 1.75 Permanent thermal image of arc of carbon arc lamp from 1866 (after [184]).

Table 1.13 Timeline of important developments: IR applications and imaging techniques up to around 2000.

Subfield	Year	Person/company/ reference	Important event in IR imaging technology
C2		Egypt, Greece	[181]: Temperature measurement for illness, detect heat with hands above body [180], also Greeks: drying mud [182, 183]
B1,C2	1840	Herschel [58]	First image spectrum
C2	1866	Tyndall [184, 185]	Thermal images by (1) chemical reduction and (2) color changes
	1880	Abney [186]	Photographic plates, sun spectrum
C2	1929–1938	Czerny, Willenberg, Mollet, Röder [187–190]	Ultrared photography: naphthalene on celluloid membranes, IR absorbed, heating ⇒ sublimation of naphthalene at those locations
C1	1930s/ 1940s	Gudden, Kutzscher	Military research on PbS IR detectors [78]
	1933	Mees *et al.* [195, 196]	Sensitive IR films
C1	1933	Ford Motor Company	First patents for IR drying ($\lambda \approx 1$–$1.6\,\mu m$) in automotive industry
C2	1934	G. Holst *et al.* [197]	First IR image converter (photocathode), more advanced developments in following decades [198]
B2, C1	1940s	Military applications in WWII	First IR display unit, image converter tube, sensitive up to 1.2 μm, used as sniper scopes
C2	1940s	G. Eastman Kodak	Commercial IR sensitive films
	1946 1954 1960	Some military camera developments	First military IR line scanner, line-by-line image, 1 h/image; mounted on aircraft, looking down, scan perpendicular to motion 1954: additional scanner reduced time to 45 min; by 1960: time 5 min/image (after Holst [23])
C2	1953	Gobrecht, Weiss [191]	IR images of hands, face, and so on, evaporography
C2	1950s	P. Kruse/Honeywell, Texas Instruments	IR images [148, 202]
C2	1954	First IR camera	Thermopile (20 min/image); bolometer (4 min/image)
C1	1955	Military	IR seeker heads; detectors PbS, PbTe, later InSb [78]
	1960	Texas Instruments	Camera looking forward/system with two moving mirrors Name: Forward Looking InfraRed system (FLIR)

Table 1.13 Continued.

Subfield	Year	Person/company/ reference	Important event in IR imaging technology
C2	1960s		Ge:Hg, first astronomical applications [78, 205]
C3	1964/ 1965/ 1966	Aga/Agema	Mass-produced cameras for civilian use: AGA 660/Sweden (single-element sensor, optomechanical scanner); 1966: 20 images/s; first camera of modern type, as known today [23, 78]
C2/A1	1970	W.S. Boyle, G.E. Smith [120–122]	CCDs, Nobel Prize 2009
C3	1975		Start of high spatial resolution systems, multielement detectors in mini coolers (first-generation systems, common module in USA) [78, 206]
C3	1980		Second-generation systems: hybrid HgCdTe(InSb)/Si (readout) FPAs
B1	1983	[207]	IRAS satellite for IR astronomy
C3	1985		Schottky diode FPAs (PtSi) commercial systems
C3	1986	Agema	Agema 870 camera with SPRITE sensor
B1	1990s	NASA	NIR instruments on board Hubble Space Telescope, for example, WFC3 [201]
C3	1990		Quantum well IR photoconductor (QWIP), hybrid second-generation systems, Stirling coolers
C3	1995		Cameras with uncooled FPAs, microbolometer, and pyroelectric
C3	> 2000		Start of third-generation system development

mercury iodide changed color from red at room temperature to yellow at 150 °C, that is, the recorded color changes refer to temperature differences. Tyndall finally realized that experiments could be dangerous. His filter solution of iodine in carbon-disulfide was extremely inflammable, and the equipment in his lab caught fire several times.

The next people to try recording thermal images were Czerny and coworkers [187–190]. Whereas Herschel and Tyndall had high temperature sources (sun or arc lamp) and therefore operated at short IR wavelengths, Czerny wanted to detect IR radiation of room temperature.

Obviously regular photography was not possible at long wavelengths because of dark reactions at room temperature.

For his new method, called *ultrared photography*, he used naphthalene or camphor on one side of a celluloid membrane. The other side facing the source

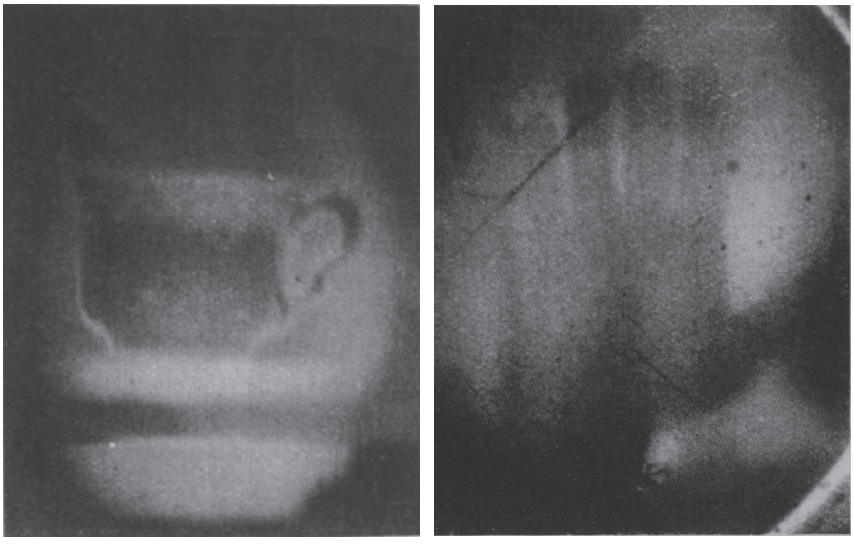

Figure 1.76 Thermographic images of a coffee mug and hand from 1953 (after [191]).

was covered with soot (later other absorbers). Absorbed IR radiation heated the membrane, leading to sublimation of the naphthalene at the respective locations. As a consequence, the irradiated parts of the coated membrane became thinner. Initially, Czerny recorded absorption spectra (with integration times of about 20 min!). A later modification entailed the use of absorbed layers of paraffin oil that evaporated when the membrane was heated. The thickness change resulted in an observed change in interference colors. Image quality depended on the thickness of the absorber layer. For thin layers, sharp images were produced; however, the method was then not very sensitive because of the reduced absorption. But if the absorber layers were thick, strong absorption also led to heat diffusion in the layer, giving slightly fuzzy images. The technique was used to analyze many spectra of fluids or gaseous samples. Also, beakers filled with near boiling water were recorded with exposure times of around 30 s. Drastic improvements in this method were later reported by Gobrecht and Weiss. They were (to our knowledge) the first to publish images of hot coffee mugs, a hand, and even the profile of a face (Figure 1.76, after [191]).

In parallel to these imaging methods based on thermal effects on absorption, research in photography was partly also focusing on the development of films sensitive to NIR radiation. Initially, the creation of IR-sensitive photographic layers and plates was an art in science [186, 192]. The first photographic images of scattered NIR radiation in nature [193] looked very strange compared to visible photos, and there is a lot of interesting physics behind the phenomena [194]. Eastman Kodak was developing the first commercial films based on fundamental research by Mees and coworkers after World War I [195, 196]. IR-sensitive films were soon being sold by at least five companies. Most films were only usable in the very NIR with

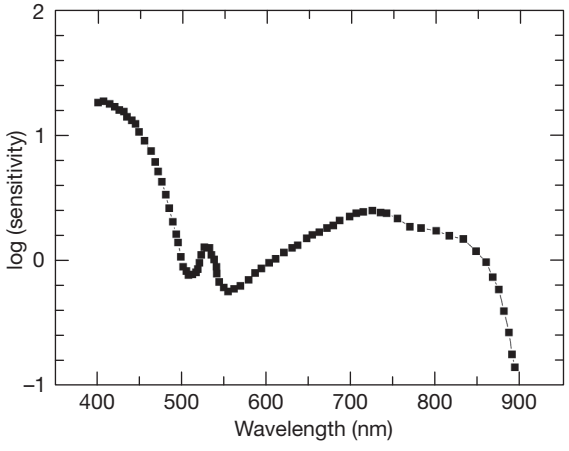

Figure 1.77 Example of sensitivity of Kodak Ektachrome Professional IR-sensitive film (after Kodak).

an upper wavelength of around 900 nm (Figure 1.77). Owing to the shift from film to digital cameras, demand for IR films decreased, and most if not all companies have meanwhile stopped producing IR films altogether.

A typical military development with later commercial use was the invention of image intensification systems, starting during World War II, based on image conversion systems that had been demonstrated as early as 1934 [197]. Image conversion means that red or IR radiation is used to create photoelectrons, which are accelerated and converted back to photons upon hitting a fluorescent layer, which emits shorter-wavelength radiation (Figure 1.78).

In principle, image intensification systems were the basis for early night vision systems [198]. Incident radiation (typically residual light or NIR radiation) is focused with an objective lens on a photocathode. There photoelectrons are created via the photoelectric effect (first conversion). The energy of these electrons is increased by accelerating them using a high electric voltage and they are then directed onto a phosphor screen where they generate photons (second back conversion), which can be viewed through an eyepiece. Early versions used photocathodes of rather low quantum efficiency (compared to today's technology). Owing to their relatively low price (compared to IR cameras), such systems are still used and sold as standard night vision goggles. The reduction in size, weight, and price of modern IR cameras may, however, soon lead to an end of these products. The principle of image intensifiers is also used in many other fields, for example, medical and industrial endoscopes.

An early example of a nonmilitary application of IR radiation is the drying of paints in the automotive industry, dating back to 1993 and operating with IR wavelengths in a range from 1 to 1.6 μm [199].

Another important nonmilitary application of IR radiation is IR astronomy. Following detector development advances, modern IR astronomy started around the

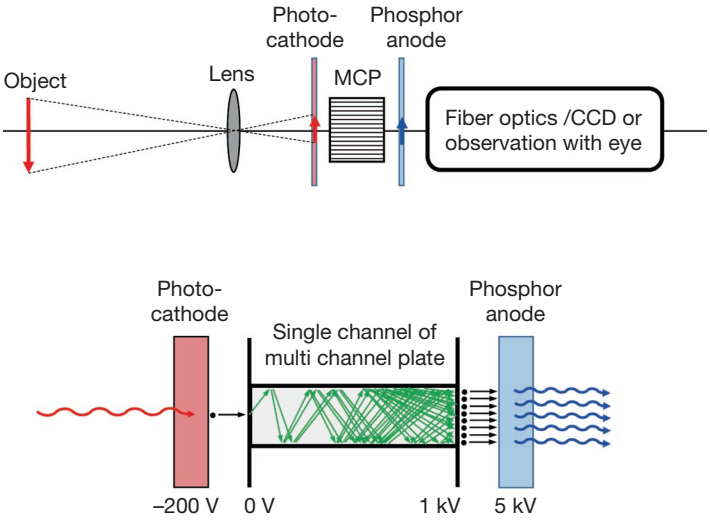

Figure 1.78 Principal setup of an image intensifier (or residual light amplifier). Top: scheme, bottom: enlarged view of main components. A small amount of object scene long-wavelength radiation is directed onto a photocathode. The ejected photoelectrons are accelerated, and their number increases, for example, with a microchannel plate (MCP). The electrons then hit a phosphor, which emits a large amount of shorter-wavelength radiation, which can either be observed by the naked eye or detected with suitable image sensors.

1960s (for a good overview of the topic, see [176]). The best systems nowadays all avoid attenuation due to the earth's atmosphere. The first pure IR satellite (IRAS) was launched in 1983, and more modern systems, such as the Hubble Space Telescope, owed their development to IRAS's success. At present, alternatives to satellites are high flying observatories such as SOFIA, a 2.5 m telescope located on board a 747 airplane [200]. The future of IR astronomy will probably start with the launch of Hubble's successor – currently planned for late 2018 – the James Webb telescope [210], which will have a 6.6 m aperture and detect radiation with wavelengths between 0.7 and 28 µm.

An example of satellite-based IR astronomy is shown in Figure 1.79. It depicts the Carina Nebula at a distance of about 7500 light years, recorded in July 2009 with the Wide Field Camera (WFC3) instrument of the Hubble Space Telescope [201]. The Hubble Space Telescope, put into orbit in April 1990 and fully operational after a service mission in late 1993, has enlarged our knowledge about the universe enormously, partly also because of its amazing capability to detect NIR radiation. Many nebulas are called as such because they have a characteristic appearance in VIS images, as shown in Figure 1.79. It is dominated by scattered light from enormous amounts of dense gas and dust. Therefore stars nestled within the dust cannot be detected in the VIS. However, they can easily be detected in the bottom image, recorded at NIR wavelengths that are scattered much less than VIS light and thus penetrate the gas and dust region (see also

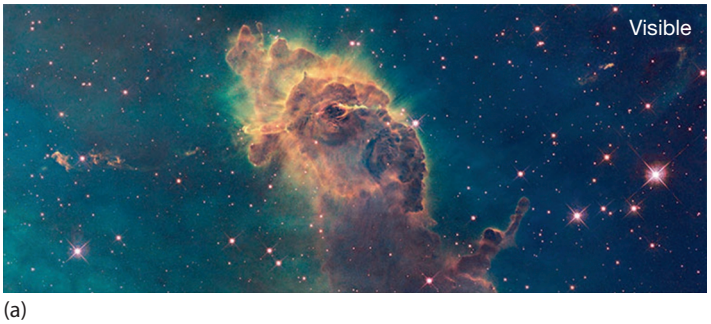

(a)

(b)

Figure 1.79 Comparison of VIS (a) and NIR (b) images of Carina Nebula. The VIS image is a composite and was recorded with a 16 megapixel CCD sensor using narrowband filters with center wavelengths of 502, 656, and 673 nm (false colors assigned are blue, green, and red, respectively). The NIR image was recorded with a 1 megapixel HgCdTe CMOS sensor with center wavelengths of 1.26 and 1.64 μm (false colors are cyan and orange, respectively). Images courtesy NASA, ESA, and the Hubble SM4 ERO team.

Section 6.3.3.3 on NIR imaging examples and Section 10.9 on the range of IR cameras).

Modern IR imaging with electronic detectors started in the late 1940s. The first systems were for the military and consisted of line scanners with a single detector. They were mounted on airplanes looking down while scanning perpendicular to the plane's motion. The forward motion of the plane led to two-dimensional images created from many line scans placed side by side. Recording times were later reduced by the addition of a scanner. A revolutionary design emerged in 1960 when Texas Instruments designed the first system capable of looking at other angles (i.e., not downward) and in particular looking in the forward direction. These systems were therefore called *forward looking IR* and later gave the acronym to the company FLIR Systems, probably the largest worldwide in this field. Many names are associated with the early research in IR detector and camera technology, but here only one of them will be singled out as an example. Paul Kruse (1927–2012) [148, 202], working at Honeywell, started working on IR imaging in the 1950s and pursued this topic until well after his retirement. He made many contributions to the field, in particular on HgCdTe detectors and uncooled microbolometer two-dimensional arrays.

Around 1960, IR detector technology was increasingly being applied to study not only intrinsic materials such as PbS or InSb but also extrinsic, that is, impurity-activated ones that offer the possibility to shift energies by the concentration and kind of doping material [203]. Mercury-doped germanium [204] soon became a new material of choice for IR applications (e.g., [205]) in the 8–14 μm range.

FLIR imagers – produced mostly, of course, for the military – were highly customized, each having unique requirements. For example, between 1964 and 1972, Texas Instruments produced 385 FLIR systems, but with 55 different configurations [206]. Obviously, because of the small numbers per configuration, these were expensive systems. In the 1970s, the need to reduce costs finally led to the development of common modules (CMs), dramatically reducing the number of configurations. The currently accepted idea behind CM systems is that certain functions of an IR sensor are not sensitive to a specific application and can therefore be made universal. This decision marked the start of rapid development in IR imaging.

The first mass-produced civilian-use camera had already been introduced earlier in 1966 with the AGA 660 by Aga (later Agema) in Sweden. Such early cameras were quite heavy and could easily weigh 20 kg, including the control unit. Aga 660 cameras had a single element sensor and an optomechanical scanner unit and pro-

Figure 1.80 AGA Thermovision 665 camera This camera type was sold starting around 1965. Image courtesy FLIR systems, Inc. (2016).

duced about 20 images/s. Figures 1.80 and 1.81 depict two other early commercial models, a Thermovision 665 and a later example of a 1980s medical 30 Hz IR camera (Inframetrics 535) with a single HgCdTe sensor cooled by liquid nitrogen. It was advertised as requiring little space and having video output, and it allowed for recording screen images with a Polaroid camera.

Subsequent changes in IR camera technology included so-called second-generation systems where sensor and ROC were produced as hybrid focal-plane arrays. These required less power consumption and allowed for a more compact design at affordable prices and, hence, led to a real breakthrough for nonmilitary, that is, civilian, applications.

The next milestone was 1995, when the first IR cameras with uncooled microbolometer arrays were produced. The turn of the century marked the start of the development of so-called third-generation systems, which, besides bringing improvements in frame rates, number of pixels, and thermal resolution, saw the emergence of other functions, for example, multiwaveband detection.

The current world leader in IR camera sales, commercial, scientific, and military, is probably FLIR Systems. Founded in 1978, it bought out many successful competitors, such as Agema (formerly Aga Infrared) in 1997, Inframetrics in 1999, Indigo Systems in 2003, and Cedip in 2008.

Figure 1.81 Liquid-nitrogen-cooled Inframetrics 535 IR camera from 1980s producing images of 130 × 200 pixels. The camera was cooled with liquid nitrogen (funnel on top). Hard copy recording was performed on 35 mm film (photo of computer screen) and half-inch VCR (VHS). The needed floor area of 17.5 × 22.5 in^2 was advertised as space saving (see Inframetrics PDF brochure from FLIR web site [209]).

References

1 Wolfe, W.L. and Zissis, G.J. (eds) (1993) *The Infrared Handbook*, revised 4th printing, The Infrared Information Analysis Center, Environmental Research Institute of Michigan.

2 Bass, M. (ed.) (1995) *Handbook of Optics*, Sponsored by the Optical Society of America, vol. 1, McGraw Hill, Inc.

3 Dakin, J.R. and Brown, R.G.W. (eds) (2006) *Handbook of Optoelectronics*, vol. 1, Taylor and Francis, New York.

4 Laurin, T.F. (2005) *The Photonics Handbook, Book 3: The Photonics Directory*, 51st edn, Laurin Publishing Company, Pittsfield.

5 Gross, H. (ed.) (2005) *Handbook of Optical Systems*, vol. 1, Wiley-VCH Verlag GmbH, Weinheim.

6 Gross, H. (ed.) (2008) *Handbook of Optical Systems*, vol. 4, Wiley-VCH Verlag GmbH, Weinheim.

7 Bentley, R.E. (ed.) (1998) *Handbook of Temperature Measurement, Temperature and Humidity Measurement*, vol. 1, Springer, Singapore.

8 Michalski, L., Eckersdorf, K., Kucharski, J., and McGhee, J. (2001) *Temperature Measurement*, 2nd edn, John Wiley & Sons, Ltd, Chichester.

9 Hermann, K. and Walther, L. (eds) (1990) *Wissensspeicher Infrarottechnik*, Fachbuchverlag, Leipzig (in German).

10 Dereniak, E.L. and Boreman, G.D. (1996) *Infrared Detectors and Systems*, John Wiley & Sons, Inc., New York.

11 Holst, G.C. (1993) *Testing and Evaluation of Infrared Imaging Systems*, JCD Publishing Company, Maitland.

12 Jha, A.R. (2000) *Infrared Technology: Applications to Electro-Optics, Photonic Devices, and Sensors*, John Wiley & Sons, Inc., New York.

13 Schlessinger, M. (1995) *Infrared Technology Fundamentals*, 2nd edn, Marcel Dekker, New York.

14 Schneider, H. and Liu, H.C. (2007) *Quantum Well Infrared Photodetectors*, Springer Series Optical Science, vol. 126, Springer, Heidelberg.

15 Schuster, N. and Kolobrodov, V.G. (2000) *Infrarotthermographie*, Wiley-VCH Verlag GmbH, Berlin.

16 Wolfe, W.L. (1996) Introduction to infrared system design, in *Tutorial Texts in Optical Engineering*, vol. TT24, SPIE Press, Bellingham and Washington, DC.

17 Savage, J.A. (1985) *Infrared Optical Materials and Their Antireflection Coatings*, Adam Hilger, Bristol.

18 Palik, E.P. (ed.) (1985) *Handbook of Optical Constants of Solids*, vol. 1, Academic Press, Boston; vol. 2 (1991); vol. 3 (1998).

19 Baehr, H.D. and Karl, S. (2006) *Heat and Mass Transfer*, 2nd revised edn, Springer, Berlin, New York.

20 Incropera, F.P. and DeWitt, D.P. (1996) *Fundamentals of Heat and Mass Transfer*, 4th edn, John Wiley & Sons, Inc., New York.

21 Richards, A. (2001) *Alien Vision, Exploring the Electromagnetic Spectrum with Imaging Technology*, SPIE Press, Bellingham and Washington, DC.

22 Kaplan, H. (1999) Practical applications of infrared thermal sensing and imaging equipment, in *Tutorial Texts in Optical Engineering*, vol. TT34, 2nd edn, SPIE Press, Bellingham.

23 Holst, G.C. (2000) *Common Sense Approach to Thermal Imaging*, SPIE Optical Engineering Press, Washington, DC.

24 Moore, P.O. (ed.) (2001) Infrared and thermal testing, in *Nondestructive Testing Handbook*, vol. 3, 3rd edn, American Society for Nondestructive Testing, Inc., Columbus.

25 Hecht, E. (1998) *Optics*, 3rd edn, Addison-Wesley, Reading.

26 Falk, D.S., Brill, D.R., and Stork, D.G. (1986) *Seeing the Light: Optics in Nature, Photography, Color Vision, and Holography*, Harper & Row, New York.

27 Pedrotti, F. and Pedrotti, L. (1993) *Introduction to Optics*, 2nd edn, Prentice Hall, Upper Saddle River.

28 Palmer, J.M. (1993) Getting intense on intensity. *Metrologia*, **30**, 371–372.

29 Codata values of fundamental constants 2014, www.nist.gov/pml/div684/

fcdc/upload/wall2014.pdf (accessed May 2017).

30 Soffer, B.H. and Lynch, D.K. (1999) Some paradoxes, errors, and resolutions concerning the spectral optimization of human vision. *Am. J. Phys.*, **67**, 946–953.

31 De Witt, D.P. and Nutter, G.D. (eds) (1988) *Theory and Practice of Radiation Thermometry*, John Wiley & Sons, Inc., New York.

32 Fronapfel, E.L. and Stolz, B.-J. (2006) Emissivity measurements of common construction materials. Inframation 2006, Proceedings vol. 7, pp. 13–21.

33 Kanayama, K. (1972) Apparent directional emittance of V-groove and circular-groove rough surfaces. *Heat Transf. Jpn. Res.*, **1** (1), 11–22.

34 Wen, C.-D. and Mudawar, I. (2004) Emissivity characteristics of roughened aluminum alloy surfaces and assessment of multispectral radiation thermometry (MRT) emissivity models. *Int. J. Heat Mass Transf.*, **47**, 3591–3605.

35 Rose, S.R., Watson, I.M., Ramsey, M.S., and Hughes, C.G. (2014) Thermal deconvolution: Accurate retrieval of multispectral infrared emissivity from thermally-mixed volcanic surfaces. *Remote Sens. Environ.*, **140**, 690–703

36 deMonte, J. (2008) Guess the real world emittance. Inframation 2008, Proceedings vol. 9, pp. 111–124.

37 Cronholm, M. (2003) Geometry effects: Hedging your bet on emissivity. Inframation 2003, Proceedings vol. 4, pp. 55–68.

38 Hartmann, J. and Fischer, J. (1999) Radiator standards for accurate IR calibrations in remote sensing based on heatpipe blackbodies. Proc. EUROPTO Conf. Environ. Sens. Appl., SPIE, vol. 3821, pp. 395–403.

39 Henke, S., Karstädt, D., Möllmann, K.P., Pinno, F., and Vollmer, M. (2004) Challenges in infrared imaging: Low emissivities of hot gases, metals, and metallic cavities. Inframation 2004, Proceedings vol. 5, pp. 355–363.

40 F. Olschewski *et al.* (2013) The in-flight blackbody calibration system for the GLORIA interferometer on board an airborne research platform. *Atmos. Meas. Tech.*, **6**, 3067–3082.

41 Madding, R.P. (2004) IR window transmittance temperature dependence. Inframation 2004, Proceedings vol. 5, pp. 161–169.

42 Richards, A. and Johnson, G. (2005) Radiometric calibration of infrared cameras accounting for atmospheric path effects, in *Thermosense XXVII*, Proceedings of SPIE, vol. 5782 (eds G.R. Peacock, D.D. Burleigh, and J.J. Miles), SPIE Press, Bellingham, pp. 19–28.

43 Vollmer, M., Möllmann, K.-P., and Pinno, F. (2007) Looking through matter: quantitative IR imaging when observing through IR windows. Inframation 2007, Proceedings vol. 8, pp. 109–127.

44 Kaiser, N. and Pulker, H.K. (eds) (2003) *Optical Interference Coatings*, Springer, Berlin, Heidelberg.

45 Bach, H. and Krause, D. (eds) (1997) *Thin Films on Glass*, Springer, Berlin, Heidelberg.

46 MacLeod, H.A. (2010) Thin Film Optical Filters, 4th ed., CRC Press. www.thinfilmcenter.com (accessed May 2017).

47 www.spectrogon.com; https://www.jenoptik.com/-/media/websitedocuments/optical-systems/optik/filter_ir_spektralbereich_en.pdf (accessed May 2017).

48 *This month in Physics History: Birth of Émilie du Châtelet*, APS news 17/11, p. 2 (2008), http://www.aps.org/publications/apsnews/200812/physicshistory.cfm (accessed May 2017).

49 du Châtelet, É. (1744) Dissertation sur la nature et la propagation du feu, Paris, Chez Prault, fils, 1744, avail. via Bibliothèque nationale de France, see http://gallica.bnf.fr/ark:/12148/bpt6k756786/f6.image (accessed May 2017).

50 Hearnshaw, J.B. (1986) *The Analysis of Starlight*, Cambridge UP.

51 Herschel, W. (1800) Experiments on the refrangibility of the invisible rays of the sun. *Philos. Trans. R. Soc. Lond.*, **90**, 284–292, doi:10.1098/rstl.1800.0015

52 Cornell, E.S. (1938) The radiant heat spectrum from Herschel to Melloni. – I.

The work of Herschel and his contemporaries. *Ann. Sci.* **3** (1), 119–137 and Cornell, E.S. (1938) II. The work of Melloni and his contemporaries. *Ann. Sci.* **3** (4), 402–416.

53 Olson, R.G. (1969) A note on Leslie's cube in the study of radiant heat. *Ann. Sci.*, **25** (3), 203–208.

54 Olson, R.G. (1970) Count Rumford, Sir John Leslie, and the study of the nature and propagation of heat at the beginning of the nineteenth century. *Ann. Sci.*, **26** (4), 273–304.

55 Newton, I. (1730) *Opticks or, a Treatise of the Reflections, Refractions, Inflections, and Colours of Light,* corrected 4th edn, The Project Gutenberg, EBook #33504

56 Thompson, B. (1786) New experiments upon heat. *Philos. Trans. R. Soc. Lond.*, **76**, 273–304.

57 Leslie, J. (1804) *An Experimental Inquiry Into the Nature and Propagation of Heat*, J. Mawman, London, Edinburgh, reprint Cambridge Univ. Press (2014).

58 Herschel, J.F.W. (1840) On the chemical action of the rays of the solar spectrum on preparations of silver and other substances, both metallic and non-metallic, and on some photographic processes. *Philos. Trans. R. Soc. Lond.* **130,** 1–59, http://www.jstor.org/stable/108209?seq=1#page_scan_tab_contents (accessed May 2017).

59 Kirchhoff, G. (1860) Über das Verhältnis zwischen dem Emissionsvermögen und dem Absorptionsvermögen der Körper für Wärme und Licht. *Pogg. Ann. Phys.* Bd. 19, new count: **185** (2), 275–301.

60 Agassi, J. (1967) The Kirchhoff–Planck radiation law. *Science*, **156**, 30–37.

61 Schirrmacher, A. (2003) Experimenting theory: The proofs of Kirchhoff's radiation law before and after Planck. *Hist. Stud. Phys. Biol. Sci.*, **33** (2), 299–335, University of California Press.

62 Lummer, O. and Pringsheim, E. (1901) Kritisches zur schwarzen Strahlung. *Ann. Phys.*, 4. Folge **6**, new count: **311** (9), 192–210.

63 Rubens, H. and Nichols, E.F. (1897) Versuche mit Wärmestrahlen von grosser Wellenlänge. *Wied. Ann. Phys.*, **60**, new count: *Ann. Phys.*, **296** (3), 418–462.

64 Rubens, H. and Kurlbaum, F. (1901) Anwendung der Methode der Reststrahlen zur Prüfung des Strahlungsgesetzes. *Ann. Phys.*, 4. Folge, Bd. **4**, new count: **309** (4), 649–666.

65 Wien, W. (1896) Über die Energieverteilung im Emissionsspektrum eines schwarzen Körpers. *Ann. Phys.*, **58**, new count: vol **294** (8), 662–669,
in English: (1897) On the division of energy in the emission-spectrum of a black body. *Philos. Mag.*, **43** (262), 214–220.

66 Lord Rayleigh (1900) Remarks upon the law of complete radiation. *Philos. Mag. Ser. 5*, **49** (301), 539–540.

67 Jeans, J.H. (1905) On the partition of energy between matter and ether. *Philos. Mag. Ser. 6*, **10** (55), 91–98.

68 Hollandt, J. (2012) 125 Jahre Forschung an und mit dem schwarzen Körper. *PTB Mitteilungen*, **122** (3), 87–91.

69 Hoffmann, D. (2000) Schwarze Körper im Labor – Experimentelle Vorleistungen für Plancks Quantenhypothese. *Phys. Bl.*, **56** (12), 43–47.

70 Hettner, G. (1922) Die Bedeutung von Rubens Arbeiten für die Planck'sche Strahlungsformel. *Naturwissenschaften*, **10**, 1033–1038.

71 Planck, M. (1900) Zur Theorie des Gesetzes der Energieverteilung im Normalspektrum. *Verh. Dtsch. Phys. Ges.*, **2**, 202 refers to oral presentation of 19 October, see also (1900) Über eine Verbesserung der Wien'schen Spektralgleichung. *Verh. Dtsch. Phys. Ges.*, **2**, 237 refers to oral presentation of 14 December.

72 Wien, W. (1894) Temperatur und Entropie der Strahlung. *Ann. Phys.*, **52**, new count: vol. **288** (5), 132–165.

73 Stefan, J. (1879) Über die Beziehung zwischen der Wärmestrahlung und der Temperatur. *Sitzungsber. Math.-Naturwiss. Classe Kais. Akad. Wiss. Wien*, **79**, 391–428.

74 Wisniak, J. (2006) Josef Stefan. Radiation, conductivity, diffusion, and other phenomena. *Rev. CENIC Cienc. Quím.*, **37** (3), 188–195.

75 Douglas, R.C. (1979) The centenary of the fourth-power law. *Phys. Educ.*, **14**, 234–238.

76 Boltzmann, L. (1884) Ableitung des Stefan'schen Gesetzes betreffend die Abhängigkeit der Wärmestrahlung von der Temperatur aus der electromagnetischen Lichttheorie. *Wiedem. Ann.*, **22**, 291–294, new count: (1884) *Ann. Phys.* **258** (6), 291–294, http://onlinelibrary.wiley.com/doi/10.1002/andp.18842580616/abstract (accessed May 2017).

77 Volume numbers Annalen der Physik: https://de.wikisource.org/wiki/Annalen_der_Physik (accessed May 2017).

78 Rogalski, A. (2012) History of infrared detectors. *Opto-Electron. Rev.*, **20** (3), 279–308.

79 Putley, E.H. (1982) History of infrared detection – Part I. The first detectors of thermal radiation. *Infrared Phys.*, **22**, 125–131.

80 Putley, E.H. (1982) History of infrared detection – Part II. The first thermographs. *Infrared Phys.*, **22**, 189–191.

81 Lovell, D.J. (1969) The development of lead salt detectors. *Am. J. Phys.*, **37**, 467–478.

82 Kutzscher, E.W. (1974) Review on detectors of infrared radiation. *Electro-Opt. Syst. Des.*, **5**, 30–34.

83 Wolfe, W.L. and Ballard, S.S. (1959) Optical materials, films, and filters for infrared instrumentation. *Proc. IRE*, **47** (9), 1540–1546.

84 Coblentz, W.W. (1908) Instruments and Methods used in radiometry. *Bull. Bureau Stand.*, **4** (3), 391–460, Washington, https://archive.org/details/NBSBulletin (accessed May 2017).

85 Coblentz, W.W. (1913) Instruments and Methods used in radiometry II. *Bull. Bureau Stand.*, **9**, 7–63, Scientific Paper 188, https://archive.org/details/NBSBulletin (accessed May 2017).

86 Arnquist, W.N. (1959) Survey of early infrared developments, Proc. IRE 47/9, 1420–1430.

87 Della Porta, G.B. (1589) *Magiae Naturalis*, Naples.
English translation, London (1658) See short description on page 361, book download from the library of congress researchers rare book and special collections room: http://www.loc.gov/rr/rarebook/digitalcoll/digitalcoll-magic.html (accessed May 2017).

88 Evans, J. and Popp, B. (1985) Pictet's experiment: The apparent radiation and reflection of cold. *Am. J. Phys.*, **53** (8), 737–753.

89 Mariotte, M. (1733) 1682 – a short note on an experiment with changed perception, if glass is put in front of fireplace, Histoire de l'Académie Royale des Sciences depuis son établissement en 1666 jusqu' à 1686 vol. 1, Paris, p. 344.

90 Lambert, J.H. (1779) *Pyrometrie oder vom Maaße des Feuers und der Wärme*, Haude und Spener, Berlin, pp. 210–211, Sect. 78, https://books.google.de/books?id=G5l_AAAAcAAJ&printsec=frontcover&hl=de#v=onepage&q&f=false (accessed May 2017).

91 Count of Rumford (1804) An enquiry concerning the nature of heat. *Philos. Trans. R. Soc. Lond.* 94, 77–182.

92 Seebeck, T.J. (1822) Magnetische Polarisation der Metalle und Erze durch Temperatur-Differenz. *Abh. Dtsch. Akad. Wiss. Berlin*, 265–373; also available as: (1895) *Ostwald's Klass. Exakten Wiss.*, **70**, 3–120.

93 Nobili, L. (1830) Beschreibung eines Thermo-Multiplicators oder elektrischen Thermoskops. *Pogg. Ann. Phys.*, **20**, new count: vol. **96**, 245–252.

94 Nobili, L. and Melloni, M. (1833) Untersuchungen über mehrere Wärme-Erscheinungen mittelst des Thermomultiplicators. *Pogg. Ann. Phys.*, **27**, new count: vol. **103**, 439–455.

95 Barr, E.S. (1962) The infrared pioneers – 2. Macedonio Melloni. *Infrared Phys.*, **2**, 67–73, see also: Sir William Herschel. (1961) *Infrared Phys.* **1**, 1–4 and (1963) Samuel Pierpont Langley. *Infrared Phys.*, **3**, 195–206.

96 Hentschel, K. (2005) Macedonio Melloni über strahlende Wärme. *NTM Int. J. Hist. Ethics Nat. Sci. Technol. Med.*, **13** (4), 216–237.

97 Melloni, M. (1833) Ueber den Durchgang der Wärmestrahlen durch ver-

schiedene Körper. *Ann. Phys.*, **28** (2), new count: vol. **104** (6), 371–378.

98 Melloni, M. (1835) Ueber den freien Durchgang der strahlenden Wärme durch verschiedene starre und flüssige Körper. *Ann. Phys.*, **111** (6), 112–139, 277–308.

99 Melloni, M. (1835) Neue Untersuchungen über den unmittelbaren Durchgang der strahlenden Wärme durch verschiedene starre und flüssige Körper. *Ann. Phys.* **111** (7), 385–413 and **111** (8), 529–558.

100 Melloni, M. (1835) Nachtrag zu den Abhandlungen des Herrn Melloni. *Ann. Phys.*, **35** (2), new count: vol. **111** (8), 559–578.

101 Melloni, M. (1835) On the immediate transmission of calorific rays through diathermal bodies. *Philos. Mag.*, **7** (3), 475–478.

102 Peltier, J.C.A. (1834) Nouvelles Expériences sur la Caloricité des courans électriques. *Ann. Chim. Phys.* **56**, 371–386, http://gallica.bnf.fr/ark:/12148/cb343780820/date.r=Annales+de+chimie+et+de+physique.langEN (accessed May 2017).

103 http://www.leybold-shop.com/physics/physics-equipment/heat/heat-transfer/heat-radiation/moll-s-thermopile-55736.html (accessed May 2017).

104 (a) Langley, S.P. The bolometer and radiant energy. *Proc. Am. Acad. Arts Sci.*, **16**, 342–358 (May 1880–June 1881), see also (b) (1901) The new spectrum. *Philos. Mag. Ser. 6*, **2** (7), 119–130.

105 Becquerel, E. (1839) Recherches sur les effets de la radiation chimique de la lumière solaire, au moyen des courants électriques, *C. R. Acad. Sci.*, **9**, 145–149, see http://gallica.bnf.fr/ark:/12148/bpt6k2968p.image.langDE.r=comptes%20rendus%201839 (accessed May 2017).

106 Becquerel, E. (1841) Ueber die elektrischen Wirkungen unter Einfluß der Sonnenstrahlen. *Ann. Phys.*, **54**, new count **130**, 35–42.

107 Smith, W. (1873) Effect of light on selenium during the passage of an electric current. *Nature*, **7**, 303.

108 Adams, W.G. and Day, R.E. (1877) The action of light on selenium. *Philos. Trans. R. Soc. Lond.*, **167**, 313–349.

109 Ta, Y. (1938) Effects des radiations sur les cristaux pyroelectriques, *Compt. Rend.*, **207**, 1042–1044, see http://gallica.bnf.fr/ark:/12148/cb343481087/date.langDE (accessed May 2017).

110 Svanberg, A.F. (1851) Ueber Messung des Leitungswiderstandes für elektrische Ströme und über ein galvanisches Differentialthermometer. *Ann. Phys Chem.*, **24** (3), 411–418 (gesamte Reihe Bd. 160).

111 Lummer, O. and Kurlbaum, F. (1901) Der elektrisch geglühte "schwarze" Körper. *Ann. Phys.*, new count **310** (8), 829–836.

112 Czerny, M. (1923) Über eine neue Form der Rubensschen Reststrahlenmethode. *Z. Phys.*, **16** (1), 321–331.

113 Pohl, R.W. (1954) *Optik und Atomphysik*, 9th edn, Springer.

114 Nicodemus, F.E. and Zissis, G.F. (1962) Methods of radiometric calibration, Report 4613-20-R, Infrared Laboratory, University of Michigan, see http://deepblue.lib.umich.edu/bitstream/handle/2027.42/6821/bac9793.0001.001.pdf?sequence=5 (accessed May 2017).

115 Nicodemus, F. (1963) Radiance. *Am. J. Phys.*, **31**, 368–377.

116 Spiro, I.J., Clark Jones, R., and Wark, D.Q. (1965) Atmospheric transmission: Concepts, symbols, units and nomenclature. *Infrared Phys.*, **5**, 11–36.

117 Tilton, L.W., Plyler, E.K., and Stephens, R.E. (1949) Refractive indices of thallium bromide-iodide crystals for visible and infrared radiant energy. *J. Res. Nat. Bureau Stand.*, **43**, RP2008, http://nvlpubs.nist.gov/nistpubs/jres/43/jresv43n1p81_A1b.pdf (accessed May 2017).

118 Hass, G., Schroeder, H.H., and Turner, A.F. (1956) Mirror coatings for low visible and high infrared reflectance. *J. Opt. Soc. Am.*, **46**, 31–35.

119 Cox, J.T. and Hass, G. (1958) Antireflection coatings for germanium and silicon in the infrared. *J. Opt. Soc. Am.*, **48**, 677–680.

120 Boyle, W.S. and Smith, G.E. (1970) *Bell Syst. Tech. J.*, **49**, 587–593.

121 Amelio, G.F., Tompsett, M.F., and Smith, G.E. (1970) *Bell Syst. Tech. J.*, **49**, 593–600

122 Scientific Background on the Nobel Prize in Physics 2009: Two revolutionary optical technologies, Royal Swedish Academy of Sciences, (2009), http://www.nobelprize.org/nobel_prizes/physics/laureates/2009/ (accessed May 2017).

123 Rogalski, A. (2012) Progress in focal plane array technologies. *Progr. Quant. Electron.*, **36**, 342–473.

124 Case, T.W. (1917) Notes on the change of resistance of certain substrates in light. *Phys. Rev.*, **9**, 305–310.

125 Schäfer, C. and Matossi, F. (1930) *Das Ultrarote Spektrum*, Springer, Berlin.

126 Putley, E.H. (1971) Infrared applications of the pyroelectric effect. *Opt. Laser Technol.*, **3** (3), 150–156.

127 Lal, R.B. and Batra, A.K. (1993) Growth and properties of triglycine sulfate (TGS) crystals: Review. *Ferroelectrics*, **142** (1), 51–82.

128 Welker, H. (1952) Über neue halbleitende Verbindungen. *Z. Naturforsch.*, **7a**, 744–749 and (1954) Semiconducting intermetallic compounds. *Physica*, **XX**, 893–909.

129 Lawson, W.D., Nielsen, S., Putley, E.H., and Young, A.S. (1959) Preparation and properties of HgTe and mixed crystals of HgTe-CdTe. *J. Phys. Chem. Solids*, **9**, 325–329.

130 Kozlowski, L.J. and Kosonocky, W.F. (1995) Infrared detector arrays, in *Handbook of Optics*, Chapt. 23, McGraw Hill.

131 Elliott, C.T. (1981) New detector for thermal imaging systems. *Electron. Lett.*, **17** (8), 312–313.

132 Elliott, C.T., Day, D., and Wilson, D.J. (1982) An integrating detector for serial scan thermal imaging. *Infrared Phys.*, **22**, 31–42.

133 Elliott, C.T. (1985) Cadmium mercury telluride infrared detectors. *J. Cryst. Growth*, **72**, 453–461.

134 Shepherd, F.R. and Yang, A.C. (1973) Silicon Schottky retinas for infrared imaging. IEEE Int. Electron. Dev. Meet. (IEDM73) Tech. Dig., 310–313.

135 Kimata, M., Denda, M., Fukumoto, T., Tsubouchi, N., Uematsu, S., Shibata, H., Higuchi, T., Saheki, T., Tsunoda, R.E., and Kanno, T. (1982) Platinum silicide Schottky-barrier IR-CCD image sensors. *Jap. J. Appl. Phys.*, **21** (1), 231–235.

136 Kosonocky, W.F., Shallcross, F.V., Villani, T.S., and Groppe, J.V. (1985) 160 · 244 element PtSi Schottky-barrier IR-CCD image sensor. *IEEE Trans. Electron. Dev.*, **ED-32** (8), 1564–1573.

137 Kimata, M., Denda, M., Yutani, N., Iwade, S., and Tsubouchi, N. (1987) A 512 × 512-element PtSi Schottky-barrier infrared image sensor. *IEEE J. Solid State Circuits Soc.*, **22** (6), 1124–1129.

138 Yutani, N., Yagi, H., Kimata, M., Nakanishi, J., Nagayoshi, S., and Tubouchi, N. (1991) 1040 × 1040 element PtSi Schottky-barrier IR image sensor. IEEE Int. Electron. Dev. Meet. (IEDM 91) Tech. Dig., 175–178.

139 Levine, B.F. (1993) Quantum-well infrared photodetectors. *J. Appl. Phys.*, **74**, R1–R81.

140 Rogalski, A. (2003) Quantum well photoconductors in infrared detector technology. *J. Appl. Phys.*, **93**, 4355.

141 Veprik, A.M., Babitsky, V.I., Pundak, N., and Riabzev, S.V. (2000) Vibration control of linear split Stirling cryogenic cooler for airborne infrared application. *Shock Vib.*, **7**, 363–379.

142 Korf, H., Rühlich, I., Mai, M., and Thummes, G. (2005) Pulse tube cryocooler for IR applications. Proc. SPIE, vol. 5783, Infrared Technology and Applications XXXI, 164.

143 Mongellaz, F., Fillot, A., Griot, R., and De Lallee, J. (1994) Thermoelectric cooler for infrared detectors. Proc. SPIE, vol. 2227, Cryogenic Optical Systems and Instruments VI, 156.

144 Wood, R.A., Han, C.J. and Kruse, P.W. (1992) Integrated uncooled infrared detector imaging arrays. Solid-State Sens. Actuator Workshop, 1992. 5th Tech. Dig., IEEE, 132–135.

145 Niklaus, F., Vieider, C., and Jakobsen, H. (2007) MEMS-based uncooled infrared bolometer arrays – A review, in *MEMS/MOEMS Technologies and Applications III*, (eds J.-C. Chiao,

X. Chen, Z. Zhou, and X. Li), Proc. SPIE, vol. 6836, 68360D.

146 Roxhed, N. *et al.* (2010) Optical Sensing and Detection, in *Low-Cost Uncooled Microbolometers for Thermal Imaging* (eds F. Berghmans, A.G. Mignani, and C.A. van Hoof), Proc. SPIE, vol. 7726, 772611.

147 Budzier, H. and Gerlach, G. (2011) *Thermal Infrared Sensors*, John Wiley & Sons.

148 Kruse, P.W. (2001) Uncooled thermal imaging – arrays, systems, and applications, in *Tutorial Texts in Opt. Eng.*, vol. TT51, SPIE, Bellingham.

149 Pouillet, C.S.M. Recherches sur le hautes temperatures et sur plusieurs phénomènes qui en dependent. *C. R. Acad. Sci.*, **3**, 782–790 (1836), see also http://gallica.bnf.fr/ark:/12148/cb343481087/date.r=Comptes+rendus+de+l%27Acad%C3%A9mie+des+sciences+1838.langDE (accessed May 2017).

150 Wedgewood, J. (1782) An attempt to make a thermometer for measuring the higher degrees of heat from a red heat up to the strongest that vessels made of clay can support. *Philos. Trans. R. Soc. London*, **72**, 305–326.

151 Becquerel, A.E. (1862) Recherches sur la détermination des hautes températures au moyen de l'intensité de la lumiere émise par les corps incandescents. *C. R. Acad. Sci.* **55**, 826–829, Mallet-Bachelier, Paris.

152 Waidner, C.W. and Burgess, G.K. (1904/1905) Optical pyrometry. *Bull. Bureau Stand.*, **1** (2), 189–254, http://nvlpubs.nist.gov/nistpubs/bulletin/01/nbsbulletinv1n2p189_A2b.pdf (accessed May 2017).

153 Childs, P.R.N., Greenwood, J.R., and Long, C.A. (2000) Review of temperature measurement. *Rev. Sci. Instrum.*, **71** (8), 2959–2978.

154 Lee, R.D. (1966) The NBS photoelectric pyrometer and its use in realizing the international practical temperature scale above 1063 °C. *Metrologia*, **2** (4), 150–162.

155 Ng, D. and Fralick, G. (2001) Use of a multiwavelength pyrometer in several elevated temperature aerospace applications. *Rev. Sci. Instrum.*, **72**, 1522–1530.

156 le Chatelier, H. (1892) Sur la mesure optique des temperatures élevés. *C. R. Acad. Sci.*, **114**, 214–216, http://gallica.bnf.fr/ark:/12148/bpt6k918488/f164.image.r=h%20de%20chatelier%201892.langDE, (accessed May 2017), also H. le Chatelier, O. Boudouard, *Mesure des Températures élevées*, Carré et Naud, Paris.

157 Morse, E.F. (1899) US Patent 696916, Apparatus for gaging temperatures of heated substances (filed 9 November 1899; patent issued 1 April 1902).

158 Holborn, L. and Kurlbaum, F. (1903) Über ein optisches Pyrometer. *Ann. Phys.*, 4. Folge, Bd. **10**, 225–241, new count: vol. **315** (2).

159 Paschen, F. (1908) Zur Kenntnis ultraroter Linienspektra. I. (Normalwellenlängen bis 27 000 Å.-E.). *Ann. Phys.*, **332** (13), 537–570.

160 Brackett, F.S. (1922) Visible and infrared radiation of hydrogen. *Astrophys. J.*, **56**, 154–161.

161 Ångström, K. (1900) Ueber die Bedeutung des Wasserdampfes und der Kohlensäure bei der Absorption der Erdatmosphäre. *Ann. Phys.*, **308** (12), 720–732.

162 Meyer, C.F. and Levin, A.A. (1929) On the absorption spectrum of hydrogen chloride. *Phys. Rev.*, **34**, 44–52.

163 Randall, H.M. (1938) The spectroscopy of the far infra-red. *Rev. Mod. Phys.*, **10**, 72–85.

164 Fairchild, C.O. and Hoover, W.H. (1923) Disappearance of the filament and diffraction effects in improved form of an optical pyrometer. *J. Opt. Soc. Am.*, **7**, 543–579.

165 Foote, P.D., Fairchild, C.O., and Harrison, T.R. (1948) *Pyrometric Practice*, Department of Commerce – Technologic papers of the bureau of standards No. 170, Bureau of Standards, 16 February 1921, US Government printing office Washington.

166 Coblentz, W.W. (1905) Infra-red absorption spectra, I. Gases. *Phys. Rev. (Ser. I)*, **20** (5), 273–291.

167 Coblentz, W.W. (1905) Infra-red absorption spectra, II. Liquids and solids. *Phys. Rev. (Ser. I)*, **20** (6), 337–363.

168 Coblentz, W.W. (1906) Infra-red absorption and reflection spectra (minerals). *Phys. Rev. (Ser. I)*, **23** (2), 125–153.

169 Coblentz, W.W. (1907) Infra-red emission spectrum of burning carbon disulphide. *Phys. Rev. (Ser. I)*, **24** (1), 72–76.

170 Pfund, A.H. (1924) The emission of nitrogen and hydrogen in infrared. *J. Opt. Soc. Am.*, **9** (3), 193–196.

171 Ogilvie, J.F. (1989) Infrared spectroscopy of diatomic molecules – the first century, *Chin. J. Phys.*, **27** (4), 281–296.

172 Czerny, M. (1925) Messungen im Rotationsspektrum des HCl im langwelligen Ultrarot. *Z. Phys.*, **34** (1), 227–244.

173 Herzberg, G. (1939) *Molecular Spectra and Molecular Structure, 1. Diatomic Molecules*, Prentice Hall.

174 Bell, R.J. (1972) *Introductory Fourier Transform Spectroscopy*, Academic, New York.

175 Möllmann, K.-P. and Vollmer, M. (2013) Fourier transform infrared spectroscopy in physics laboratory courses. *Eur. J. Phys.*, **34**, S123–S137.

176 Rieke, G.H. (2009) History of infrared telescopes and astronomy. *Exp. Astron.*, **25**, 125–141.

177 Clements, D.L. (2015) *Infrared Astronomy – Seeing the Heat*, CRC Press.

178 Merrill, P.W. (1934) Photography of the near infra-red region of stellar spectra. *Astrophys. J.*, **79**, 183–202.

179 Mumma, M.J. *et al.* (2009) Strong release of methane on Mars in northern summer 2003. *Science*, **323** (5917), 1041–1045.

180 Berz, R. and Sauer, H. (2007) The medical use of infrared thermography – History and recent applications, paper 04, 12 pages, online-Proceedings Thermographie Kolloquium 2007, DGZfP, Stuttgart/Germany, see http://www.ndt.net/search/docs.php3?MainSource=61 (accessed May 2017).

181 Wunderlich, C.A. (1871) *On the Temperature in Diseases, a Manual of Medical Thermometry*, translation of 2nd German edn, New Sydenham Soc., London.

182 Ring, E.F.J. (2004) The historical development of thermal imaging in medicine. *Rheumatology*, **43**, 800–802.

183 Niumsawatt, V., Rozen, W.M., and Whitaker, I.S. (2015) Digital thermographic photography for preoperative perforator mapping, in *Imaging for Plastic Surgery*, Chapt. 10, (eds L. Saba *et al.*), CRC Press, Taylor and Francis.

184 Tyndall, J. (1866) On calorescence. *Philos. Trans. R. Soc. Lond.*, **156**, 1–24.

185 Tyndall, J. (1868) *Heat – A Mode of Motion*, 3rd edn, Longmans, Greens and Co, London.

186 Abney, W.W. (1880) The Bakerian lecture: On the photographic method of mapping the least refrangible end of the solar spectrum. *Philos. Trans. R. Soc. Lond.*, **171**, 653–667.

187 Czerny, M. (1929) Über Photographie im Ultraroten. *Z. Phys.*, **53** (1/2), 1–12.

188 Willenberg, H. (1932) Ultrarotphotographie. *Z. Phys.*, **74** (9–10), 663–680.

189 Czerny, M. and Mollet, P. (1938) Neue Versuche zur Photographie im Ultraroten. *Z. Phys.*, **108** (1–2), 85–100.

190 Czerny, M. and Röder, H. (1938) Fortschritte auf dem Gebiete der Ultrarottechnik. *Ergeb. Exakt. Naturwiss.*, **17**, 70–107.

191 Gobrecht, H. and Weiss, W. (1953) Zur photograpischen Aufnahme im Ultrarot nach der Methode von Czerny. *Z. Angew. Phys.*, **5** (6), 207.

192 Hentschel, K. (2002) *Mapping the Spectrum – Techniques of Visual Representation in Research and Teaching*, Oxford UP.

193 Wood, R.W. (1910) A new departure in photography. *Century Mag.*, Volume 79, 565–572.

194 Mangold, K., Shaw, J.A., and Vollmer, M. (2013) The physics of near-infrared photography. *Eur. J. Phys.*, **34** (6), 51–71.

195 Brooker, L.G.S., Hamer, F.M., and Mees, C.E.K. (1933) Recent advances in sensitizers for the photography of the infrared. *J. Opt. Soc. Am.*, **23** (6), 216–222.

196 Kenneth Mees, C.E. (1961) *From Dry Plates to Ektachrome Film: A Story of Photographic Research*, Ziff-Davis Pub. Co.

197 Holst, G., de Boer, J.H., Teves, M.C., and Veenemans, C.F. (1934) An apparatus for the transformation of light of long wavelength into light of short wavelength. *Physica*, **1**, 297–305.

198 Montoro, H.P. (2005) Image intensification: The technology of night vision, in *The Photonics Handbook 2005, Book 3 of The Photonics Directory*, 51st Int. edn, Laurin Publishing, Pittsfield, p. H114–H117, see www.photonics.com (accessed May 2017).

199 Groven, F.J. (1933) Ford Motor Company, patents US 1998615 A and US 2057776 A, Paint baking process, registered 21. July 1933 and 29. October 1934.

200 https://www.sofia.usra.edu (accessed May 2017).

201 https://www.nasa.gov/mission_pages/hubble/main/index.html (accessed May 2017).

202 Reine, M.B., Norton, P.R., and Stelzer, E.L. (2013) Paul E. Kruse (1927–2012, in memoriam), in *Infrared Technology and Applications XXXIX*, (eds B.F. Andresen, G.F. Fulop, C.M. Hanson, and P.R. Norton), Proc. SPIE, vol. 8704, 87041F.

203 Bratt, P., Engeler, W., Levinstein, H., Mac Rae, A., and Pehek, J. (1961) A status report on infrared detectors, *Infrared Phys.*, **1**, 27–38.

204 Borrello, S.R. and Levinstein, H. (1962) Preparation and properties of mercury-doped germanium. *J. Appl. Phys.*, **33**, 2947–2950.

205 Westphal, J.A., Murray, B.C., and Martz, D.E. (1963) An 8–14 micron infrared astronomical photometer, *Appl. Opt.*, **2**, 749–753.

206 http://www.ti.com/corp/docs/company/history/timeline/defense/1970/docs/72-common-module.htm (accessed May 2017)

207 Neugebauer, G. *et al.* (1984) The infrared astronomical satellite (IRAS) mission. *Astrophys. J.*, **278,** L1–L6.

208 Tekniska museet in Stockholm, http://www.tekniskamuseet.se/objekt.html?id=http://kulturarvsdata.se/tekm/object/TM40091 (accessed May 2017).

209 http://www.flir.com/uploadedFiles/CVS/Markets/Legacy/Documents/Model%20535%20Inframetrics.pdf (accessed May 2017).

210 http://www.jwst.nasa.gov/ (accessed May 2017).